Development of an XUV Spectrometer for diagnostics of high harmonic radiation pulses generated in a gas jet array

Diploma Thesis
by
Arvid Hage

10th May 2012

submitted to:
Institut für Experimentalphysik
Universität Hamburg

Deutscher Titel:

Entwicklung eines XUV Spektrometers zur Diagnose von Höheren Harmonischen produziert in einem Gas Array

Eingereicht im März 2012
beim Fachbereich Physik

Gutachter der Diplomarbeit:
1. Gutachter: Prof. Dr. J. Rossbach
2. Gutachter: Dr. F. Tavella

Abstract

Recently several experiments showed that the beam quality of a free-electron laser (FEL) can be improved by seeding with an external electro-magnetic wave. At the Free-Electron-Laser in Hamburg (FLASH) the principle of direct seeding is pursued. This will be carried out at a new beamline, called FLASH2, in the extreme ultraviolet (XUV) regime from 10 to 40 nm. The required higher harmonics of the driving laser will be generated in a dual-gas target based on quasi-phase matched (QPM) high harmonic generation (HHG).

In order to characterize the seeding radiation an XUV spectrometer was developed. The development included control programs as well as calculations to calibrate the spectrometer. The spectrometer can operate in the spectral range from 1 to 62 nm and it is able to determine the beam divergence. Measurements with the spectrometer and a dual-gas target were performed to test and improve both designs. Furthermore a one dimensional simulation has been programmed to calculate suitable laser and target parameters for quasi-phase matching.

Zusammenfassung

In den letzten Jahren haben einige Experimente gezeigt, dass die Strahlqualität von einem Freie-Elektronen Laser (FEL) durch das Säen (Seeden) mit einer externen elektromagnetischen Welle verbessert werden kann. Am Freie-Elektronen-Laser in Hamburg (FLASH) wird das Prinzip des “direct seeding” verfolgt. Dies wird bei der neuen beamline mit dem Namen FLASH2 im extrem ultraviolettem (XUV) Bereich von 10 bis 40 nm umgesetzt. Die dazu benötigten höheren Harmonischen des Treiberlasers werden in einem “dual-gas target” generiert, welches auf quasi-phasen angepassten höheren Harmonischenerzeugung basiert.

Um die “seeding” Strahlung zu charakterisieren wurde ein XUV Spektrometer entwickelt. Die Entwicklung beinhaltet Steuerprogramme so wie auch Berechnungen zur Eichung des Spektrometers. Das Spektrometer kann einen spektralen Bereich von 1 bis 62 nm auflösen und die Divergenz des Strahls bestimmen. Die ersten Messungen mit dem Spektrometer und dem “dual-gas target” wurden durchgeführt um beide Designs zu testen und zu verbessern. Des weiteren wurde eine eindimensionale Simulation programmiert um geeignete Laser- und “target-” Parameter für quasi-phasen Anpassung zu berechnen.

Contents

1 Introduction

Free-Electron Lasers (FELs) in the x-ray region are used for the analysis of atomic structures and fundamental processes. Until now the Free-Electron Laser in Hamburg (FLASH) at DESY generates coherent radiation in the wavelength range between 4.1 nm and 44 nm [1, 2] by self-amplified spontaneous emission (SASE). The spectrum and the arrival time of these SASE pulses vary from shot to shot as the structure of this process is stochastic in nature. Thus, in order to control these parameters the FEL can be seeded with an external electromagnetic wave. At FLASH2 the seeding pulses are generated with a high harmonic generation (HHG) target driven by an optical parametric chirped-pulse amplification (OPCPA) system [3]. In order to overlap the seed beam with the electron beam, it is necessary to know the divergence of the seed beam. Furthermore a large energy contrast is needed between the seed radiation and the noise level from the SASE process. Thus, a spectrometer is needed, which can analyse the intensity absolutely and determine the divergence of the seed beam. Furthermore, the spectrometer has to be remotely controllable, as it will be installed in the tunnel of FLASH2. In this diploma thesis a spectrometer, which fulfils these requirement was developed. The spectrometer resolves a spectral range from 1 to 62 nm, which is larger than the spectral range of 10 to 40 nm planned for seeding FLASH2.

The diploma thesis is subdivided into four chapters. In the first chapter fundamentals of accelerator physics as well as the physics of nonlinear processes like high harmonic generation (HHG) are described. Additionally this chapter explains the effects of absorption and the optical Kerr-effect on the measured spectra. In the second chapter, the spectrometer is described in detail and the spectral parameters such as the dispersion and the resolution are calculated. Furthermore, this chapter includes calculations of the filter transmission and simulations of the grating reflectivity efficiency, which enable the calibration of the spectrometer. The required programs to synchronise the dual-gas target with the spectrometer, as well as a program to control the spectrometer remotely are introduced at the end of the second chapter. Measurements with the spectrometer and the QPM target with an array of 13 nozzles are described and evaluated in the third chapter. This experiment was carried out at laser pulse durations of 3.9 fs and 25 fs, whereas seeding is planned for pulse durations between 10 fs and 15 fs. In the last chapter a one dimensional QPM simulation of the dual-gas target is described and a simulation for the FLASH2 seeding system is shown.

1.1 Synchrotron radiation

In the year 1895, W. C. Röntgen discovered the x-rays [4]. It covers a spectral range from 10 to 0.0124 nm, corresponding to an energy range from 100 eV

to 100 keV. The x-rays are used, for example, in biology for structural analysis of DNA and proteins, as well as for the analysis of atoms, molecules and whole crystals [5]. Until 1970 x-rays were produced in an x-ray tube, where electrons were accelerated towards an anode producing Bremsstrahlung with characteristic wavelengths dependent on the anode material. As 95 % of the electron energy was deposited as heat in the anode this concept was restricted to low intensities. A slight increase in intensity was possible with a rotatable anode. However, only with the emitted synchrotron radiation of storage rings and ring accelerators a completely new spectral range with far higher intensities could be reached. Originally accelerators were only used for particle physics and synchrotron radiation was just an undesired effect that limited the energy. Synchrotron radiation is emitted when electrons are forced to change their direction of motion for example in a storage ring, where the electrons are continuously forced on a circular path. With the construction of storage rings just for the generation of synchrotron radiation, undulators and wigglers were developed to generate intensities with a more focused beam profile as well as the opportunity to control the emitted spectrum directly.

1.1.1 Undulators and wiggler

Undulators and wigglers are distinguished by the undulator parameter K which can be calculated with

$$K = \frac{eB\lambda_u}{2\pi mc} \,, \tag{1}$$

where λ_u is the undulator period, e the elementary charge, m the electron mass, c the speed of light and B the amplitude of the magnetic field. The undulator period λ_u is in the order of a few centimetres. If the undulator parameter is in the order of $K > 1$, the magnetic structure is called a wiggler, which characterised by a large perpendicular displacement of the electron bunch. As a consequence the emittance angle of the radiation is so large, that the photons generated at different points due to the oscillation do not overlap with each other. Thus, wigglers have a rather small intensity and a large spectral bandwidth. In contrast an undulator parameter in the order of $K \leq 1$ leads to a smaller perpendicular displacement of the electrons. Such a magnetic structure is called an undulator. The generated intensity of undulators is quadraticly dependent on the number of undulator periods, whereas the intensity of wigglers is linearly dependent. The wavelength of the emitted undulator radiation can be calculated by

$$\lambda_l = \frac{\lambda_u}{2\gamma^2}\left(1 + \frac{K^2}{2} + \Theta^2\gamma^2\right) \,, \tag{2}$$

where the first term is inversely dependent on the energy of the electrons $\left(\frac{1}{\gamma^2}\right)$. The undulator parameter defines the dependence of the undulator wavelength

λ_l on the magnetic structure. The last term $\theta^2\gamma^2$ gives that the wavelength dependence on the observation angle θ between the central axis and the observer. This means, that the shortest wavelength can be observed on axis behind the undulator. The wavelength increases quadratically with the observation angle. Each electron in a bunch emits photons independently, therefore the radiation power is linearly dependent on the number of electrons N_e in the bunch. In order to achieve an increased radiation power, the bunch length has to be reduced below the undulator wavelength λ_l so that coherent radiation with a power dependence of N_e^2 is produced. As λ_l is in the order of a few nanometres it can not be achieved by normal bunch compressors. However, with the invention of Free-Electron Lasers it became possible to modulate the charge of electron bunches on the scale of λ_l.

1.2 Free Electron Lasers

Typical Free-Electron Lasers are based on self-amplified spontaneous emission (SASE). The electrons emit spontaneous uncorrelated radiation in the first section of the undulator. This electromagnetic wave interacts with the electrons, so that the electrons transfer energy to the electric field. This is continuously possible when the electrons slip behind the light wave by λ_l or a multiple of λ_l per undulator period, where λ_l is the light-wavelength which is similar to the undulator wavelength in forward direction [6]. This slippage is due to the fact that the electrons have to travel a longer path than the electro-magnetic wave in the undulator as they are deflected by the magnet field. Using equation (2), the resonance energy γ_r can be calculated, which is the energy the electrons need to emit undulator radiation with the wavelength λ_l :

$$\gamma_r = \sqrt{\frac{\lambda_u}{2 \cdot \lambda_l}(1 + \frac{K^2}{2})} \, ,$$

where $\Theta = 0$. Free-Electron Lasers are divided into low gain and high gain Free-Electron Lasers, where the gain describes the increase of the electric field per passage of the electrons through the undulator section.

Low Gain FEL Electrons with an energy higher than the resonance energy γ_r amplify the electric field of the low gain FEL, whereas electrons with less energy attenuate the field. If the electrons are tuned right on the resonance energy there will be no energy gain of the electromagnetic wave, because the same amount of energy is contributed to the electric field as removed from it by the electrons. Hence, in order to start the FEL process the relative energy distribution η has to be positive:

$$\eta = \frac{\gamma - \gamma_r}{\gamma_r} \, .$$

The main assumption of the low gain FEL theory is that the electric field amplitude is constant for one passage of the electrons. Due to this low gain, the radiation has to be reflected in a resonator over the whole undulator section so that it is amplified by many passages of the electrons. Thus, the low gain FEL is limited to the visible and infrared region because the mirror reflectivity efficiency for XUV radiation is far to low. Especially for large angles of up to 180°, which would be necessary for the resonator, the reflectivity drops dramatically.

High Gain FEL In contrast to a low gain FEL the energy distribution η of a high gain FEL has to be near or equal to zero in order to achieve a strong amplification of the radiation. The advantage of a high gain FEL is that it is not necessary to rely on a resonator with mirrors, because the electrons have to pass the undulator only once to create, for example, XUV radiation of sufficient intensity to enable experiments on the atomic scale. This is possible, because of the interaction of the electric field with the electrons, which imprints a so called microbunch structure on the complete bunch. The microbunch structure is of the same scale as the light wavelength and thus a charge density is reached, which is high enough for coherent radiation of the electrons. The microbunch structure is created by the fact that electrons, which gain energy from the electric field, take a shorter pass and electrons, which lose energy to the electric field, take a longer path. In comparison to a low gain FEL, the undulator section of a high gain FEL is longer so that the microbunch structure can develop completely, whereas even a small charge modulation in a low gain FEL will be erased during one round trip in the storage ring by the bending magnets. Another limiting factor for the high gain FEL process is a required peak current of more than $1000\,A$ [6], as well as a small transverse beam profile. In order to achieve these parameters the dispersion should be as small as possible. Thus, linear accelerators have to be deployed due to their small dispersion, which is only introduced by chicanes such as bunch compressors. Storage rings have a large dispersion as well as long bunches, which is quite contrary to the parameters needed for an ideal high gain FEL.

When the microbunch modulation is fully developed in a high gain FEL, no further amplification is possible and the microbunch structure will dissolve again. This occurs at about 20 gain lengths [6]. The gain length L_G is dependent on the charge density n_e and the energy of the electrons:

$$L_G = const \cdot \gamma_r \cdot \left(\frac{1}{n_e}\right)^{\frac{1}{3}} = const \cdot \gamma_r \cdot \left(\frac{\sigma_t^2}{I_0}\right)^{\frac{1}{3}} \ ,$$

where σ_t is the transverse RMS size and I_0 the peak current. The gain

$$G(z) \propto e^{(\frac{z}{L_G})} \ ,$$

increases exponentially with z, where z is the distance from the entrance of the undulator. Thus, in order to achieve a high gain a short gain length is required, which can be attained by minimizing σ_t and increasing I_0.

1.3 Linear optics

1.3.1 Gaussian optics

The theory of Gaussian optics describes the optical parameters of a Gaussian beam and its evolution in an optical system. Consequently the transverse profile is specified by a Gauss function. A Gaussian beam is defined by its complex electric field amplitude given by

$$E(r,z) = E_0 \cdot \frac{w_0}{w(z)} \cdot e^{\left(-\frac{r^2}{w^2(z)}\right)} \cdot e^{\left(-ikz - ik\frac{r^2}{2R(z)} + i\varphi_G(z)\right)} , \tag{3}$$

where $w(z)$ is the beam width at the point where the intensity has decreased by $\frac{1}{e^2}$:

$$w(z) = w_0 \sqrt{1 + \left(\frac{z}{z_R}\right)^2} , \tag{4}$$

where w_0 is the radius of the beam at the waist (focal spot). With equation (3) the electric field amplitude can be calculated in dependence of the distance from the waist in longitudinal or axial direction given by z and the radial distance r. The phase shifts by π as the beam passes from the upstream far field to the downstream far field through the focus [7]. This is called Gouy phase shift:

$$\varphi_G(z) = -\arctan \frac{z}{z_R} , \tag{5}$$

where $z = 0$ is the position of the beam waist and z_R is the Rayleigh length, which can be calculated for a Gaussian beam with

$$z_R = \frac{\pi w_0^2}{\lambda} , \tag{6}$$

where λ is the central wavelength of the beam. Hence, the Rayleigh length is just the distance from the beam waist to the point where the radius of the beam has increased by a factor of $\sqrt{2}$. For $z \gg z_R$ the beam size $w(z)$ will become a straight line with an angle Θ to the central beam axis. This angle is a measure of the divergence of the beam and can estimated by

$$\tan \Theta = \frac{\lambda}{\pi w_0} = \frac{w(z)}{z} . \tag{7}$$

The shorter the wavelength the smaller is the angle of divergence. Therefore, it is necessary for experiments to use different focusing or beam guiding optics for different wavelengths, which is very important for HHG radiation as their wavelength and therefore their divergence varies over a wide range.

1.3.2 Spectral resolution

The spectral resolution of a planar grating is determined by

$$R = \frac{\lambda}{\triangle\lambda} = m \cdot N \ , \tag{8}$$

where λ is the examined central wavelength, m is the diffraction order, N is the number of grooves illuminated by the beam [8]. The full width half maximum (FWHM) of the examined central wavelength is defined by $\triangle\lambda$. From equation (8), it follows that the best resolution R is achieved when the maximum number of grooves is illuminated. The resolution R increases also with the refraction order m. The grooves can be produced with different shapes, for example with a triangular or a rectangular shape. Gratings with triangular grooves are called Blaze gratings. These gratings are defined by the Blaze angle, which is the angle of the long side of the triangle to the grating normal. The long side of the grating faces into the direction of the incident beam (see figure 1).

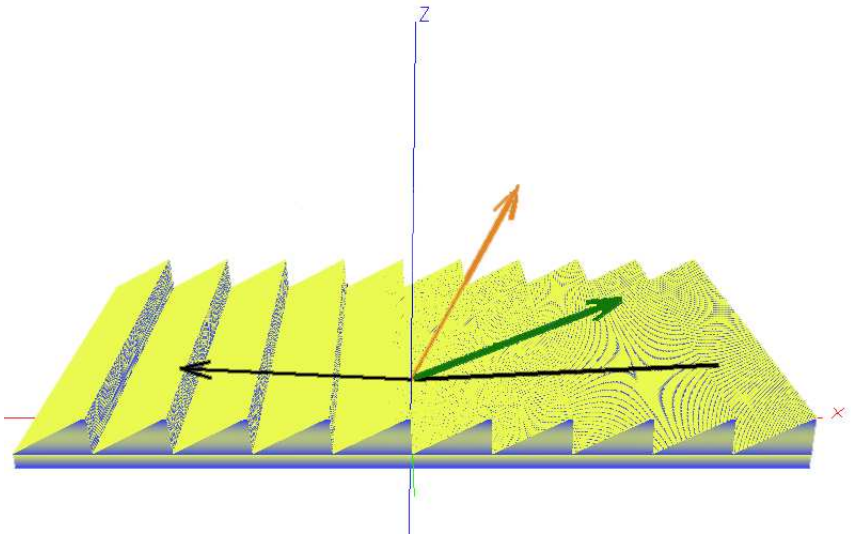

Figure 1: Schematic of a blaze grating with a blaze angle of 10°. The beam direction corresponds to the x-axis with an angle α of in this case 87° to the z-axis. The black arrow marks the direction in which the gratings has to be orientated. The green (orange) arrow marks the direction of the first (second) order diffraction.

With the incidence angle α and the exit angle β, the corresponding wavelength for constructive interference can be calculated by the well-known grating equation:

$$d \cdot (\sin\alpha + \sin\beta) = m \cdot \lambda \ , \tag{9}$$

where d is the grating constant. As a simplification only the first order diffraction is considered with $m = 1$. Therefore, the resolution per angle is

$$\frac{d\lambda}{d\beta} = d \cdot \cos\beta \ .$$

The angle β can be written in dependence on the wavelength λ and the incidence angle α [8]:

$$\beta = \arcsin(\frac{\lambda}{d} - \sin\alpha) \ .$$

Hence the minimal wavelength difference $d\lambda$, which can be distinguished can be calculated by multiplication of both sides with $d\beta$:

$$d\lambda = d \cdot \cos\left(\arcsin(\frac{\lambda}{d} - \sin\alpha)\right) \cdot d\beta = d \cdot \sqrt{1 - (\frac{\lambda}{d} - \sin\alpha)^2} \cdot d\beta \qquad (10)$$

The simplification was carried out by using the trigonometric theorem:

$$\cos(\arcsin(x)) = \sqrt{1 - x^2} \ .$$

1.4 Nonlinear optics

With the invention of lasers in the year 1960 the light intensities where high enough to examine the nonlinear behaviour of light in optical materials [9]. Nonlinear optics covers a range of effects. The first discovered effect was the second harmonic generation by Peter Franken et al. at the University of Michigan in 1961 [10]. Other important nonlinear processes are optical parametric amplification (OPA), high harmonic generation (HHG) and the optical Kerr effect, which leads to self-focusing and self-phase modulation. The electric field required to observe nonlinear effects has to be higher than the inner atomic electric field, which is about $E = 10^8 \frac{V}{m}$. This would correspond to a laser intensity of

$$I = \frac{n \cdot \left(\overrightarrow{E}(\omega)\right)^2}{2 \cdot \eta_0} = 1.3 \cdot 10^9 \frac{W}{cm^2} \ , \ for\, n = 1 \ , \qquad (11)$$

where $\eta_0 = Z_0 = \sqrt{\left(\frac{\mu_0}{\varepsilon_0}\right)}$ is the impedance of free space. A pulsed laser system easily reaches these intensities. The intensity of a pulsed laser in the focal spot can be calculated with

$$I\left[\frac{W}{cm^2}\right] = \frac{Energy[J]}{Area[cm^2] \cdot Duration[s]} \ , \qquad (12)$$

when the pulse energy, the focal spot size and the pulse duration are measured. When a laser pulse passes through a medium the motion of the electrons in the

medium will be perturbed by the electric field. In a linear medium the polarisation density, which is the sum over all dipole moments, is linearly dependent on the electric field:

$$\overrightarrow{P} = \varepsilon_0 \chi \overrightarrow{E} \ , \tag{13}$$

where χ is the electric susceptibility of the medium and ε_0 is the vacuum permittivity. The relationship between the electric susceptibility χ and the refractive index n is given by:

$$n^2 = 1 + \chi \ . \tag{14}$$

Equation (13) is comparable to the model of an harmonic oscillator, because each dipole moment $\mu = -ex$ is linearly dependent on the displacement x by which the electron is shifted. If the restraining force is not linearly dependent on the displacement, the polarisation density becomes a nonlinear function of the electric field. This occurs when the laser intensity exceeds the threshold intensity for nonlinear effects of the considered medium. Hence, no medium is purely linear, because at a certain intensity nonlinear effects will become visible in all media. The linear equation (13) can be expanded in a Taylor series for $E = 0$, because the atom potential will be strong even in comparison to high electric laser fields. The nonlinear equation for the polarisation density is:

$$\overrightarrow{P} = \varepsilon_0 \chi^{(1)} \overrightarrow{E} + \frac{1}{2}\chi^{(2)} \left(\overrightarrow{E}\right)^2 + \frac{1}{6}\chi^{(3)} \left(\overrightarrow{E}\right)^3 + ... \ , \tag{15}$$

where the additional terms are the n^{th}order nonlinearities with their corresponding n^{th}order nonlinear susceptibilities χ.

1.4.1 Optical Kerr-effect

A Kerr medium has an inversion symmetry which reduces the nonlinear equation to its uneven terms. The third order term will dominate the nonlinear polarisation density and can be written as

$$\overrightarrow{P_{NL}} = \frac{1}{6}\chi^{(3)} |\overrightarrow{E}(\omega)|^2 \overrightarrow{E}(\omega) \ . \tag{16}$$

Insertion of equation (11) for the electric field into equation (16) gives:

$$\varepsilon_0 \Delta\chi = \frac{\overrightarrow{P_{NL}}}{\overrightarrow{E}(\omega)} = \frac{1}{3} \cdot \eta_0 \cdot I \cdot \chi^{(3)} \ ,$$

where $\triangle\chi$ is the increase of the susceptibility, proportional to the electric field [9]. As χ changes because of the intensity also the refraction index n changes $\triangle n \approx \frac{\triangle\chi}{2n}$, so the refraction index in dependence on the laser intensity is determined by the equation for the Optical Kerr-effect:

$$n(I) = n + \frac{1}{6}\frac{\eta_0 \chi^{(3)}}{\varepsilon_0 n} = n + n_2 I \ . \tag{17}$$

The Kerr-effect influences the laser pulse spectrum via self-phase modulation and the beam profile through Kerr-induced self-focusing.

1.4.2 Self-phase modulation

When a laser pulse with a temporal Gaussian intensity profile passes through a Kerr medium, the refractive index will change due to the Kerr effect with the intensity and therefore the wave vector $k = \frac{n \cdot \omega}{c_0}$ will change [11]. In addition to the phase shift of $\phi = kL = \omega t$ generated when the laser pulse travels through a medium with the length L, the phase shift will change by $\triangle\phi(t) = \frac{\omega}{c_0} n_2 I(t) L$ due to the optical Kerr-effect [12]. For a Gaussian beam with the intensity $I(t) = I_0 \cdot e^{\left(-\frac{t^2}{\tau^2}\right)}$, the frequency shift can be calculated from the phase shift using

$$\omega(t) = \frac{d\phi(t)}{dt} = \frac{d(\omega_0 t - n\frac{\omega}{c_0} - n_2 \frac{\omega}{c_0} I(t) L)}{dt} \ ,$$

$$\Longleftrightarrow \omega(t) = \omega_0 + \frac{2\omega n_2 L I_0}{c\tau^2} \cdot t \cdot e^{-\frac{t^2}{\tau^2}} \ ,$$

where τ is the FWHM pulse duration. Mostly, the value n_2 is positive which leads to a red shift on the rising edge of the pulse and a blue shift on the falling side of the pulse. As there is a nearly linear modulation of the frequencies in the central part of the pulse the pulse is positively chirped. In contrast to a chirp, which is introduced by dispersion, the frequencies are not only shifted, but new frequency components are created and added to an already existing spectrum.

1.4.3 Kerr-induced self-focusing

Kerr-induced self-focusing occurs if a threshold power, also called critical radiation power, is exceeded:

$$P_{cr} = \alpha \cdot \frac{\lambda^2}{4\pi n_0 n_2} \ ,$$

where α is a constant for the beam profile, which is for a Gaussian beam $\alpha = 1.8962$ [13]. For laser profiles with a transverse electromagnetic 00 mode (TEM_{00}), the laser intensity decreases with increasing distance from the central axis. Thus, as mostly all materials have a positive value n_2, the overall refractive index is highest at the central beam axis. As the beam is diffracted to higher refractive indexes the medium acts as a focusing lens. The effect of plasma defocusing [14] is able to cancel out the effect of Kerr-induced self-focusing at a certain pressure value [15].

1.5 High Harmonic Generation (HHG)

1.5.1 Corkum model

The Corkum model describes the high harmonic generation process with two main assumptions. First, the electrons do not interact with each other and second, the electron of the ionised atom is treated as a free particle. With the three step model the interaction of the electron with the coulomb potential and the laser field is described in a simple way by separating the process into three steps: the ionisation, acceleration and recombination. The electrons are bound in the atomic potential of the HHG medium (usually a noble gas). When the atom is exposed to a strong laser pulse the coulomb potential is deformed (see figure 2). The potential is diminished and the electrons can tunnel through the barrier. After this ionisation process the free electron is accelerated in the electric field of the laser away from the ion. The electron can be assumed to be completely freed from the atomic potential. When the electric field of the laser changes its sign the electron is accelerated back towards its parent ion until they recollide. With the absorption of the electron the atom emits a photon with the recombination energy from the atomic potential plus a multiple of the laser photon energy. It should be noted that only in the case of linear polarised light can the electron be led back to its atom. This acceleration process is described by classical physics, whereas the ionisation and absorption of the electron are described by quantum mechanics. Therefore the Corkum model is a semiclassical theory.

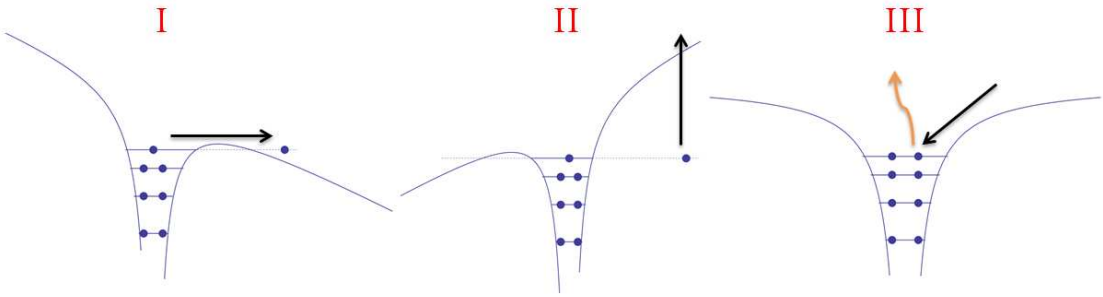

Figure 2: Schematic of the 3 step model: (I) ionisation, (II) acceleration and (III) recombination. The harmonic radiation (orange) is emitted after recombination of the electron with the ion.

There are three different types of ionisation processes possible: the multiphoton ionisation, the tunnelling ionisation and the barrier-suppression ionisation. For the multiphoton regime the applied electric field amplitude is small compared to the electric field of the atomic potential. Thus, it is necessary for the electron to absorb several photons to gain enough kinetic energy to leave the atomic potential. In the regime of barrier-suppression ionisation the electric field amplitude is large, so that the atomic potential barrier is suppressed.

In this case the electrons can leave the potential easily and all atoms of the ensemble become ionized. The HHG process takes place in the tunnelling regime. To distinguish between those three regimes, the Keldysh parameter is used. It is defined as

$$\gamma = \sqrt{\frac{I_P}{2U_P}} ,$$

where I_P is the ionisation potential and U_P is the ponderomotive potential. The Keldysh parameter can be used to estimate the ionisation regime. The multiphoton regime is limited to a Keldysh parameter of $\gamma > 1$ and the tunnelling regime is limited to $\gamma < 1$. The ponderomotive energy is the time averaged kinetic energy the electron gains through the acceleration in the electric field of the laser pulse. In order to calculate the ponderomotive energy, the velocity of the electron is calculated by integration over the accelerating force:

$$F = m \cdot \frac{dv}{dt} = eE_0 e^{-i\omega t} \Rightarrow v = \int \frac{eE_0}{m} e^{-i\omega t} dt = -\frac{eE_0}{i\omega m} e^{i\omega t} .$$

From the average velocity the kinetic energy is obtained. By insertion of the constants of nature and transformation of the electric field to intensity and frequency to wavelength, the following simplification can be derived for the ponderomotive energy. Thus, the maximum photon energy is defined as

$$U_P = \frac{1}{2} m v_{average}^2 = \frac{e^2 E_0^2}{2m\omega^2} \approx 9,33 \cdot 10^{-14} \cdot I \left[\frac{W}{cm^2}\right] \cdot (\lambda[\mu m])^2 . \qquad (18)$$

The final photon energy is a combination of the ionisation of the HHG medium and the ponderomotive energy:

$$E_{cutoff} \approx I_P + 3.17 \cdot U_P . \qquad (19)$$

This is the so called cutoff law [16].

1.5.2 Harmonic spectrum

The generated single-atom harmonic spectrum can be distinguished into three regions: the perturbative regime for the low order harmonics, the plateau region where the intensities of the harmonics are of the same magnitude and the cutoff region, where the intensity of the highest order harmonics drop to zero. In order to calculate the intensity of the lower order harmonics the lowest-order perturbative theory is used, whereas the intensities of the higher harmonics can be calculated with the strong field approximation (SFA). A purely quantum mechanical description of the SFA is the Lewenstein model [17].

A characteristic of the HHG process is that only odd harmonics are produced. This is due to the symmetry of the electric field, because when the

electric field changes its sign the coulomb potential of the atoms is distorted in the other direction and the bound electrons have the possibility to tunnel through the barrier in the other direction. Hence, the recombination occurs every time when the electric field of the driving laser crosses the zero-point (see figure 3). Therefore the pulse distance is $\frac{T}{2}$; the Fourier transformation yields a frequency separation of $\Delta\omega = 2$. Another explanation is that two photons have to be absorbed by the atoms because of the inversion-symmetry of the HHG medium, which is usually a noble gas. For some kind of molecules the symmetry of the potential is broken and it is possible to generate even harmonics.

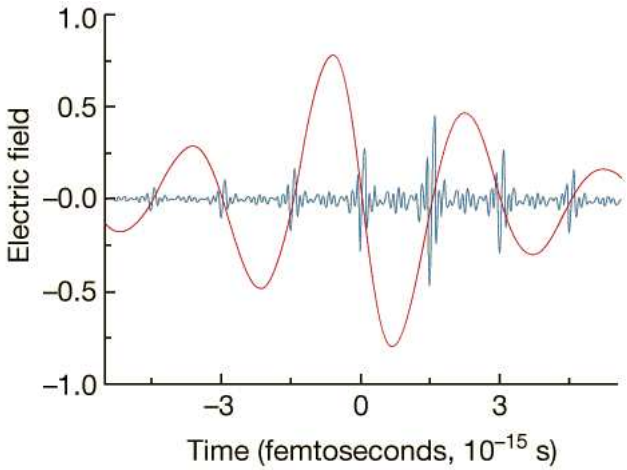

Figure 3: Temporal evolution of a generated train of attosecond pulses (blue line). These pulses are emitted twice per laser cycle (red line) [18].

1.5.3 Short and long trajectories

The "birth time" of the electron corresponds to a phase of the electric field at which the electron tunnels through the barrier. This phase is the only parameter defining the achievable kinetic energy during the acceleration. After the ionisation the electron has three options. One option is that the excited electron can depart further so that it will never recombine with its parent ion. The other two options lead to HHG radiation. The electron paths in one cycle of the driving laser are distinguished into short and long trajectories (see figure 4), where the ionisation for a long trajectory is directly after the peak of the electric field from 0 to $0.05\,T$ and for a short trajectory from $0.05\,T$ to $0.25\,T$ [19]. Here T is the time the electric field needs for one oscillation, which can be simply calculated from its frequency.

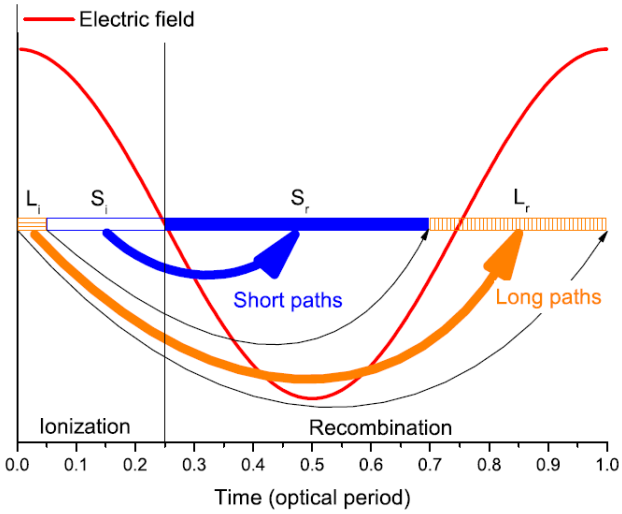

Figure 4: Schematic plot of the time resolved HHG-process. The electron paths are divided into short (blue) and long (orange) trajectories. [19]

After the electric field changes its sign at $0.25\,T$ the electron is accelerated back to its atom so that the last freed electron directly recombines. The largest kinetic energy $E_{kin} = 3.17 \cdot U_P$ is reached by those electrons which are ionized at $0.05\,T$ and have a travelling time of $0.65\,T$ so that they recombine at $0.7\,T$. As this trajectory is the border between the short and the long paths, the kinetic energy of the short trajectories decreases to shorter paths, whereas for long trajectories the kinetic energy decreases to longer paths.

1.6 Phase Matching

In the previous chapter the HHG process was considered in the picture of the single atom response. In order to describe the real HHG process, it is necessary to take into account the macroscopic effects from the whole ensemble of gas atoms. The generation process is limited by the fact that the driving laser and the generated harmonics experience different phase advances, which leads to destructive interference after one coherence length L_C. The coherence length is defined as

$$L_C = \frac{\pi}{|\triangle k|} \,,$$

where $|\triangle k|$ is the wave vector mismatch between the driving laser and the created harmonic [20]. It is also called k-vector mismatch and can be calculated by

$$|\triangle k| = |k_q - q \cdot k| \,, \tag{20}$$

where k_q is the wave vector of the qth order harmonic and k is the wave vector of the driving laser. Thus, the phase advance of the driving laser and the

considered harmonic have to be calculated. Since the HHG process takes place in a gas target there are different effects accumulating to the phase advance: the neutral gas dispersion, the plasma dispersion as well as a phase shift due to the beam geometry:

$$k(\lambda) = k_{vac}(\lambda) + k_n(\lambda) + k_p(\lambda) + k_{geom}(\lambda) \ ,$$

where $k_{vac}(\lambda) = \frac{2\pi}{\lambda}$ is the wave vector in free space. The term $k_{geom}(\lambda)$ is the Gouy phase shift, which can be calculated with equation (5). Its contribution to the wave vector mismatch is always negative [20]. However, the other two terms of the phase advance are due to dispersion, which depends on several factors, for example, the gas pressure and the tunnelling rate. Hence, these terms depend on the gas type and the achieved laser intensity.

The neutral gas dispersion delivers a positive contribution to the wave vector mismatch, as the index of refraction is higher in the visible than in the XUV-regime [21]. In the 1D simulation presented in chapter 4 the following formula is used to calculate the neutral gas dispersion:

$$\triangle k_n = \frac{2\pi \cdot q}{\lambda_{central}} \cdot (1 - \eta) \cdot p \cdot \triangle n \ , \tag{21}$$

where η is the ionisation fraction and p is the HHG gas pressure. The difference of the refractive index n between the driving laser and the q^{th} harmonic is given by $\triangle n$.

The plasma dispersion is based on the refractive index, which is introduced by free oscillating electrons:

$$\triangle k_p = -N_e r_e \lambda_{central} = p \cdot N_{e-norm} \cdot \eta \cdot r_e \cdot \lambda_{central} \cdot \frac{(q^2 - 1)}{q} \ , \tag{22}$$

where p is the gas pressure and N_{e-norm} is the free electron density at standard state, η is a factor for the free electron density which corresponds for the HHG gas to the fraction of ionised to neutral atoms. For completely ionised hydrogen η is a factor of two, due to the fact that each molecule delivers two electrons. In both equations (21) and (22) the wavelength dependence of the dispersion is given by the harmonic number q [22]. This contribution of the plasma dispersion to the wave vector mismatch is always negative.

1.7 Absorption

The HHG process is carried out in vacuum, because at standard atmosphere pressures, the generated XUV radiation would be directly absorbed by the gas atoms and molecules. The obtained spectral intensity distribution is strongly dependent on the absorption, which takes places between the point of generation and the spectrometer. To compare the effects on different kinds of gases

the absorption can be calculated with the Henke tables [23]. This is done for different interaction lengths and gas pressures. Typical HHG gases are argon, neon or helium, and as the QPM foil target tunes the phase shift with hydrogen the transmission of these four gases are compared in figure 5. The selected pressure for this plot is 10 mbar, which is just a very rough estimation as there were no measurements done to determine the actual pressure at the exit of the nozzles. An interaction length of 2 mm is chosen for the plot as the target with 13 nozzles has a length of 1.3 mm from which the gas will expand. So this calculation is a worst case scenario where the XUV radiation is generated at the beginning of the gas jet. In addition to the absorption in the jet there will be some residual gas in the vacuum chamber between the target and the spectrometer where the radiation can be absorbed or scattered. As visible in figure 5 the transmission of XUV radiation is strongly dependent on the type of applied gas. Whereas the HHG gases have hard absorption edges the transmission efficiency of hydrogen monotonously decreases to 80 % over the spectral range from 1 to 62 nm and thus has only a small effect on the obtained spectrum. The transmission efficiency of the HHG gases is far smaller compared to hydrogen. For example, the transmission of helium and neon have minima of ca. 70 % and especially for Argon the transmission drops below 20 % for wavelength longer than 40 nm.

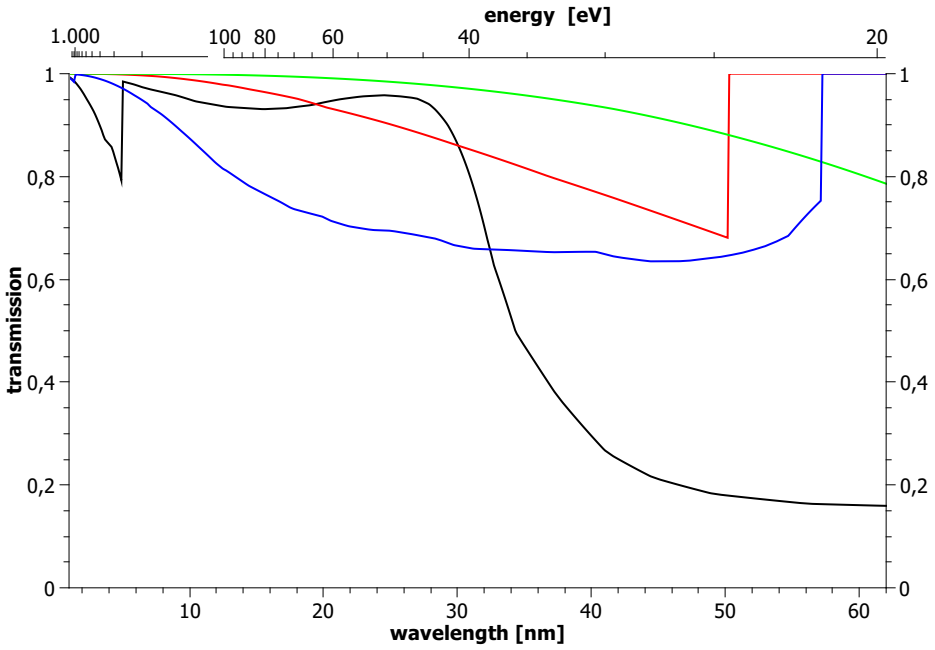

Figure 5: Transmission curves of argon (black), helium (red), hydrogen (green) and neon (blue) in dependence on the radiation wavelength. The gas pressure is 10 mbar for an interaction length of 2 mm. [23]

1.8 Quasi-Phase Matching

Quasi-Phase Matching (QPM) is a mechanism to increase the conversion efficiency of the HHG process. It is based on suppressing the HHG process in regions, where the phase of the harmonic radiation would destructively interfere. Furthermore the wave vector mismatch $\triangle k$ between the driving laser and the generated harmonic radiation has to be tuned in this suppression region. Due to destructive interference the intensity of the HHG radiation is limited to a phase advance of $|\triangle k| \cdot l = \pi$ or uneven higher orders $|\triangle k| \cdot l = n \cdot \pi$, where l is the propagation distance. Thus, it is necessary to suppress the generation of radiation for phases between π and 2π. After a phase advance of the wave vector mismatch of 2π another HHG source is added so that the intensity can coherently increase. Hence, the generated signal from a QPM target will be larger than the signal of a single HHG target by a factor specified by the number of the deployed single nozzles. Several different methods proved this principle successful such as the periodic variation of the diameter of a capillary to modulate the laser intensity [24, 25] or multi mode beating in a capillary [20, 26]. If the harmonic energy is limited by the phase mismatch, it is possible to increase the energy by repeating the quasi-phase matching pattern until other limiting factors are reached. These could be macroscopic effects like the reabsorption of the generated radiation as well as plasma defocusing or the deformation of the driving laser pulse. If the harmonic energy of an HHG target is limited by absorption in the HHG medium no further enhancement can be achieved through QPM. The limitation due to absorption in the typical HHG gases, argon, neon and helium decreases at shorter wavelengths (see figure 5). In the case of similar nozzles without any destructive effects the enhancement factor is quadratic depend on the number of HHG nozzles as the HHG intensity is quadratic dependent on the HHG gas density [27, 28, 29]:

$$I_q \alpha N_a^2 \frac{sin^2\left(\frac{\triangle kL}{2}\right)}{\left(\triangle k\right)^2} \ , \tag{23}$$

where N_a^2 is the number of radiating atomic dipoles and L is the interaction length.

1.8.1 The dual-gas target

To suppress the HHG process completely in the region of destructive interference a second kind of gas with a lower ionisation potential and a smaller atomic radius could be used. The QPM mechanism of the dual-gas target applies noble gases such as argon or neon as the HHG medium and in the matching zones hydrogen. When the applied laser intensity is high enough, $I > 3 \cdot 10^{14} \frac{W}{cm^2}$, the hydrogen gas will be completely ionized due to tunnel ionisation and barrier-suppression ionisation. Due to the fact that the atomic radius of hydrogen is

small compared to other atoms, the electron has a smaller probability to recombine with its parent hydrogen ion. Therefore the ionized hydrogen gas is a passive medium, which contributes a phase shift to the passing radiation [30]. The interaction with the free electrons leads to plasma dispersion. The phase shift due to plasma dispersion can be described by the following simplified formula

$$\phi_q \propto q L_M n_e r_e \lambda \,, \tag{24}$$

where r_e is the classical electron radius and λ is the fundamental wavelength. Therefore, the phase advance of the qth harmonic is only proportional to the interaction length L_M and the electron density n_e. Hence, the phase advance in the hydrogen zone can be easily tuned by varying the hydrogen backing pressure and accordingly the free electron density. The dual-gas target design gives also the opportunity to vary the length and width of each nozzle, so that the phase advance in the matching zone can be roughly defined before finely tuning the pressure. Already proven designs had a width of 200 μm or 800 μm with a length of 100 μm (see figure 6).

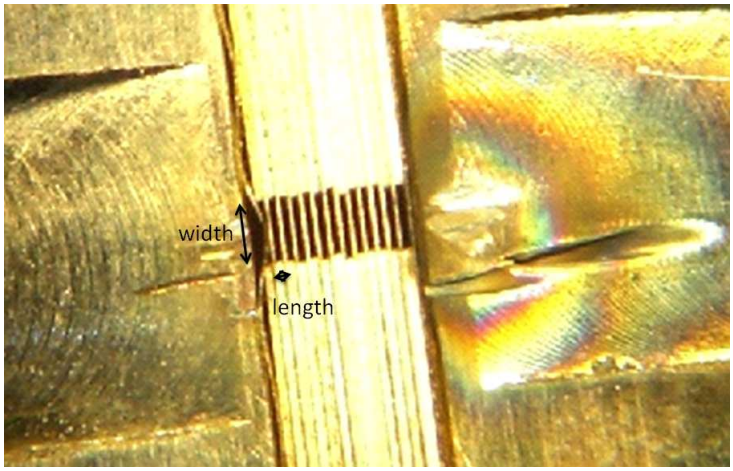

Figure 6: The dual-gas foil target in top view. Each nozzle has an opening of $100\mu m$ x $800\mu m$.

1.9 FLASH

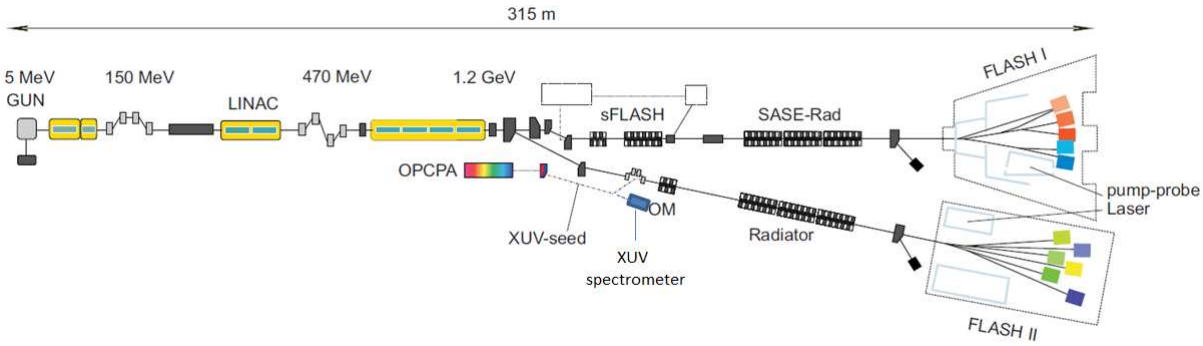

Figure 7: Design of FLASH with the extension FLASH2. The position of the optical parametric chirped pulse amplifier, the XUV seeding target as well as the XUV spectrometer are shown. (Courtesy of F. Tavella)

FLASH (Free-Electron Laser in Hamburg) is a high gain FEL, which produces radiation in the range from 4 to 60 nm with more than 100 $\frac{\mu J}{pulse}$ in 10 Hz mode. The electron bunches of FLASH can have a repetition rate of 1 MHz in each 10 Hz burst. Therefore the number of bunches per clock pulse can be varied from one single bunch to bunch trains with more than 800 bunches.

Due to the high request of beam time at FLASH and the aim to further improve the beam quality, the extension FLASH2 has gone into construction in the year 2011. A schematic of the linac section of FLASH and the two beamlines ending in the experimental halls of FLASH1 and FLASH2 is presented in figure 7. FLASH2 is build at a small angle to FLASH behind the linac section, so that it can be supplied with bunches from the FLASH linac simultaneously. This will be done by a kicker which can be operated in two different modes. Either each bunch train is split and supplied to both beamlines by conservation of the initial repetition rate of 10 Hz or every second whole bunch train is kicked to FLASH2 so that both beamlines are supplied at a repetition rate of 5 Hz.

The electron bunches of FLASH are created by laser pulses, with a wavelength of 262 nm, on the surface of a Cs_2Te photo cathode. Afterwards they are accelerated and compressed. The electron beam passes through a transverse and an energy collimator to cut off electrons with a big transverse displacement and to erase the dark current. Finally the transverse and longitudinal compressed bunches enter the undulators. The FLASH accelerator modules are based on superconducting technology, which gives the advantage that due to the lack of resistance nearly no heat energy is deposited in the cavity. Thus, the cavities can operate at high repetition rates with a large field gradient. Originally, these modules where developed for the linear collider project (Teraelectronvolt Energy Superconducting Linear Accelerator (TESLA)). The design field gradient for these modules was about 23.4 $\frac{MV}{m}$, but after a few years of research

the field gradient could be further improved and some of the newest models have gradients of over 35 $\frac{MV}{m}$. This is an important factor in order to decrease the length of the whole accelerator [31]. FLASH is equipped with seven acceleration modules and reaches actually a maximal energy of 1.2 GeV, which results in a soft x-rays from the undulators of down to 4.12 nm [32]. This enables experiments in the water window, between 2.34 nm and 4.4 nm, where the radiation can be used to examine biological structures. It is called the water window, because water is transparent in this regime, whereas atoms like nitrogen and carbon, main components of biological structures, have a great absorption cross-section.

The phase and amplitude of the standing waves inside the accelerator modules define the energy chirp of the electrons in a bunch. This energy chirp is used in the so called bunch compressors to create very short bunches. Due to the adjusted energy chirp, the electrons which reach the bunch compressor first have less energy than the electrons at the end of the bunch. In the bunch compressor, which is a magnetic chicane, the electrons with less energy will be diverted stronger. Thus, their path through the bunch compressor is longer than the path of more energetic electrons, resulting in compression.

1.9.1 Seeding at FLASH

If the FEL amplification process is based on self-amplified spontaneous emission (SASE), the spectrum, the pulse energy, the pulse duration and the arrival time of the generated radiation will vary from pulse to pulse. All these parameters are influenced by the generation process of the electron bunch and its acceleration. For example, the arrival time fluctuations of the generated radiation depends on the arrival time fluctuations of the electron bunch at the undulator section. For FLASH the arrival time jitter is in the order of several tenth of fs [33]. The SASE amplification process starts from a random modulation of the charge distribution in longitudinal phase space. This so called shot noise can be assumed at any time due to the fact that the number of electrons in a bunch is limited. The pulse duration, the spectrum as well as the pulse energy depend on the charge distribution within the electron bunch and will therefore diver from shot to shot. In the worst case the charge distribution is so inhomogeneous that several single radiation pulses are generated in the undulator.

In order to reduce the shot-to-shot variation of the radiation, the incoming electron beam can be overlapped with an external electromagnetic wave with a central wavelength of λ_l. The overlap has to be achieved in transverse and longitudinal space as well as the bandwidth of the seed radiation should fit to the bandwidth of the FEL as only the radiation within this wavelength regime is amplified. When the overlap with the electron beam and the energy of the external wave is sufficient the SASE process will be dominated by the

amplified seed radiation. Hence, the resulting electromagnetic wave has the advantage of both systems, which are the controlled arrival time and spectrum of the seed radiation as well as the high pulse energy from the amplification process in the undulator. There are 4 different kinds of seeding possible: direct seeding, self seeding, seeding with High-Gain Harmonic Generation (HGHG) or Echo-Enabled Harmonic Generation (EEHG). All these methods already proved functional, for example HGHG was achieved in the infrared regime with a wavelength of $5.3\mu m$ at the Accelerator Test Facility at Brookhaven National Laboratory [34] or at NSLS at around 266 nm [35].

The sFLASH (seeding-FLASH) project pursues the concept of direct seeding, although self-seeding was also considered [36] for FLASH. The sFLASH objective is to demonstrate the first direct seeding of an FEL in the XUV regime. To generate an electromagnetic seeding wave in this regime a laser system with a wavelength of 800 nm and a pulse length of 35 fs with 50 mJ pulse energy was generated to be used on a HHG target. The HHG target is a single nozzle in a vacuum chamber, which creates a free argon jet with a length of 20 mm. The highest intensity was measured for the 21^{st} harmonic, which is about 38 nm. This harmonic is transported to the sFLASH undulator by several mirrors, which reduces the intensity of the seeding wave to 5 % of its original value. To overlap the seeding XUV beam with the electron beam it is focused into the first undulator section of the variable gap sFLASH undulators. Both beam positions are checked by beam position monitors (BPMs) and wire scanners [37]. For standard SASE operation of FLASH another undulator section is used, therefore the sFLASH undulators have to be fully opened, so that the electron path is not affected by their magnetic field.

The sFLASH project also includes "pump-probe" experiments. "Pump-probe" means, that the atomic structure under observation is first excited by a pump pulse and is then sampled by the probe pulse. Therefore, the probe pulse illuminates the same target after some variable time delay. Thus, for example the decay time of an excited state of a molecule can be determined by scanning the transmission efficiency in dependence of the time delay.

1.9.2 Seeding at FLASH2

Direct seeding is planned to be another optional operation mode for FLASH2. The seeding laser laboratory is situated at the beginning of the FLASH2 section (see figure 7), whereas the HHG setup and the spectrometer will be installed inside the tunnel. Similar to the sFLASH project XUV pulses will be generated by a laser interacting with an HHG target. The generation process is based on quasi-phase matching in order to improve the conversion efficiency. The laser system, which is described in the next section, will produce 10 Hz bursts of pulses, with a repetition rate of 100 kHz, synchronized to the 10 Hz bursts of FLASH [3]. For the seeding process it is necessary to achieve a high conversion

efficiency as the electromagnetic seeding wave has to be more intense than the spontaneous radiation of the electrons in the undulator. In reference [38], the shot noise power (spontaneous radiation power) in the first undulator section of FLASH2 for an electron bunch with a duration of 200 fs was computed. In order to achieve the same energy level with the seeding wave at that wavelength, the necessary energy at the harmonic source point was then calculated. This was done with respect to transmission losses from the harmonic source to the undulator. The assumed mirror reflectivity efficiency in the XUV regime was 65 %. Furthermore an additional factor of 100 is multiplied to the calculated energy in order to dominate the shot noise power. Thus, with this high contrast the seeding wave will exceed the shot noise by two orders of magnitude. As a direct diagnostic tool for XUV seeding pulses, especially for the pulse intensity, an XUV spectrometer was developed. The spectrometer enables measurements of the divergence and of the absolute energy for the whole spectral seeding range from 10 to 40 nm for FLASH2.

1.9.3 The FLASH2 seeding laser system

The seeding laser system is based on the principle of Optical Parametric Chirped-Pulse Amplification (OPCPA) [3]. Optical parametric amplification is a non-linear process such as second harmonic and sum frequency generation, where a signal pulse is amplified by energy conversion from a high energy pump pulse. The pump pulse with the frequency ω_p and the broadband signal pulse with centre frequency ω_s are spatially and temporally overlapped inside a crystal. Because of the nonlinear interaction, a part of the pump photons are split into ω_s and ω_i, where ω_i is the frequency of the idler beam. The energy is conserved by the production of the idler photons: $\hbar \cdot \omega_i = \hbar \cdot \omega_p - \hbar \cdot \omega_s$. Thus, with appropriate phase matching conditions energy will be transferred from the pump beam to the signal beam .

A Titanium:Sapphire Oscillator is used to seed the laser system (see figure 8). The oscillator beam is split in two parts: a broadband signal beam at $\lambda_{center} = 760\,nm$ (OPA seed) and a pump seed, which is frequency shifted to $\lambda = 1030\,nm$. The pump beam is first stretched to a duration of about 2.2 ns in a grating compressor and afterwards amplified to a pulse energy of about 20 mJ. This is called chirped pulse amplification as the stretched pulse has a frequency chirp. After the amplification with an Innoslab amplifier [39] and a thin-disk amplifier the pulses are compressed to a pulse duration of 1 ps. The required pump wavelength of $\lambda_p = 515\,nm$ is generated by second harmonic generation (SHG) in a BBO-crystal. The broadband signal beam is then amplified by the pump beam in a 2-stage OPA setup to a pulse energy of about 2 mJ. Afterwards the laser pulses are compressed to a pulse duration of 15 fs and coupled into the HHG target vacuum chamber.

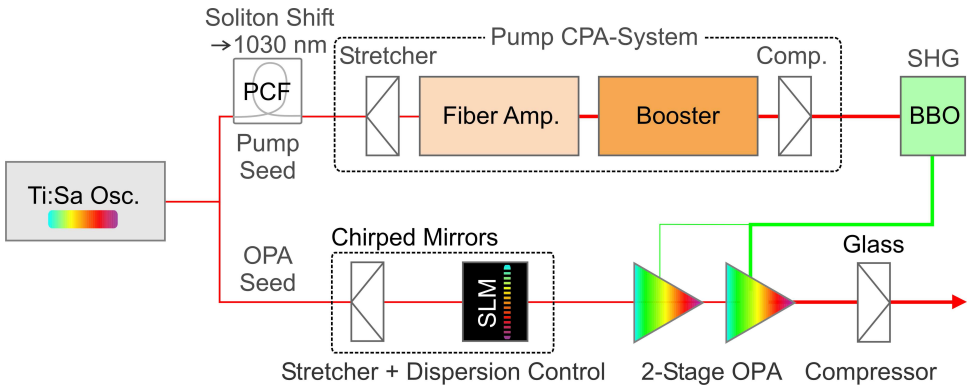

Figure 8: Schematic drawing of the seeding laser system of FLASH2 (courtesy of R. Riedel). The laser beam from the oscillator is split into two parts. One part is used to seed the OPA pump amplifier system, whereas the other part is used as signal pulse for the optical parametric amplification.

2 The XUV spectrometer

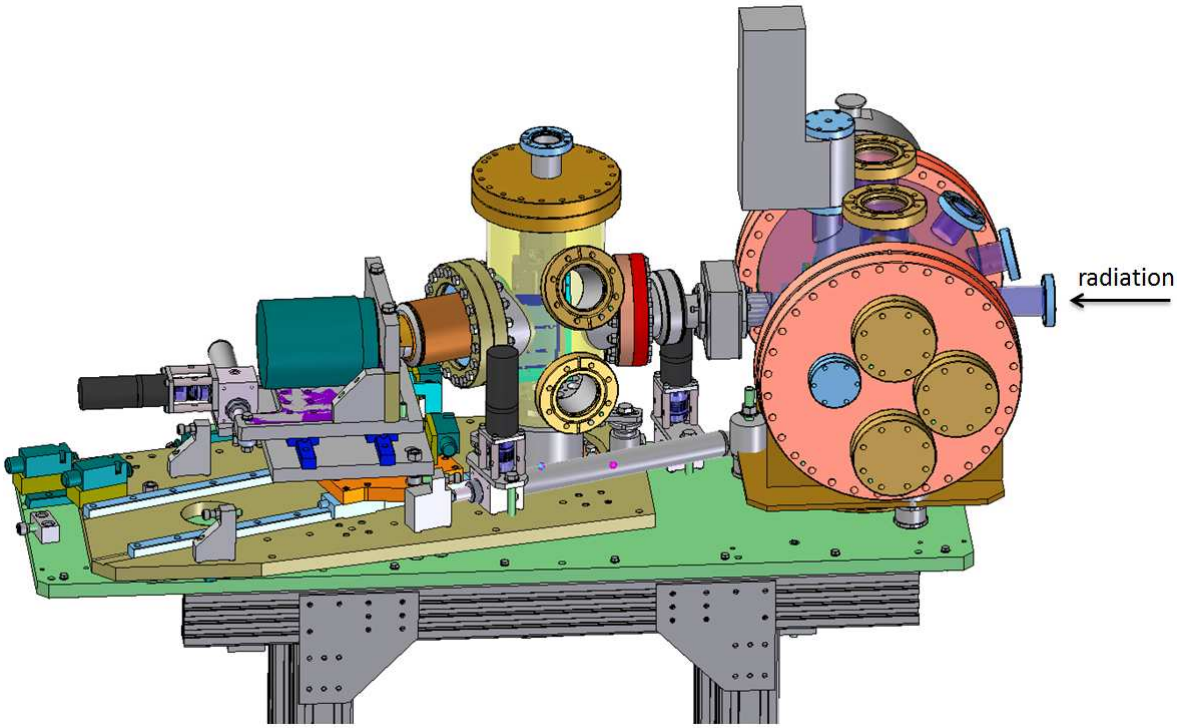

Figure 9: Design of the XUV Spectrometer. The radiation enters the vacuum chamber from the right hand side. This chamber contains filter wheels, an XUV diode and a shutter. The second vacuum chamber is equipped with gratings and is connected to a CCD camera (turquoise) via a flexible bellow (brown). A high precision slit is positioned in between the two vacuum chambers.

2.1 Motivation for the special XUV spectrometer

In order to seed FLASH2 it is necessary to generate pulses with a high intensity to overcome the SASE effect of the FEL. Hence, the seed pulses have to be characterised with a spectrometer, which has to be installed in the FEL tunnel. For this purpose software and hardware was developed to remotely control the spectrometer. Seeding is planned for a spectral range from 10 - 40 nm and therefore the spectrometer should cover this range. Thus, it is equipped with three concave flat-field gratings, which resolve a spectral range from 1 to 62 nm. Furthermore, because the seed radiation has to be focused into the first undulator section, it is crucial to know the divergence of the XUV beam. Therefore, the spectrometer is equipped with a slit in front of the gratings. The slit will be also necessary when the spectrometer is installed at FLASH2, because of the large distance to the source point of the XUV radiation. The

mechanics of the spectrometer are easily adaptable to different alignments, so that it can be deployed for experiments with different target setups in several labs. The final design is shown in figure 9.

2.2 The flat-field spectrograph

One problem of XUV diagnostics is the low reflectivity of mirrors or gratings at these wavelengths. To maximize the efficiency it is necessary to work at small glancing angles. The glancing angle is measured between the grating and the incidence beam. With a common concave grating, the XUV radiation would be focused at points on the Rowland Circle. The size of the Rowland Circle is defined by the curvature of the grating and its position is defined by the positions of the grating and the sample, because these have to be also situated on that circle. Such a conventional concave grating with uniformly spaced grooves is not sufficient to analyse a big spectral range or the spatial shape of an XUV pulse [40]. In order to resolve the whole spectral range with such a grating, the spectrum has to be scanned in several steps with one detector or several detectors positioned at the Rowland Circle. The solution is to focus the whole spectral range on a plane with a concave flat-field grating with a variable line space. The uniformity is important because otherwise scattered light is produced [41]. These concave spherical variable line space (SVLS) gratings combine focusing and diffraction in one single optical element. As the created spectrum is now focused in one plane, the whole spectral range can be resolved with a CCD camera in a single shot. The gratings (see figure 10) used in this spectrometer, were produced by Hitachi High Technologies America, Inc.[42].

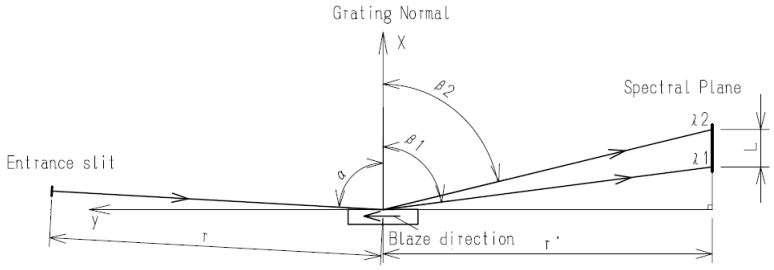

Figure 10: Working principle of the grating with the design parameters r (distance between slit and grating), r' (distance between grating and image plane),α (incidence angle of the radiation) and L (spectral range, which is focused)[42].

wavelength range [nm]	grooves per mm	r [mm]	r‘ [mm]	L [mm]	α [°]
1-5	2400	237	235,3	19,99	88,7
5-20	1200	237	235,3	25,30	87,0
11-62	1200	350	469	110,16	85,3

Table 1: Design parameters of the gratings, where the wavelength range is the focused spectral range imaged onto a plane with the length L

The spectrometer consists of three gratings with different spectral ranges. They are installed on a linear stage (LTM60, OWIS GmbH), to ensure a remote controlled grating change. The gratings are defined by the following: spectral range, grating constant, the distances at which they should be positioned between the slit and the CCD camera, the length of the flat-field image on the CCD camera and also the required incidence angle of the beam. These parameters are listed in table 1. The gratings are mounted on a linear stage by a special holder shown in figure 11, which ensures the required incidence angle α for each grating.

As given in table 1, the image size on the CCD camera is up to 110.16 mm and due to a chip size of only 13.3 mm, it is essential to scan the whole range with the CCD. To be able to scan automatically from 1 to 62 nm, it is necessary to the change of the gratings, to vary the length r and r’ and to move the camera. These distances are controlled by three translation motors and six end switches.

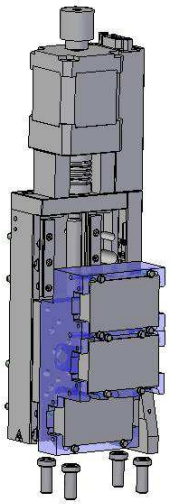

Figure 11: Design of the gratings, the grating holder (blue) and the linear stage. The topmost grating is the 5-20 nm grating, in the middle is the 1-5 nm grating and at the bottom the 11-62 nm grating.

2.3 The alignment procedure

Several steps are necessary to align the spectrometer. First, the incoming beam has to be centred on the incoupling flange of the first vacuum chamber of the spectrometer. The distance r of the grating to the slit has to minimized with the first motor and the grating holder corner has to be positioned between the 1-5 nm grating and the 11-62 nm grating. Then the spectrometer has to be rotated until one quarter of the direct beam is masked on the alignment blank sheet at the back of the spectrometer. Afterwards the alignment blank sheet can be removed and the CCD camera can be installed. The position of the XUV source and the alignment of the beam can be tested by moving the CCD camera into the direct XUV beam. Therefore the grating holder has to be moved out of the beam path, which is possible when it is moved to the top most position. Now the XUV beam profile, position and intensity can be improved by steering the beam with the focusing mirrors and by optimizing the target position.

2.4 Grating reflectivity efficiency

In order to be able to define the measured energy for every wavelength it is necessary to know the grating reflectivity efficiency. The determination of the grating efficiency was performed with two different programs. The simulation results were compared to experimental results and to the efficiency curves, which were provided by the vendor. This was done in order to determine the efficiency as accuratly as possible. Furthermore, the error of the efficiency was determined through the comparison of the experimental results and the simulated values. The first simulation was done with the program GSolver. The results of this simulation for all three gratings are shown in figure 12. The refractive index in the parameter file of GSolver had to be extend to the region of 1 nm to 62 nm because the refractive index of gold was limited in the code to a spectral range from about 200 nm to 2500 nm. The concave shape and the spherical variable line space could not be considered in the simulation. Due to these restrictions, the results may have some errors. Another simulation program called PCGrate, which was limited to wavelengths longer than 17 nm, delivered values similar to the GSolver.

Certainly, the simulated efficiencies are greater than the actual values, because the simulations are done for perfect gratings without any dirt or damages on the surface. In addition, the manufacturing process has to be taken into account. Some errors of the manufacturing process are due to the fact that replicas are produced from a former developed master grating. These replicas mostly do not have exactly the same properties and their roughness can vary. Compared to the master grating their roughness will be more coarse, which leads to a different reflective behaviour and more scattered light [8]. In refer-

ence [43], the measured reflectivity values for the Hitachi gratings 0437 (5-20 nm) and 0450 (1-5 nm) are presented (see figure 13). A comparison of these efficiency curves with the provided curves from the vendor show a great consistency. The highest efficiency of the 5-20 nm grating is measured at around 11.4 nm with a maximum of 17.8 %, whereas the simulation with GSolver (figure 12) shows a maximum at 10.2 nm with 38.5 %. The actual reflectivity of the grating is therefore only half the simulated value, but the relative behaviour of the reflectivity fits very well to the measurements. The highest efficiency of the 1-5 nm grating is measured at about 2.2 nm with 2.1 % and a saddle point can be seen at 10 nm. However, in the simulation, the highest efficiency is measured at 10 nm with 10 %. In conclusion, the simulation with GSolver delivers too large efficiencies values for all gratings. The simulated profile of the 5-20 nm fit to the measured one, whereas the curve profile of the 1-5 nm grating does not fit for wavelengths shorter than 10 nm. Hence, the simulated values of the 1-5 nm grating are not reliable.

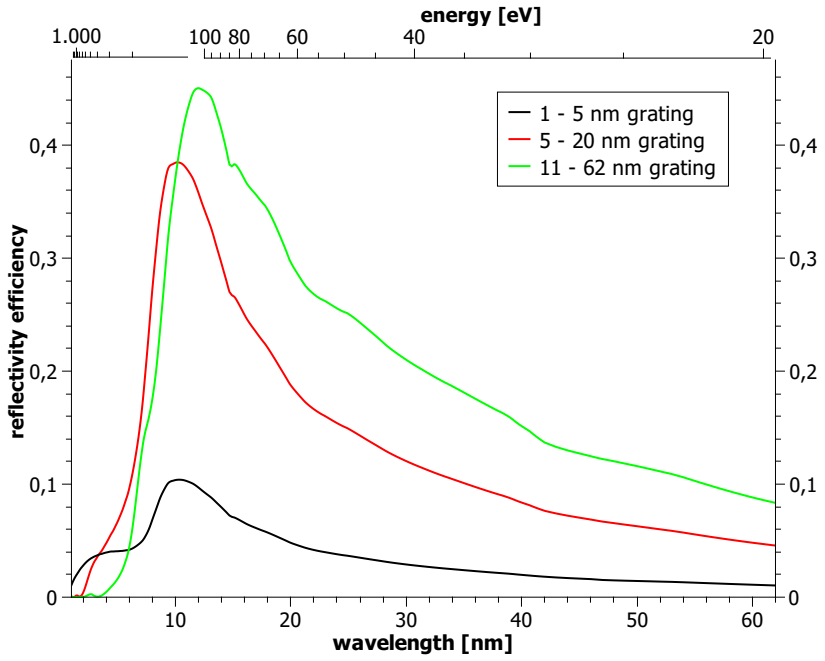

Figure 12: Simulated first order diffraction reflectivity efficiency with GSolver for the 1-5 nm grating (black), the 5-20 nm grating (red) and the 11-62 nm grating (green).

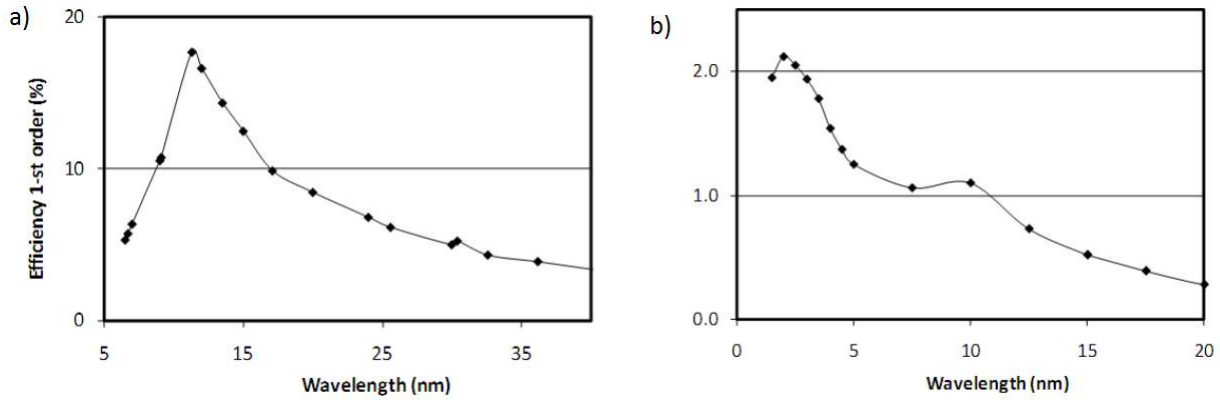

Figure 13: Measured efficiency of a) the 5-20 nm grating and b) the 1-5 nm grating. [43]

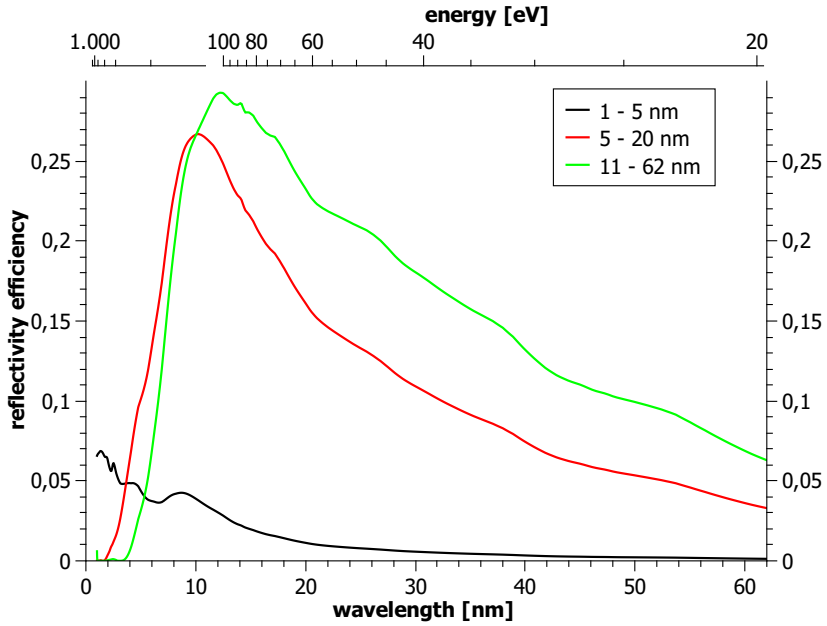

Figure 14: Simulated first order diffraction reflectivity efficiency with REFLEC for the 1-5 nm grating (black), the 5-20 nm grating (red) and the 11-62 nm grating (green).

In addition, simulations were carried out with "REFLEC - a program to calculate VUV/X-RAY OPTICAL ELEMENTS and SYNCHROTRON RADIATION BEAMLINES", which was developed at BESSY by Dr. Schäfer et al. [44]. The input parameters for this simulation were exactly the same as for GSolver. The maximum efficiency of the 5-20 nm grating is calculated at 10.3 nm, which is nearly the same value as from the simulation with GSolver.

However, the maximum efficiency of about 27 % is closer to the actual measured value of 17.8 % [43]. The overall behaviour of the 5-20 nm and the 11-62 nm grating is the same for both simulations, whereas the curve profile of the 1-5 nm grating of REFLEC differs from that of GSolver especially in the regime below 10 nm. The curve profile of the 1-5 nm grating simulated with REFLEC fits good to the measured profile when the values are normalized by a factor of 0.25. In conclusion, the deviation of the simulated values to the measured values are smaller with REFLEC than with GSolver. Furthermore a comparison with the actual measurements reveals that the relative behaviour of the calculated efficiency curves from REFLEC are accurate. Thus, the REFLEC simulations can be used to describe the reflectivity efficiency of the three spectrometer gratings after normalization to the measurements. The deviation to lower efficiencies can be explained by the fact that errors and dirt on the gratings decrease their actual efficiency.

The simulation of the 5-20 nm grating is normalized to the measurement (see reference [43]) by a factor of $0.64^{+0.15}_{-0.12}$ with respect to an entrance angle error of $\pm 0.2°$ and the fact that p-polarised radiation was used. Because the simulations for the 11-62 nm grating are similar to the latter ones, the same normalization factor is used for this grating. For the 1-5 nm grating the variation between simulation and measured efficiency is larger with an normalization factor of $0.39^{+0.17}_{-0.10}$. The resulting efficiency curves for all three gratings are shown in the figures 15 to 17.

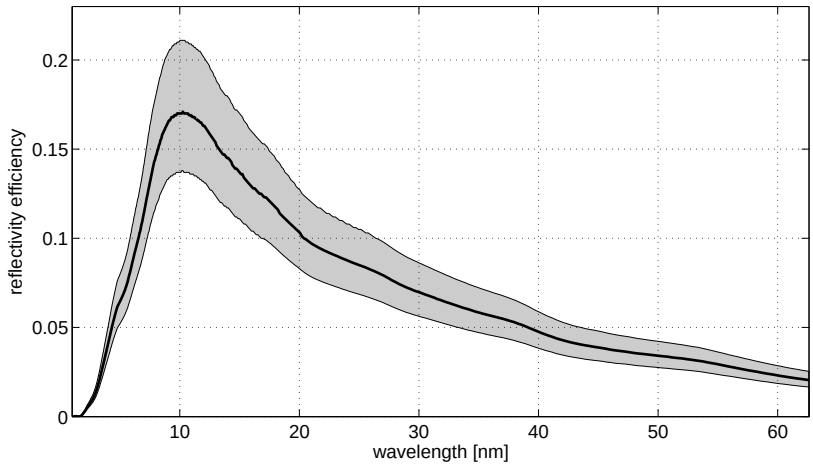

Figure 15: The 5 - 20 nm grating reflectivity efficiency for non polarised radiation at the recommended entrance angle of $\alpha = 87°$ (solid black line). The errors (shaded grey) are due to the deviation between the measurements and the simulations as well as an entrance angle error of $\pm 0.2°$.

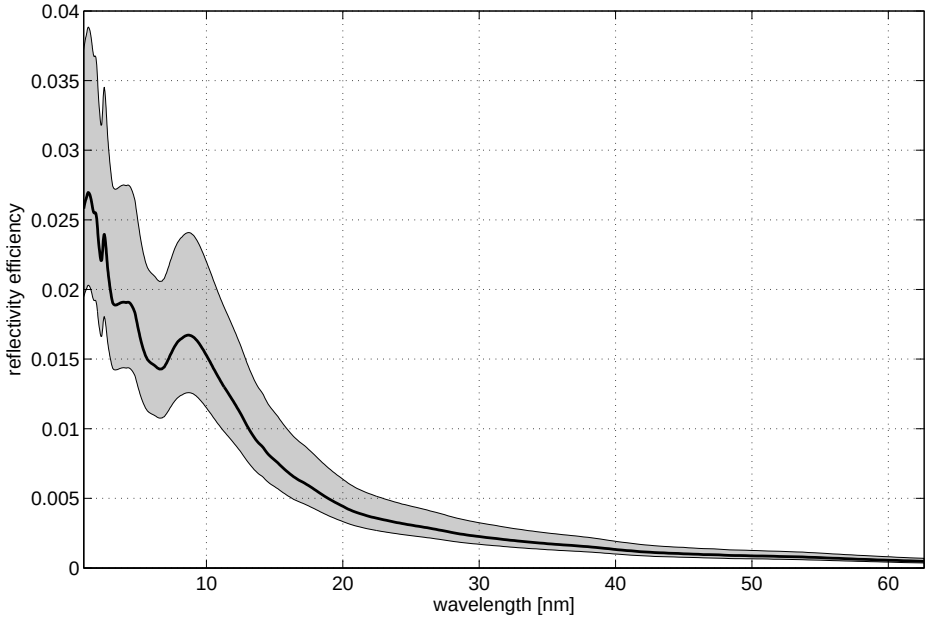

Figure 16: The 1 - 5 nm grating reflectivity efficiency for non polarised radiation at the recommended entrance angle of $\alpha = 88.7°$ (black solid) with errors (shaded grey).

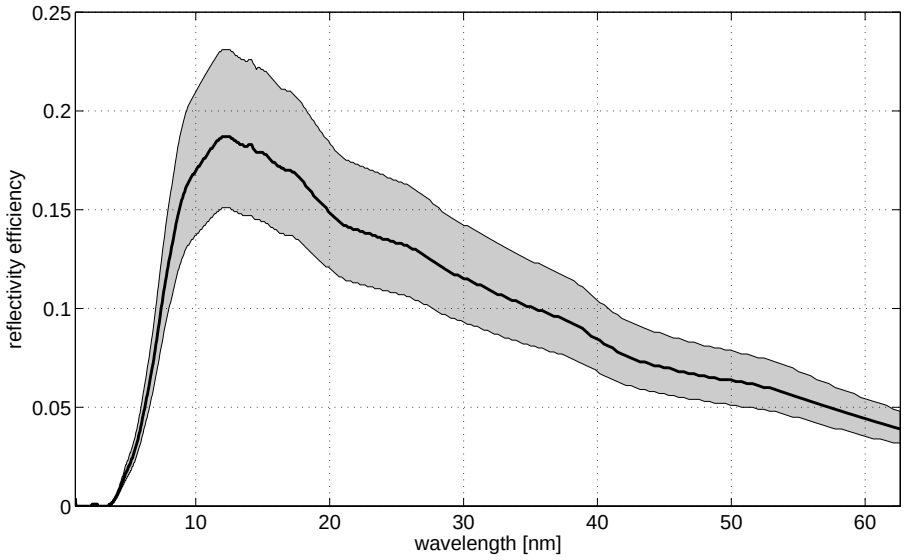

Figure 17: The 11 - 62 nm grating reflectivity efficiency for non polarised radiation at the recommended entrance angle of $\alpha = 85.3°$ (black solid) with errors (shaded grey).

As described in the HHG section, harmonics are produced by linear polarised light. P-polarised means that the electric field vector is parallel to the plane defined by the k-vector of the radiation and the grating normal. In this case the magnetic field is transversal to the plane. Therefore the radiation can also be called transversal magnetic (TM) polarised light. In the simulations shown in figure 12 and 14, the efficiencies where calculated for non polarised light, which means 50% of each polarization are present. The reflectivity is dependent on the polarisation and because the harmonics will be produced with either s- or p- polarisation, this additional factor needs to be consider for the efficiency. P-polarised light will be diffracted deeper into the media, which is in this case the gold coating of the grating. This means that the reflectivity efficiency will be smaller than for s-polarised light, shown in figure 18, where the ratio is shown for the three gratings. The efficiency ratio of s- to p-polarized light increases similar with the wavelength for all three gratings.

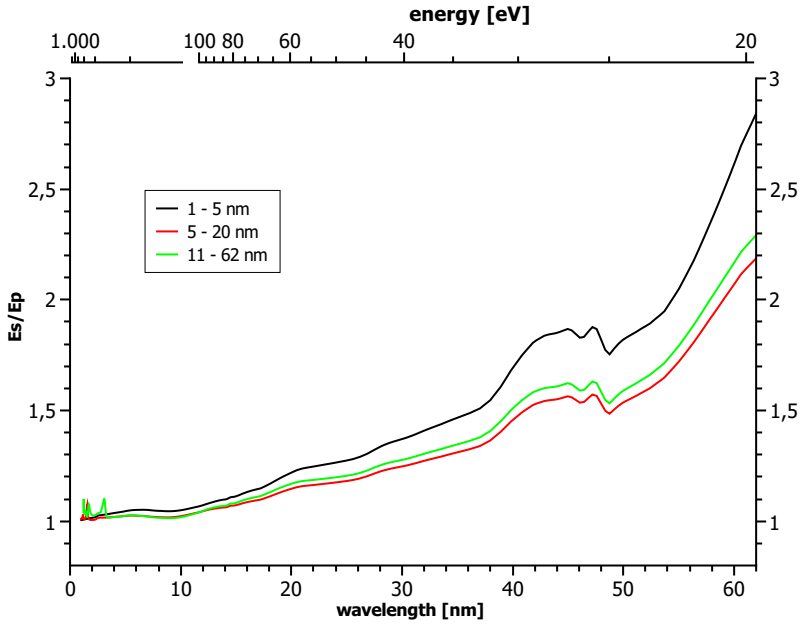

Figure 18: Ratio of the reflectivity efficiency of s- to p-polarised radiation for the 1-5 nm grating (black), the 5-20 nm grating (green) and the 11-62 nm grating (red).

The efficiency of the grating reflectivity is strongly dependent on the incident angle α (see figure 19). The maximum efficiency of the 5-20 nm grating can be reached with an angle of about 83°. With decreasing angle, the maximum reflectivity is shifted towards longer wavelengths. In addition, the reflectivity for wavelengths shorter than the wavelength of the maximal reflectivity decreases. This effect is prominent at an incident angle of 80°, where the reflectivity is only about 1 % at 8 nm.

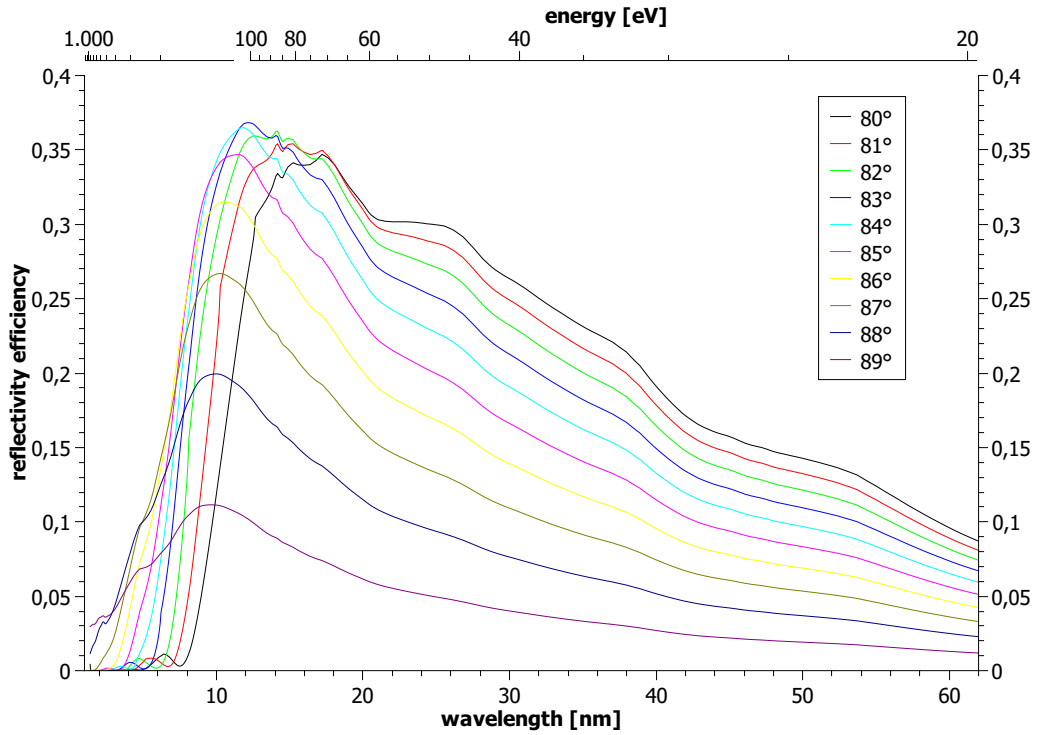

Figure 19: Variation of the entrance angle α from 80° to 89° for the 5 - 20 nm grating.

2.5 Determination of the spectral resolution

The resolution of a spectrometer is a measure for the smallest wavelength difference that can be resolved. In order to calculate the specific resolution for the gratings, first the grating dispersion has to be determined. The grating dispersion is the distance between two wavelengths in the spectral plane. With equation (9) the wavelength dependent angle of reflection β can be calculated. The distance between the two wavelengths of interest is then calculated from β with respect to the distance r' between the grating and the spectral plane. The results for all three gratings are shown in figure 20, where the dispersion is plotted in $[\frac{mm}{nm}]$ on the left y-axis and in $[\frac{pixel}{nm}]$ on the right y-axis. As the dispersion increases towards longer wavelengths, the distance between two wavelengths of the same spectral distance will decrease. Comparing the dispersion of the gratings with each other it becomes obvious that the best resolution will be achieved with the grating that has the highest dispersion at the considered wavelength. In this case, the 11-62 nm grating has the best spectral resolution.

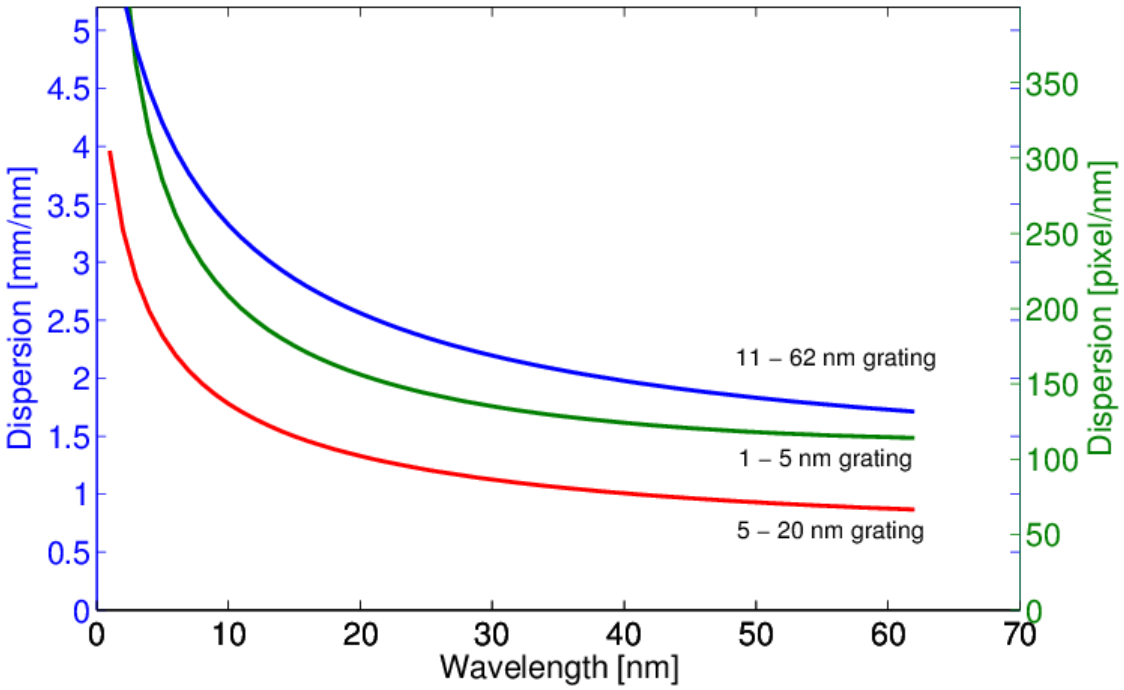

Figure 20: Calculated dispersion versus wavelength for the 1-5 nm grating (green line), the 5-20 nm grating (red line) and the 11-62 nm (blue line). The left y-axis is labelled with the dispersion in mm and the right y-axis is labelled with the dispersion in pixel.

The resolution could either be limited by the grating and the beam width itself or by the pixel size, which is for the PIXIS-XO 13μm. If the resolution is limited by the pixel size of the CCD, it is called hardware limited resolution. The hardware limited resolution can be calculated by multiplication of the considered wavelength with the dispersion at that wavelength in the dimension of $[\frac{pixel}{nm}]$. The results are plotted in figure 21.

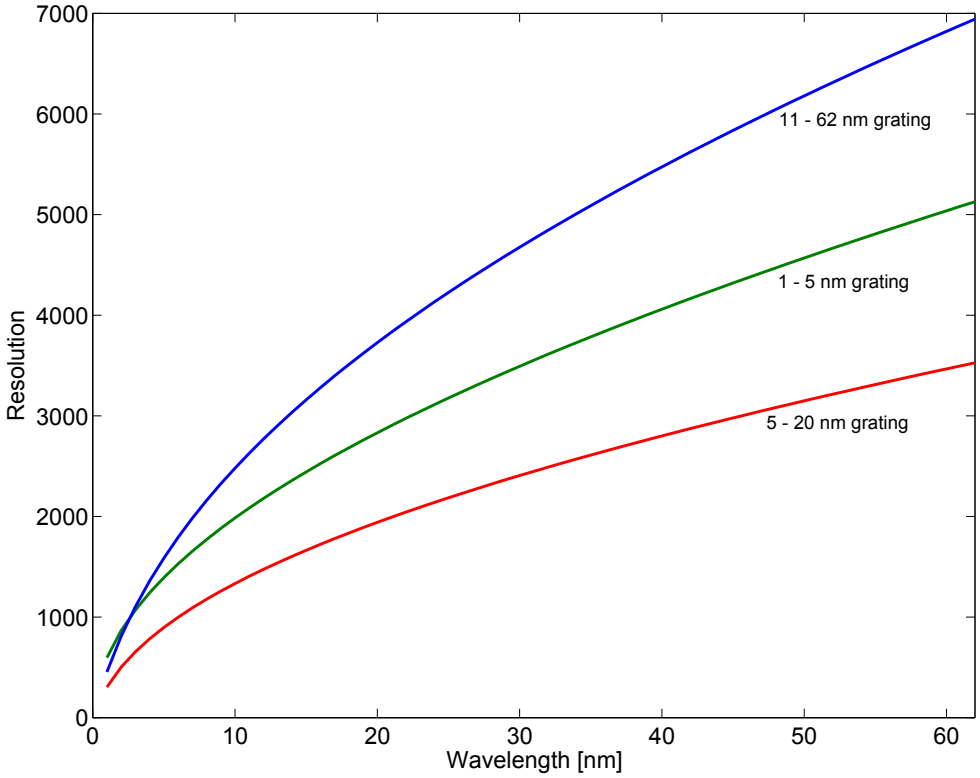

Figure 21: Calculated hardware limited resolution for the 1-5 nm grating (green), the 5-20 nm grating (blue) and the 11-62 nm grating (red)

In order to determine if the resolution is hardware limited, the resolution limit due to the grating and the beam width has to be calculated. A typical beam diameter at the grating is about 4 mm. Multiplication of the beam diameter of 4 mm with the number of grooves per millimetre (e.g. 1200) results in the number of illuminated grooves. A resolution limit of 4800 for the first order diffraction of the 5-20 nm and the 11-62 nm grating is obtained by using equation (8), whereas the resolution limit of the 1-5 nm grating is twice this value, because of a groove density of 2400 grooves/mm. Comparing these values with the hardware limited resolution plotted in figure 21 shows that the resolution is limited by the pixel size for the 1-5 nm and the 5-20 nm grating. For the 11-62 nm grating the resolution is limited by the pixel size for the spectral range below 32 nm. For wavelengths longer than 32 nm the resolution is limited by the beam width and the grating constant. For smaller beam diameters the resolution limit will be shifted to smaller values.

2.6 Position and shape of the focal planes

In the case of an ideal grating with a perfectly aligned spectrometer it can be expected that the recommended spectral range (see table 1) of the gratings is focused on one plane. In order to investigate the shape of these focal planes, the focal position in dependence on the incidence angle α and the distance r between the slit and the grating is examined with a Matlab program provided by T. Dzelzainis. First, the groove density at each position w of the variable line space grating is calculated by:

$$\sigma = \frac{\sigma_0}{1 + \frac{2b_2}{R}w + \frac{3b_3}{R^2}w^2 + \frac{4b_4}{R^2}w^3 + ...} , \tag{25}$$

where b2, b3, and b4 [45] are the parameters for the space variation, R is the radius of curvature and σ_0 is the groove density at $w = 0$. The parameters b2, b3 and b4 of the 1-5 nm Hitachi grating and the 5-20 nm grating are taken from references [46] and [45] respectively. The focal spot of each wavelength is then calculated assuming a bundle of rays. Therefore the standard deviation of the rays is calculated step by step in the propagation direction. When the focal spot is passed, the deviation will again increase, in that case the previous step is repeated with a smaller step size. The resolution is improved until the desired precision is reached.

In figures 22 and 23 the evaluated focal planes of the 1-5 nm grating and 5-20 nm are presented. The focal planes for the required incidence angles α are plotted in figure 22 and the focal planes corresponding to the angles defined by the grating holder (see figure 11) are plotted in figure 23. In both plots the blue lines show the shape of the focal plane for the spectral range from 1 to 62 nm, whereas the other four curves mark the spectral range recommended by the vendor (e.g. 1-5 nm and 5-20 nm).

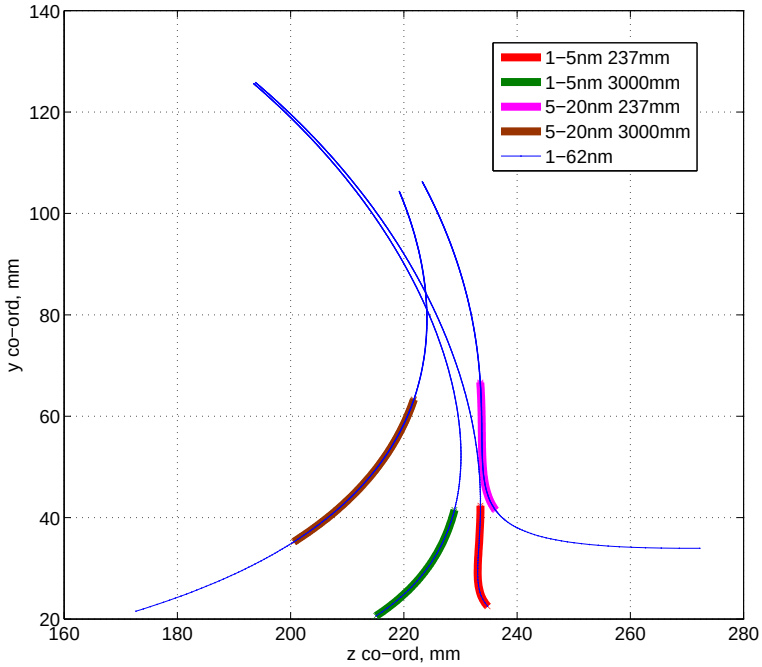

Figure 22: The theoretical focal planes for the 1-5 nm grating with a recommended entrance angle of 87° and a source distance of 237 mm (red) and source distance of 3m (green). The theoretical focal planes for the 5-20 nm grating with a recommended entrance angle of 88.7° and a source distance of 237 mm (pink) and source distance of 3m (brown). The blue lines indicate the focal planes for the spectral range from 1-62 nm, whereas the other lines correspond to recommended spectral range.

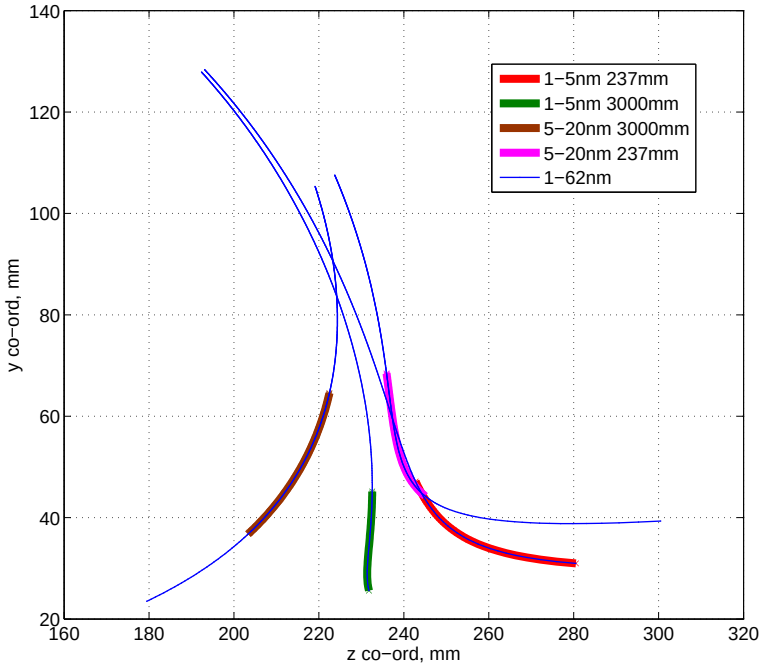

Figure 23: The theoretical focal planes for the 1-5 nm grating with entrance angle of 88.1° and a source distance of 237 mm (red) and source distance of 3m (green). The theoretical focal planes for the 5-20 nm grating with a recommended entrance angle of 86.8° and a source distance of 237 mm (pink) and source distance of 3m (brown). The blue lines indicate the focal planes for the spectral range from 1-62 nm, whereas the other lines correspond to recommended spectral range.

From figure 22 it becomes obvious that the angles α listed in table 1 are reasonable when a slit with a distance of 237 mm to the grating is used. However, when the source point has a distance of 3 m to the grating the image on the CCD chip will not be focused for all wavelengths. In this case the shorter wavelengths are focused at a shorter distance to the grating. For the measurements a grating holder with slightly smaller incidence angles was constructed. The advantage of this grating holder is that the focal plane for a source in a distance of 3 m is better aligned. This becomes obvious in figure 23, where the focal plane of the 1-5 nm grating with an incidence angle of 88.1° is one of the best possible configurations. On the other hand the deployment of a slit in this configuration is not advisable because here the focal length is strongly dependent on the wavelength. The optimal solution for an all-purpose spectrometer would be a motorized grating holder so that the incidence angle can be adjusted for each setup individually.

2.7 Wavelength calibration

Metal filters are necessary to absorb the broadband driving laser so that only the XUV beam is transmitted onto the CCD camera. Without these filters the camera would be saturated and in the worst case it would be damaged by the high intensity radiation. Because the spectrometer has a spectral range from 1-62 nm several different filter materials are required such as aluminium (Al) , zirconium (Zr) and silicium (Si). The filters have a thickness between 200 nm and 500 nm. It is possible to combine different filter materials or to increase the thickness of one material up to $1\,\mu m$, due to two filter wheels in a row where each of it has got six slots. The filter transmission curves are calculated with the Henke tables [23]. In figure 24 the transmission curve of 200 nm aluminium is plotted. The characteristic absorption edge at 17 nm is one possibility to calibrate the spectrometer. The transmission curve of beryllium (Be) shows the same behaviour with a sharp edge at 10.5 nm. Because the wavelength of the harmonic at the aluminium edge can be determined and the central wavelength of the driving laser is known, it is possible to calculate the harmonic order of the considered harmonic. Due to the fact that only odd harmonics are generated, the harmonic order of the other visible harmonics can be determined by counting. Their wavelength is again defined by division of the central wavelength of the driving laser by the harmonic order. For wavelengths shorter than 17 nm, zirconium filters have to be used. Previously the wavelength calibration has to be performed with the aluminium filter, because zirconium does not have such an extreme absorption edge. Another alternative is the usage of an additional silicium filter to calibrate the spectrometer. The transmission efficiency of silicium decreases abruptly at 12.4 nm to shorter wavelengths by about 25% for a filter thickness of only 20 nm. After the calibration the additional filter could be removed and the measurements can be started without considering the complicated absorption curve of silicium. However, the CCD camera has a silicium chip so that the XUV radiation has to penetrate an attenuating layer of silicium or silicium oxide before it reaches the detection area. The thickness of this layer is not qualified by the manufacturer of the camera, but in chapter 3.5, a thickness of about 18 ± 2 nm is extracted from the measurements.

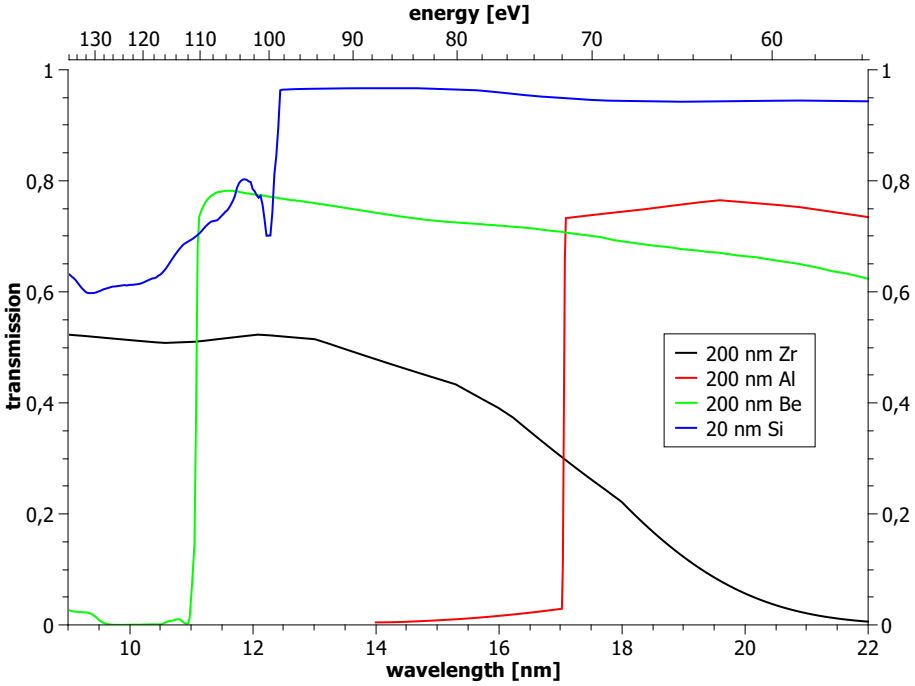

Figure 24: Transmission curves of 200 nm Zr (black), 200 nm Al (red), 200 nm Be (green) and 20 nm Si (blue)

2.8 The XUV CCD camera

A Princeton Instruments PIXIS-XO:1024 B XUV CCD camera is used as a detector for the spectrometer. The silicium chip has a size of 1024x1024 pixels with pixels of 13 µm x 13 µm, which corresponds to a detection area of $(13.3\,mm)^2 = 177\,mm^2$. The PIXIS-XO is equipped with a vacuum flange so that it can be mounted onto a vacuum chamber. The CCD consists of a silicium, a silicium oxide and a silicium nitride layer in front of the poly silicon electrodes. This setup is called a back-illuminated detector (see figure 25). The design of a back-illuminated CCD has the advantage that every incoming photon is detected with a high sensitivity.

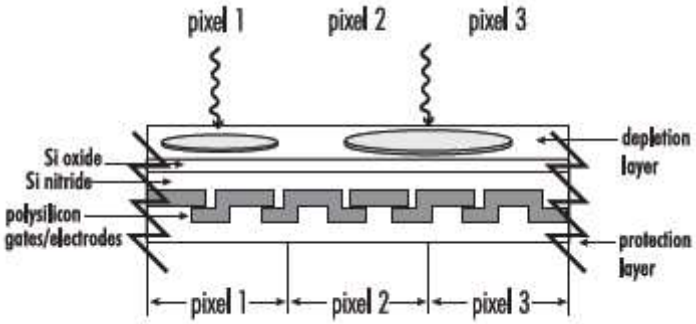

Figure 25: Schematic of the stacked layers of a back illuminated CCD from Princeton Instruments [47]

The sensitivity is further increased by the disclaim of a anti-reflection coating. The quantum efficiency curve provided by Princeton Instruments is shown in figure 26. In the range from 90 to 200 eV the efficiency curve is dotted, which means that the efficiency in this range was not measured and only estimated by Princeton Instruments. The error of this estimation is in the order of ten per cent due to the fact that a silicon oxide layer and perhaps also a part of a pure silicium layer of unknown thickness absorb and scatter the radiation.

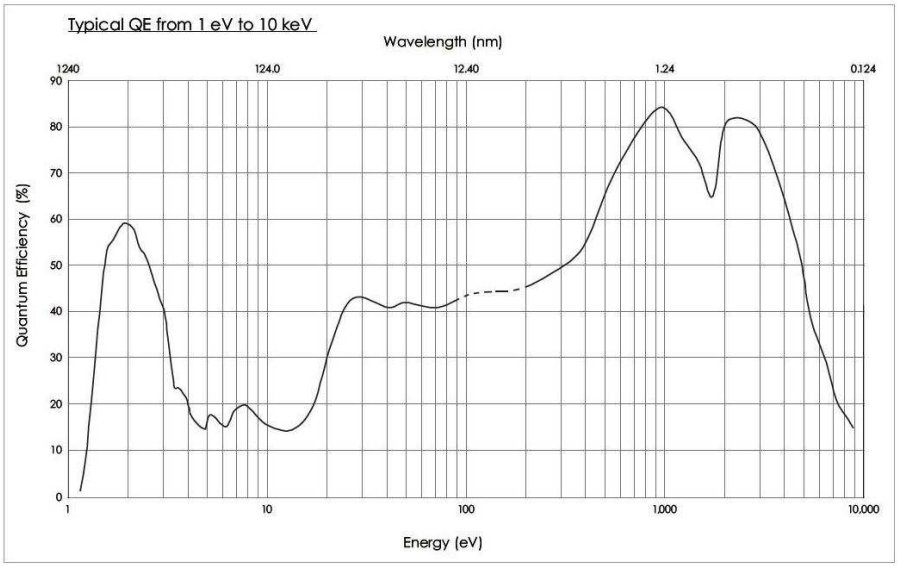

Figure 26: Quantum efficiency provided by Princeton Instruments of the PIXIS-XO:1024 CCD camera. [48]

It is crucial to pay attention to the readout time for experiments where the repetition rate of the incoming signal is faster than the rate the images are read from the CCD. This is due to the readout procedure. Incoming photons generate electrons, which are collected in the potential of the pixels. The

electrons are then shifted from one pixel to next. Since this camera has a 2 dimensional chip the charge of the pixels is transferred into the shift registers row by row. Each row is then read out from the shift registers through one of the two possible output nodes. Thereafter the signals are amplified and the voltages are digitized and transferred to the computer. The shift registers can collect twice the charge of a single pixel. This procedure implies that during the charge transfer from one pixel to another, no light should be exposed further to the camera otherwise the signals add up until saturation is reached.

The readout time of the camera can be controlled by choosing a readout rate, by hardware binning and by defining a Region Of Interest (ROI). The camera could either be run with a readout rate of 2 MHz or 100 kHz. With readout rate and number of pixels, the readout time can be calculated. Thus, for the chip at full resolution, the readout time can be calculated to 524 ms or 10.486 s, respectively. The duration to read out the chip decreases by selecting a Region Of Interest or by hardware binning. If a region of interest is selected the camera only reads out the charge of the selected area. Hence, with a smaller region of interest the readout time decreases. Hardware binning merges several pixel into a single pixel, therefore the number of pixels to be read out is reduced and accordingly the readout time. Note, that hardware binning is limited by the saturation of the shift registers. With the software WinView, which is provided by Princeton Instruments [48], the readout time can be analysed. The measured value for the 2 MHz speed is 581 ms. Thus, the actual readout is delayed by 56 ms compared to the theoretical readout time.

There are two possible solutions if a second light pulse reaches the camera during the readout procedure. If no saturation is reached and the camera is installed in the direction that the readout occurs vertical to the spectrum, an algorithm can be used to normalize the recorded values. However, to remove readout errors a VS 25 shutter with an opening and closing time of 3 ms from UNIBLITZ will be installed in front of the camera. Due to its short reaction time, the camera will be syncronisable to higher repetition rate experiments at full resolution of the chip. Additional to the sharp on and off control, the shutter offers a further protection to the camera from radiation because it is only exposed when a picture is taken.

For measurements at low radiation intensities the adjustment should be chosen such that the signal to noise ratio is large. Therefore the readout rate of the CCD camera can be reduced from 2 MHz to 100 kHz so that the readout noise is reduced from 12.95 electrons to 4.36 electrons per pixel in rms. Another parameter with direct influence on the readout noise is the temperature at which the camera is operated, because the higher the temperature of the chip the larger is the dark charge. Dark charge is the charge measured due to thermal excitation without any light on the chip. The camera temperature can be reduced to -70°C with a Peltier cooler, which in turn is cooled by air cooling.

Furthermore the gain parameter has to be chosen suitable to the measured

intensity. In table 2 the number of necessary electrons to generate one count is listed.

Read out rate	Gain mode	Gain $[\frac{e^-}{count}]$
100 kHz	1	4.29
100 kHz	2	2.18
100 kHz	3	1.05
2 MHz	1	4.46
2 MHz	2	2.30
2 MHz	3	1.19

Table 2: Conversion Gain of the CCD camera

2.9 Energy calibration

In order to be able to calibrate the spectrometer to absolute energy values a gauged XUV diode is installed. The diode, an AXUV100G from International Radiation Detectors (IRD), INC., is a photodiode for the spectral range from 0.0124 nm to 1100 nm. An incident energy of 3.65 eV is needed to create an electron-hole pair in the diode, because it is composed of silicon. The sensitive area of the diode is $100\,mm^2$. The standard thickness of this kind of diode is $55 \pm 1.5\mu m$. The n-doped top layer is protected by a 4 to 8 nm thick silicon dioxide layer. The quantum efficiency of the diode is dependent on the thickness of this oxide layer and the percentage of radiation which is absorbed by the diode. The absorption is 100 % up to a photon energy of 4 keV, photons with an even higher energy have the chance of transmitting through the diode. In the spectral range from 8 to 100 eV, which is about 153 nm to 12 nm, the quantum efficiency drops, because of reflection and absorption of the radiation in the oxide layer. The manufacturer provides the quantum efficiency curves for the XUV photodiodes, which is plotted in two different scales in the figures 27 a) and b). Figure 27 a) shows the quantum efficiency over the whole spectral range in logarithmic y-scale, whereas figure 27 b) shows only the important spectral range from 6 to 62nm, but therefore with a better resolved linear scaled y-axis. The responsitivity of the diode can be simply calculated by dividing the stated quantum efficiency by its corresponding photon energy.

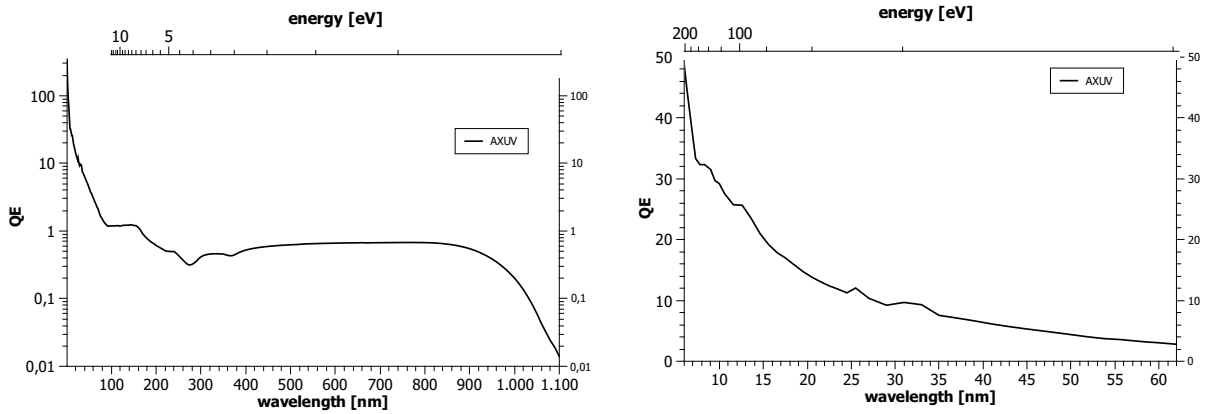

(a) QE from 1 to 1100 nm in logarithmic scale.

(b) QE from 6 to 62 nm in linear scale.

Figure 27: Typical quantum efficiency of an AXUV photodiode [49].

The diode is installed behind the filters and it can be moved in and out of the beam with a linear stage (LSM-38-100, Vacom). This linear translator can be moved by 100 mm and is mounted onto a CF40 flange. In order to prevent short circuit faults the diode itself is mounted on a ceramic holder. The ceramic holder is connected to the linear translator. The electrical contacts at the back of the diode are connected to two wires, which are fed through the flange by a 4 pin LEMO connector.

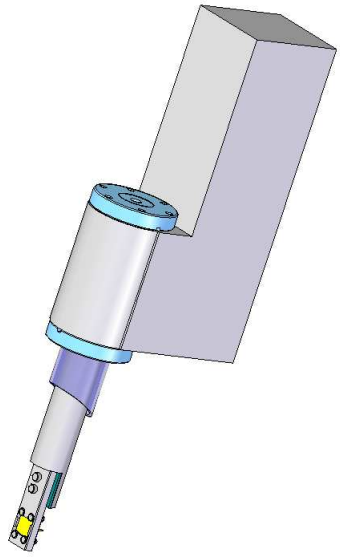

Figure 28: Schematic of the diode mounting and the linear translator. The diode (yellow) is connected by two wires and fed through the vacuum flange (light blue).

When the measured signals are very small a pulse amplifier (PA100) should be used. Otherwise the attenuation caused by the cables will create errors. Typically the amplifier is operated with a power supply of $\pm$ 12 V. Due to this supply voltage the charge detection is limited to 10 fC. The selectable gains are 1, 5, 10, 50, 100, 500, 1000 and 5000.

With such a diode, the spectrometer can be calibrated for measuring absolute intensities. This can be done by limiting the XUV spectrum to a small spectral range with two different filter materials. For the calibration, first the energy of the few harmonics within this spectral range is measured with the diode. Afterwards the diode is removed so that the XUV beam passes onto the grating and on the CCD camera. In order to calculate the total count number per wavelength it is necessary to sum up the measured energy of each harmonic. If only one harmonic is observed, the measured count number of the CCD can be easily correlated to the energy measured by the diode. For a bigger spectral range it is crucial to know the reflectivity efficiency curve of the grating and the quantum efficiency curve of the CCD. With these parameters the total intensity measured by the diode can be correlated to the number of counts of the harmonics.

The limitation of the spectral range for the energy calibration can be carried out with several different filter combinations (see figure 29). The combination of aluminium filters with zircon filters transmits wavelength from 17.06 nm up to around 20 nm dependent on the thickness of the filters. Dependent on the thickness of the zircon filter, there is another region around 50 nm for which the transmission has to be taken into account. This complicates the procedure because for filters with a thickness of less than 400 nm both spectral regions have to be scanned with the CCD. Furthermore the correlation of the count number with the energy measured by the diode is more complicated as the countnumber of several harmonics have to be summed up with respect to the grating reflectivity efficiency. Another possible combination would be a 600 nm Si filter with a zircon filter or a combination of beryllium and niobium. Note, that beryllium is very toxic so that special precautions make a usage difficult. A fourth possibility is to take a single platinum, silver, gold or palladium filter. The transmission curves of those four materials are quite similar as they all show a transmitting window for wavelengths shorter than 14 nm.

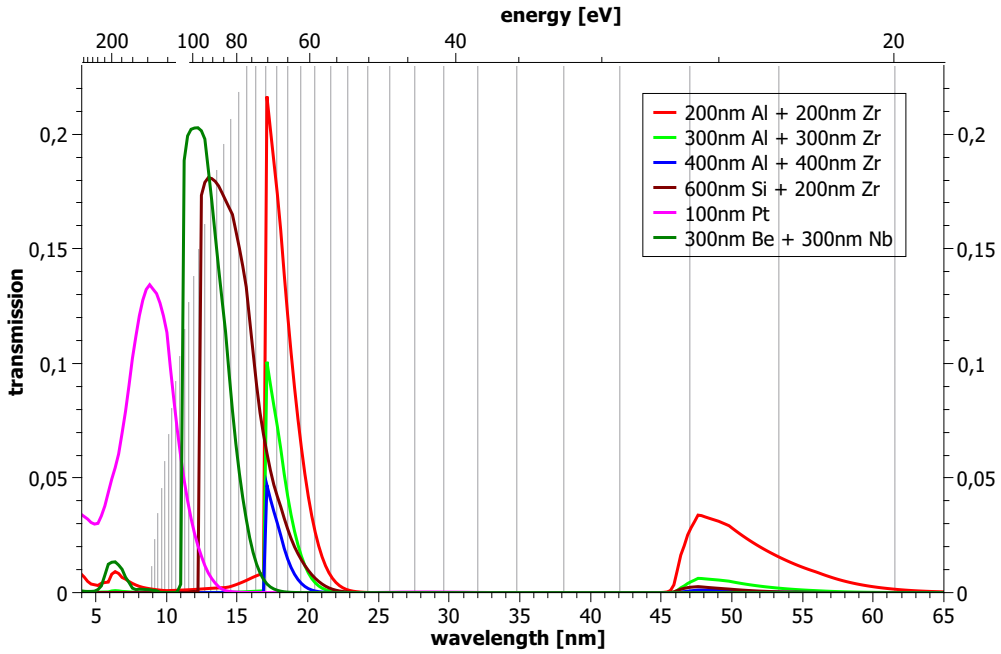

Figure 29: Transmission of different filter combinations in dependence on the wavelength with a simplified intensity profile of the harmonics illustrated in grey lines [23].

In order to avoid errors due to oxide layers on the filters or a deviation of the actual filter thickness, the transmission curves of the filters can be recorded with the calibrated spectrometer. Therefore the transmission curves of two filters of the same material are recorded separately and combined.

2.10 Divergence measurements

For seeding, the intensity of the seed radiation at the entrance of the undulator should be as high as possible. Furthermore, the overlap of the seed radiation with the electron beam in transverse and longitudinal phase space needs to be ensured. Thus, in order to find an optical system, which matches the seed radiation with the electron beam it is necessary to determine the divergence of the XUV beam. For seeding it is best when the overlap is achieved over a large distance therefore the divergence of the seed radiation should be minimized.

One opportunity to measure the beam size is a slit in front of the gratings, which is then imaged onto the CCD camera. By moving the slit into the beam the transmitted intensity is reduced and the intensity profile of the beam for each harmonic can be determined. As a matter of fact it is necessary to know the step size of the slit precisely. The high precision monochromator slit (SLT-100-20 from ADC USA Inc.) is equipped with four stepper motors and 8 end-switches so that each blade can be moved individually. The motors can be

controlled either manually or remotely with a SL-100 Stepper Motor Controller (ADC USA Inc.). Therefore the SL-100 Stepper Motor Controller can be linked to a PC with a RS-232 connection and controlled with an IMS-Terminal. With this configuration one step corresponds to $1.56 \cdot 10^{-2}\,mm$. Furthermore the slit can be also controlled with a Beckhoff controller, where one step corresponds to $31\,nm$. The advantage of this controller is the reliability and the opportunity to control the slit remotely from the network.

A second position where the beam size can be measured is directly on the CCD as the pixel size of the CCD is known. The measurement can be either performed in both dimensions for the direct beam or individually for each harmonic in the vertical dimension. As the divergence is dependent on the wavelength it is advisable to measure the beam size for each harmonic separately.

The divergence can be calculated from both determined beam sizes. Furthermore, the source spot size w_0 of the HHG radiation can be calculated by using equation (7).

2.11 Automation of the HHG setup

The HHG setup includes an absolute pressure controller (MKS PR4000B) which can control two pressures or two flow valves simultaneously. Downstream of these valves, two Parker solenoid valves (pulsed valve no. 9S1-A1-P1-9B06), controlled with two valve drivers (IOTA ONE, Parker Hannifin Corporation), are used as gas pulsers. Attached to the Parker Valves is the QPM dual-gas target. To calibrate the dual-gas target, scans have to be carried out where the gas pressure is varied. This is necessary in order to find the best configuration of both gas pressures to achieve the highest possible conversion efficiency. The pressure scans can be simplified and improved by automation of the HHG setup and the synchronization of this setup to the CCD of the spectrometer. One advantage is the reduction of human manpower to control the complete setup. Furthermore, many scans can be carried out in a shorter time, which offers the opportunity to perform pressure scans with a good pressure resolution. As less time is needed for one complete scan it is possible to decrease long term fluctuations of the pointing and intensity fluctuations of the laser. Another important improvement compared to a manually controlled system is that the gas load in the vacuum chamber can be reduced to a minimum. The synchronization software was programmed with LabVIEW.

The user interface has several input and output fields (see figure 30). Parameters such as the start, end and step pressure values of the driver and the passive gas have to be entered in the fields on the top left hand side. Furthermore, the camera settings such as temperature, ADC speed and ADC gain have to be inserted into the fields on the top right side. In between those fields as a feedback from the pressure controllers, the actual pressure is printed

and the actual picture number is counted. Before starting a scan a background picture can be taken so that scattered light can be subtracted from the scanned images. For an online analysis of the scan, a region of interest (ROI) line and square has to be selected. The recorded spectrum is displayed in the small window and the background subtracted spectrum in the big window on the left side of the screen. In addition, the ROI line profile is plotted each time a picture is taken, whereas the mean pixel value of the ROI square versus the picture number is plotted after the whole scan is finished. This provides an overview of the acquired intensities with respect to the given gas pressures. However, the final analysis of the measurements has to be carried out with an other program.

The program routine starts by setting the hydrogen and HHG gas pressure with the MKS PR4000B pressure controller. After some time delay the gas pressure has reached its appointed value and the program sends a TTL-signal via a National Instruments USB-6009 Interface to the valve driver. The valve driver is switched parallel to the second valve driver so that both valves open simultaneously. A standard configuration requires the following parameters: for an exposure time of the CCD of 1s, the valves have to be opened for about 1.7 s, due to the additional readout time of 581 ms. Therefore the valves are opened first, and after a time delay of 100 ms, the CCD readout is started. Hence, during the whole exposure and readout of the CCD, harmonics are generated in the dual-gas target. The valve will close about 119 ms after the picture is completely read out from the camera. The software will then convert the picture from a 32-bit format into a 16-bit format and subtract the background as well as performing the online analysis. Each original picture will be saved to give the opportunity to start an analysis from the raw data. The intensities of the background subtracted picture will be saved in a text file so that no further preparation of the data has to be done before the analysis. At the end of a scan a text file is saved in which the shot numbers with their corresponding pressure values and mean intensities are printed. This file is useful for the post-analysis of the measurements.

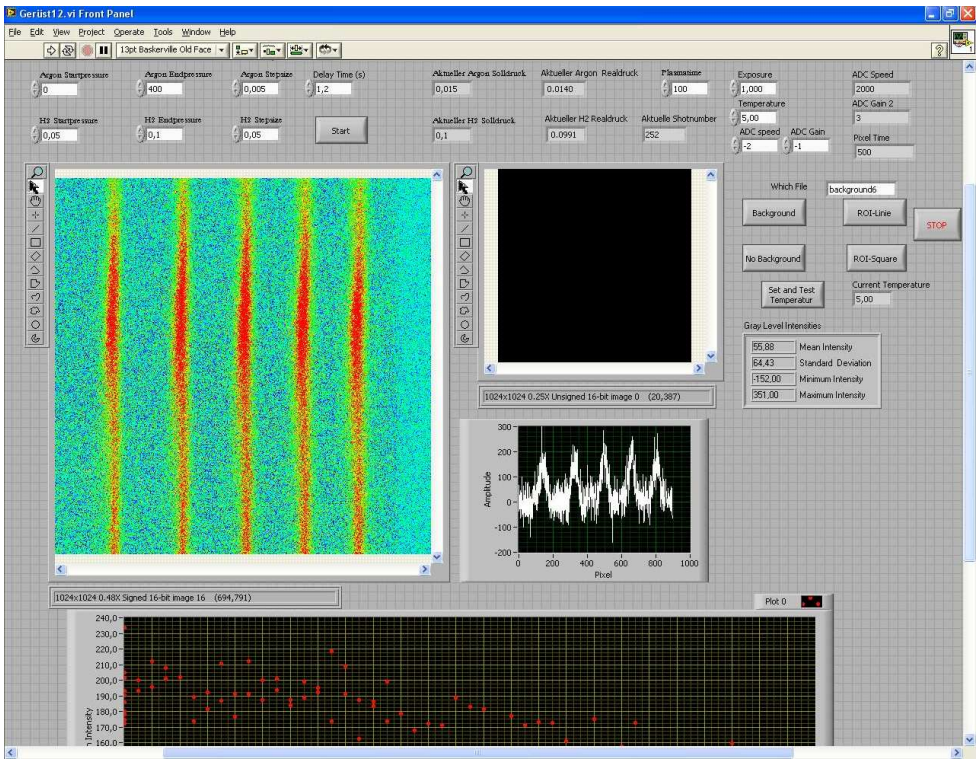

Figure 30: User interface of the synchronised automation software. On the left hand side an harmonic spectrum can be seen. The corresponding line out is plotted in the middle of the screen and next to that the mean and maximum intensity of one of the harmonics.

In order to synchronize the HHG setup with other spectrometers or CCD cameras, the basics of this program are concentrated in a smaller VI. This software controls only the pressure and times the measurements, which means that the CCD has to be read out with another PC and no online analysis is performed. The opening of the valves is again triggered by a TTL signal and this signal is also used to trigger the CCD camera.

2.12 Remote control of the spectrometer with DOOCS & Matlab

The spectrometer will be installed in the tunnel of FLASH2 so it is necessary to be able to control it remotely. DOOCS is the abbreviation for Distributed Object-Oriented Control System, which was developed to control HERA, TTF ("Tesla Test Facility") and FLASH [50]. Thus, it is self-evident that the spectrometer should be also controllable over this user interface. In order to control the CCD camera and to read out the chip as well as sending the pictures to the user interface, a separate server had to be set up. The DOOCS user interface

of the camera is shown in figure 31. The maximal read out rate is 0.52 Hz without any binning or region of interest. As FLASH has a clock of 10 Hz the direct synchronisation of the camera to the FLASH clock is not possible. The problem can be solved with an external shutter so that only every twentieth XUV pulse can pass to the camera. The advantage is that the energy per pulse can be measured directly without any mistakes due to the readout.

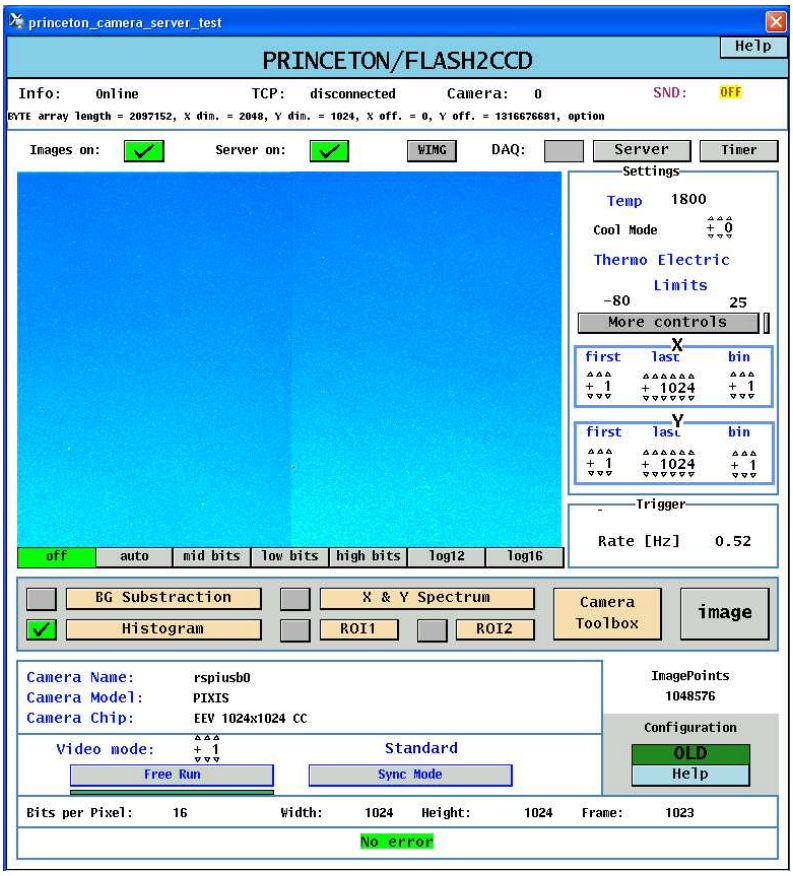

Figure 31: DOOCS interface of the PIXIS-XO:1024 B XUV CCD camera.

The spectrometer consists of three stepper motors (Phytron Elektronik GmbH) for the movement of the camera and the alignment of the different gratings. It further consists of two motorized filter wheels, a linear stage for the grating holder and a slit with four motors for its four blades. In order to simplify the remote control of the spectrometer a Graphical User Interface (GUI) was setup with Matlab (see figure 32).

In the user interface the start, end and step values for a spectral scan can be entered. The position of all stepper motors can be read out by a single button and furthermore directly controlled from the interface. And similar to the automation software, described in chapter 2.11, the camera parameters, indicated on the right hand side, are controllable. The user has three different options

to perform a scan. The most trivial option is to take a single picture by moving the spectrometer to any random position and pressing the "Take Picture" button. Another option is the "Start Scan" button. By pushing this button the spectrometer will move to the required positions and grating to achieve the spectrum, which is indicated by the start value. After the first spectral picture was recorded, the spectrometer will move to the next position and grating to take another picture. When the end value is reached, the procedure stops and the recorded spectral pictures will be connected and plotted in the window at the bottom of the screen. Above this complete spectrum, the summed intensity of each pixel column is plotted in another window with the same x-axis. The third option is to limit the spectral range to one grating so that the scans can be performed in a shorter time. Hence, the additional time to switch from one grating to another can be neglected. In order to subtract the background, a background scan with the same parameters has to be performed in advance. Therefore the "Take Background" button has to be pushed and furthermore the type of scan has to be selected. Afterwards the normal scan can be started and the background can be subtracted. In addition to the simplified control of the spectrometer, the Matlab program has the advantage that measurements can be analysed directly, and the format in which the results are saved can be chosen reasonably.

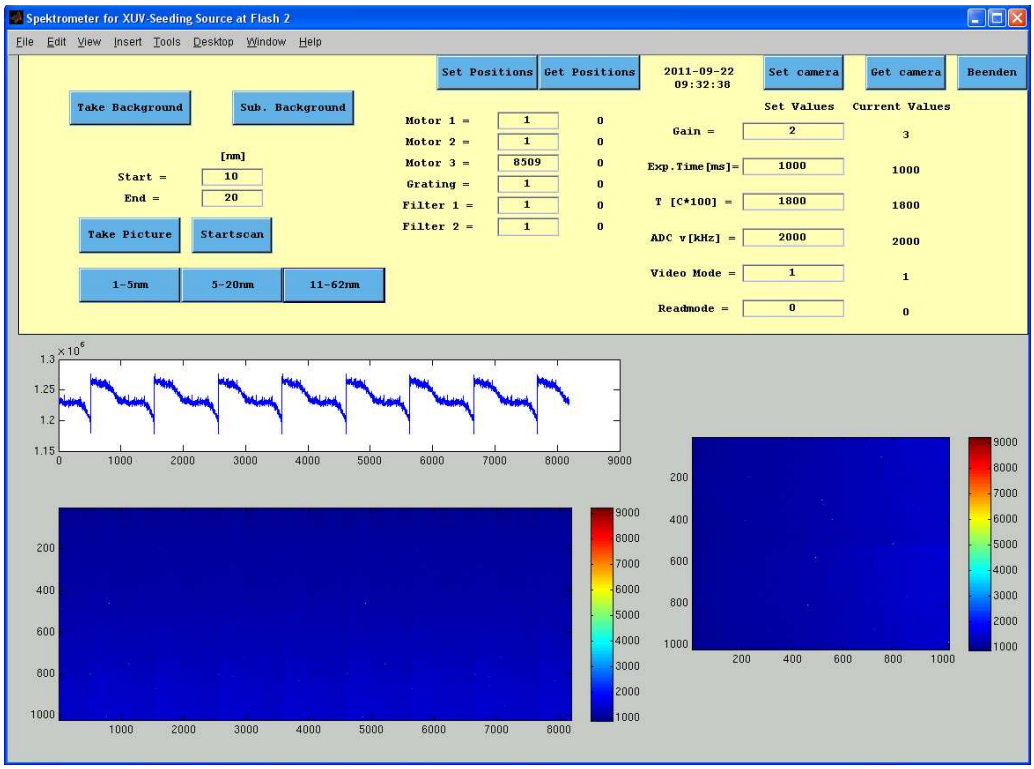

Figure 32: The Matlab graphical user interface for the spectrometer.

3 Measurements and results

The first measurements with the spectrometer were made at the Center for Free Electron Laser Science (CFEL) with a 3 kHz Femtolaser system provided by the "extreme timescales group" [51]. One of the main distinctive features of Femtolaser systems are the carrier envelope phase (CEP) stabilized oscillators. The phase of the single cycles in the envelope of the whole pulse does not vary in time for a CEP stabilized pulse. As the phase of the produced single XUV pulses will be fixed, a broad spectrum is obtained, whereas in the case of no CEP stabilization, destructive interference produces distinct harmonics. A continuum is created by the overlap of the broad harmonics. However, it needs to be ensured that the resolution of the spectrometer is high enough to avoid misinterpretation. Pulses on the attosecond scale would then be transmitted by the usage of a filter which only transmits the spectral range of the continuum.

In order to test the new spectrometer in a real experiment, a HHG setup similar to the one in reference [30] was prepared. In the following chapter, the experiment and the most important results connected to the spectrometer are presented.

3.1 Experimental setup

The laser system delivered laser pulses of either 25 fs or 3.9 fs with energies of 0.9 mJ or 0.43 mJ per pulse, respectively. In order to achieve a pulse duration of 3.9 fs pulses, the amplified laser beam was coupled into a hollow core fibre filled with neon. Due to interaction in the fibre, the spectrum of the pulses were broadened by self-phase modulation and afterwards these broadband pulses are compressed by a chirped mirror compressor. With some losses ($\approx 20\%$) caused by the vacuum window and clipping on the mirrors inside the vacuum chamber the estimated actual energy per pulse was about 0.72 mJ or 0.34 mJ respectively. The laser beam was focused inside the vacuum chamber with a focal length of 750 mm, which resulted in a focal spot size of 60 µm. The in-vacuum mirrors where equipped with "pico-motors" so that the beam could be steered in the near field at the target and in the far-field at the spectrometer. The central wavelength was $\lambda_c = 785$ nm, so that from equations (18) and (19) the cutoff wavelengths of $\lambda_{cutoff} = 6.0\,\text{nm} \pm 0.7\,\text{nm}$ and $\lambda_{cutoff} = 2.1\,\text{nm} \pm 0.3\,\text{nm}$ for neon as HHG medium can be calculated. These values are approximations and follow from the single-atom model. Thus, the actual macroscopic cut off wavelength will be shifted to longer wavelength.

The QPM-target consisted of six HHG gas and seven hydrogen nozzles. In order to compare the conversion efficiency of the QPM target with a non-QPM target, measurements were carried out with a long single jet enclosed by two hydrogen jets and with a nickel-tube. During the experiments, a control volume was installed behind the pressure controller, to ensure a constant gas

flow through the nozzles. The pressure range was limited by the gas supply lines to about 5 bar although the MKS pressure controller was limited to 7 bar [52].

The target pumping setup was exchanged during the experiment. At first the target was installed in a small chamber, which was pumped by an Edwards XDS 35i [53]. The idea was to decrease the amount of gas for the Leybold Turbo-molecular Pumps [54]. The chamber pressure could be decreased with a small entrance and exit hole for the laser beam. However, with diameters of 1 mm in diameter the amount of gas in the path of the laser and XUV beam was far to large. The improved setup included a chimney positioned directly above the gas nozzles. The chimney was pumped through an additional vacuum chamber. Note that the trajectories of the gas molecules in vacuum are straight until they are scattered against each other or at a chamber wall. Thus, most of the molecules were scattered into the chimney, whereas their probability of leaving through the small entrance hole was very small. Compared to a setup without the pumping chimney, the pressure in the main chamber was decreased by at least one order of magnitude.

3.2 Alignment & calibration

3.2.1 Alignment of the spectrometer

The geometrical alignment of the spectrometer was carried out without the CCD camera and with the vacuum chambers open. The spectrometer was moved into a position where the beam spot of the driving laser was centred at the entrance flange. After this the front end of the spectrometer was fixed and the back of the spectrometer was rotated. At the back of the spectrometer an alignment blank sheet was installed. To observe the direct laser beam, it is necessary that the first bellow was compressed completely. The height of the laser beam had to fit with the hight of the two crosses on the blank sheet, which indicate the height of the central point of the CCD camera. For the transverse alignment the back of the spectrometer had to be rotated or the whole spectrometer shifted transverse to the beam direction until the grating holder covered the upper right quadrant of the beam. Afterwards the spectrum can be observed by moving one of the gratings into the beam. The vacuum had a range between 10^{-6} mbar and 10^{-7} mbar.

3.2.2 Alignment of the target and the beam

A coarse alignment of the target was carried out in air by moving the target with three manual manipulators into the beam path. Fine tuning was possible when the chamber was pumped and the plasma from the interaction of the laser with the target gas was observed with a camera. The plasma brightness

was optimized by steering the laser beam and moving the target with the manipulators. The finest tuning was performed with the help of the spectrometer. When the CCD camera was moved directly into the XUV beam, the whole XUV radiation which passes either the aluminium or zircon filter could be seen on the screen. It was necessary to align the driving laser in order to avoid transmission losses or to increase the XUV intensity. Because the filters were visible, when some XUV radiation was transmitted, the beam could be aligned to pass through the filter wheels or some other aperture in the setup without clipping. The whole alignment of the setup was optimized until the maximal harmonic signal was reached. A screen shot of the direct beam taken during the optimization procedure is shown in figure 33. The black spots are damaged pixels of the CCD. Furthermore, weak patterns in the form of circles or bars are visible. The bars result from some unevenness in the filter, whereas the circles are formed by diffraction at some grain of dust on the filter.

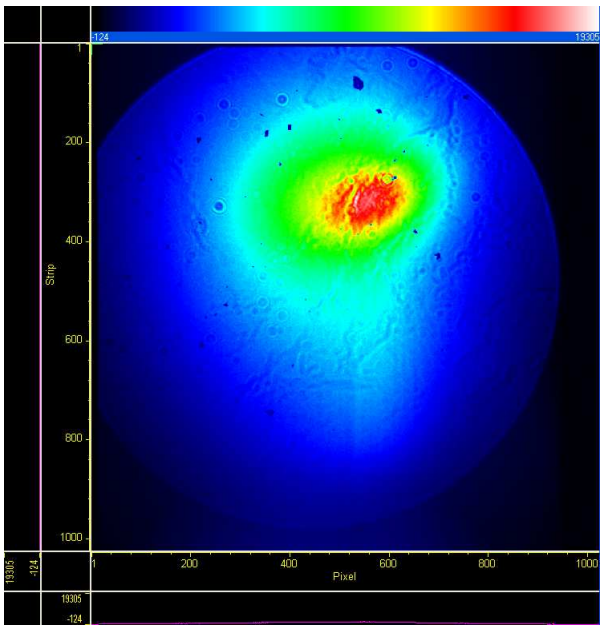

Figure 33: View of the direct XUV beam with a 200 nm aluminium filter, 1 s exposure time and 400 mbar argon. The circular shape of the filter is visible.

3.2.3 Calibration of the spectrometer

After the grating was moved into the beam, the CCD camera position was changed to see the first order diffraction of the grating. The position of the grating was improved by moving it transverse to the beam axis to maximize the intensity of the harmonics. By changing the distance of the CCD to the grating, the sharpness of the harmonics could be optimized.

The spectrometer was calibrated by applying an aluminium filter. The

transmission curve of aluminium (see figure 24) has a hard edge at 17 nm. In figure 34, harmonics from the 39^{th} to 45^{th} order, which correspond to wavelengths of 20 nm and 17.3 nm respectively, as well as the hard edge of the spectrum at 17 nm, can be clearly distinguished. The harmonic order was calculated from the central wavelength of the driving laser. Also visible is the lower blade of the slit, as it blocks partially the incoming beam. After the calibration with the aluminium filter was carried out it was possible to change to other filter materials such as zirconium.

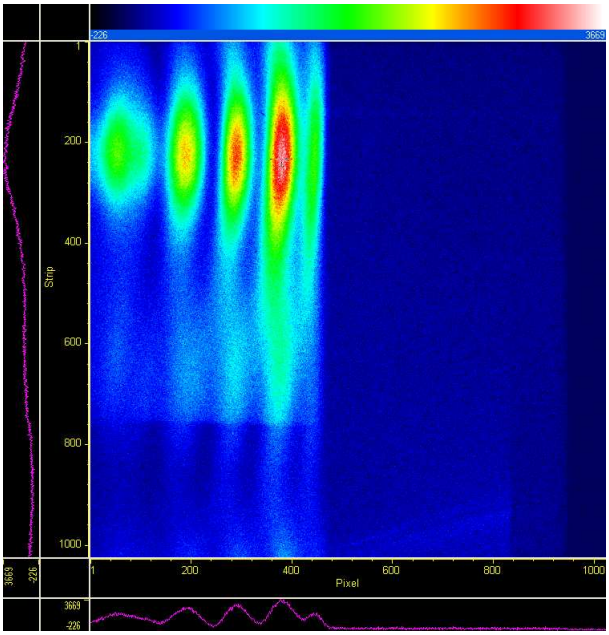

Figure 34: View at the aluminium absorption edge at 17 nm.

3.3 Calculation of the conversion efficiency

It is important for seeding to have enough energy per pulse at the resonance wavelength of the undulator. In order to determine the harmonic energy several factors have to be considered. At first it is necessary to determine the count number per photon in dependence on the wavelength from the CCD:

$$n_{counts\,at\,CCD}(\lambda) = \frac{E\,[eV]}{3.6\,eV} \cdot \eta_{QE}(\lambda) \cdot \eta_{ADC}\ , \tag{26}$$

where E is the energy of the incoming photon, 3.6 eV is the energy, which is needed to create an electron-hole pair in the silicium chip, $\eta_{QE}(\lambda)$ is the quantum efficiency of the CCD and η_{ADC} is the gain factor. Due to the fact that XUV photons are completely absorbed in the chip, photons of the 45. harmonic deposit an energy of 71 eV. With a quantum efficiency of 41 % at this wavelength, it results in eight excited electrons. With a selected ADC gain

factor of 1.19 $\frac{electrons}{counts}$, the number of counts per incoming photon is found to be 6.8. In order to calculate the conversion efficiency, it is necessary to calculate the corresponding number of photons at the source point. Several elements in the spectrometer attenuate the incoming harmonic signal until it is detected by the CCD. The attenuation $\eta_a(\lambda)$ is given by

$$\eta_a(\lambda) = \prod \eta_{GE}(\lambda)\eta_{Slit}(\lambda)\eta_{filter}(\lambda)\eta_{filteroxide}(\lambda)\eta_{CH}(\lambda) \ , \tag{27}$$

where $\eta_{GE}(\lambda)$ is the grating efficiency, $\eta_{Slit}(\lambda)$ is the slit transmission coefficient, $\eta_{filter}(\lambda)$ is the filter transmission coefficient, and, $\eta_{filteroxide}(\lambda)$ and $\eta_{CH}(\lambda)$ are correction factors due to a thin oxide or carbon layer on each side of the filter. The total attenuation for harmonics of the order 39 to 45 is mainly dependent on the grating reflectivity efficiency (see figure 35). By multiplication of $n_{counts\,at\,CCD}(\lambda)$ with $\eta_a(\lambda)$ for the 45. harmonic, a factor of 0.4 $\frac{counts}{source\,photons}$ is obtained. Each measured number of photons has to be divided by this factor and the result is the number of source photons. The conversion efficiency is calculated by comparison of the harmonic energy with the energy of the driving laser. As the measurements were performed with a duration of 1s and a repetition rate of 3 kHz, the energy deposited in the target was about 1 J.

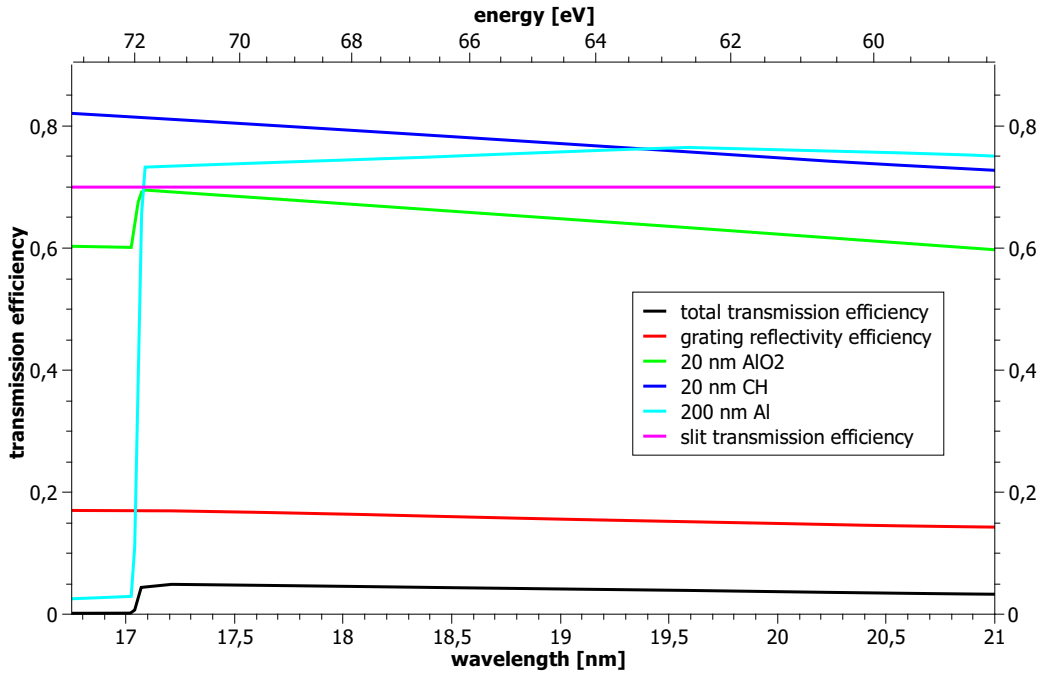

Figure 35: Transmission efficiency of the grating (red), the filters (light blue), the filter oxide layer (green), a carbon layer on the filter (dark blue), the slit (pink) and the resulting total efficiency for harmonics of the order 39 to 45.

3.4 Results for 25 fs pulses

3.4.1 Blue shift

In figure 36, the results of a scan with a neon backing pressure of 1.1 bar and a hydrogen gas pressure from 100 mbar to 800 mbar with a step size of 25 mbar is shown. The wavelength calibration on the y-axis was carried out with equation (9) and the parameters d and α were slightly varied to fit to the calibration of the aluminium edge at 17 nm. The dependence on the hydrogen gas pressure is given by the x-axis; the wavelength dependence is given by the y-axis and the colour indicates the intensity in counts measured by the CCD camera. With increasing hydrogen pressure the harmonics are shifted to shorter wavelengths, known as blue shift. This can be seen for example at the 45 harmonic. With a hydrogen pressure of 100 mbar its centre is situated at about 17.3 nm and with a hydrogen pressure of 700 mbar the centre is at about 17 nm.

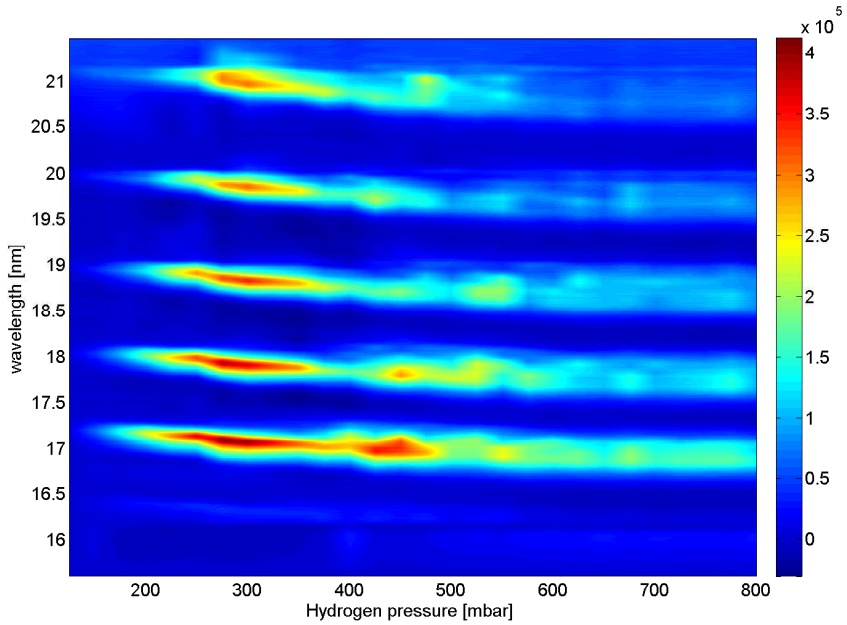

Figure 36: Interpolated hydrogen gas pressure scan. The blue shift increases with increasing hydrogen density.

One explanation could be the interaction of the driving laser with the hydrogen gas, which generates a plasma in the path of the laser beam. The central wavelength of the driving laser is blue shifted, due to the interaction of the laser pulses with the plasma, and therefore also the harmonic signal is shifted to shorter wavelengths. Taking into account the change of the refractive index

with the gas pressure the frequency can be calculated with

$$\omega(y,t) = \omega_0 - 2k_0 \frac{\partial}{\partial t} \int_0^{L(t)} n(x,y,t)dx \ ,$$

where x is the coordinate in beam direction, y is the transvers coordinate and L the interaction length [55, 56]. In order to achieve a blue shift of 0.3 nm for the 45. harmonic with this formula an interaction length of $L = 5\,cm$ is required. Thus, the interaction with the 25 fs laser pulses changed the refractive index n by about $-6.24 \cdot 10^{-5}$, which results in a shifted central wavelength of the driving laser to 765 nm. An interaction length of 5 cm seems far to large as the target has only a length of 1.2 mm. However, these measurements were performed with the setup of an inner chamber, which increased the gas pressure and the interaction length to the order of a few centimetre. Moreover an extended interaction length seems accurate, due to the observation of a long filament in front and behind of the target .

In conclusion, the effect of hydrogen on the harmonic spectrum has been considered when the dual-gas QPM target is used. The analysis of this effect is necessary in order to determine the pressure range up to where the usage of hydrogen does not alter the wavelength of the generated harmonic.

3.4.2 Enhancement due to QPM for 25 fs pulses

In order to determine the enhancement factor due to QPM, experiments with a QPM target and a non-QPM target were carried out.

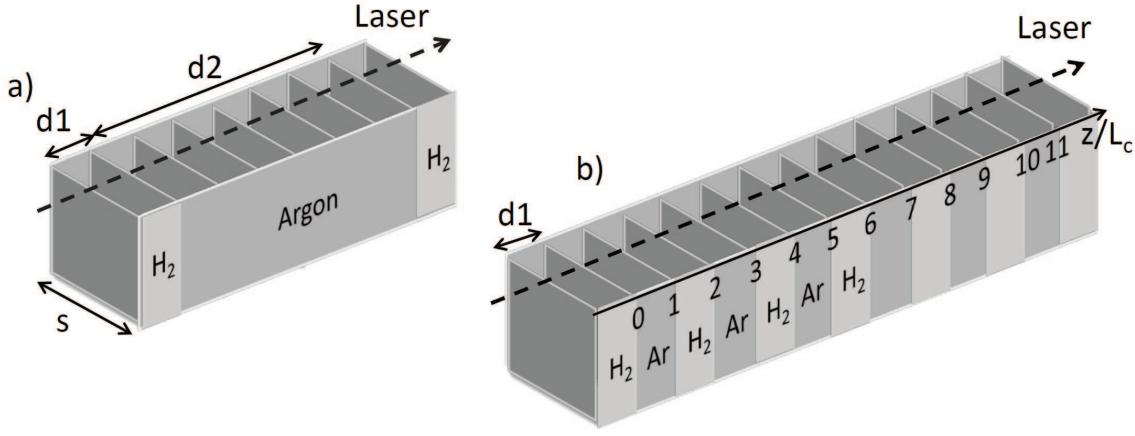

Figure 37: a) Dual-gas target with an array of merged HHG gas nozzles with the length d2. b) Dual-gas target with QPM configuration of the single nozzles with the length d1. (Courtesy of A. Willner)

A direct comparison of the setups is possible, because both target designs delivered the same neon gas density. The non-QPM target consisted of six

single jets merged into one array without any passive zones in between. The resulting HHG gas nozzle had a length of 600 μm and a transverse width of 800 μm. It was limited on each side by one hydrogen gas nozzle of 100 μm length, with a backing pressure of 100 mbar. In figure 37 both target designs are presented; the selected HHG gas there is argon instead of neon.

In figure 38, a neon pressure scan with such a merged array is presented for the 45^{th} harmonic. In this case the gas pressure was tuned up to 2.75 bar. With a central wavelength of 780 nm, the 45^{th} harmonic corresponded to 17.4 nm or 71.1 eV. The maximal achieved energy of this harmonic was 0.12 pJ.

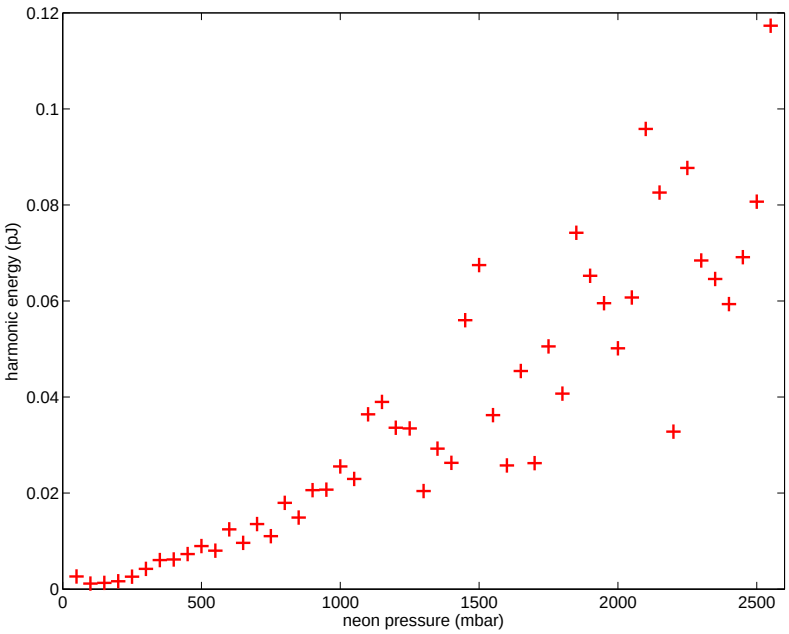

Figure 38: Harmonic energy for the 45 harmonic in dependence on the neon backing pressure.

A direct comparison between the QPM target and the merged jet at different neon pressures is shown in figure 39. The green crosses are the measurements with the merged jet target (see figure 37 a)) in the range from 0 to 2 bar in steps of 25 mbar. The blue crosses are the data points measured with the QPM target. Each of these points was achieved by maximizing the harmonic output by tuning the hydrogen gas pressure. The hydrogen pressure determined the free electron density and correspondingly the phase advance in between the neon nozzles. Note, that the harmonic energy is not only dependent on the phase matching condition but also on volume effects as well as plasma beam deformation. Due to a low harmonic energy at the neon pressure scan, the harmonic signal can be hardly distinguished from background noise. Thus, it is

impossible to determine a quantitative enhancement factor due to quasi-phase matching. However, the harmonic signal of the QPM target using hydrogen is stronger by at least one order of magnitude. The gas flow through the pressure controller was limited to small values, therefore high gas pressures could not be maintained for long opening times of the nozzles. Due to this, the gas density decreased during the opening time and accordingly the errorbars become larger for higher gas pressures. In the following experiments the pressure range could be extend up to 4 bar through the deployment of two gas reservoirs. However, in order to adjust even higher pressure at longer opening times the gas flow through the pressure controllers has to be increased.

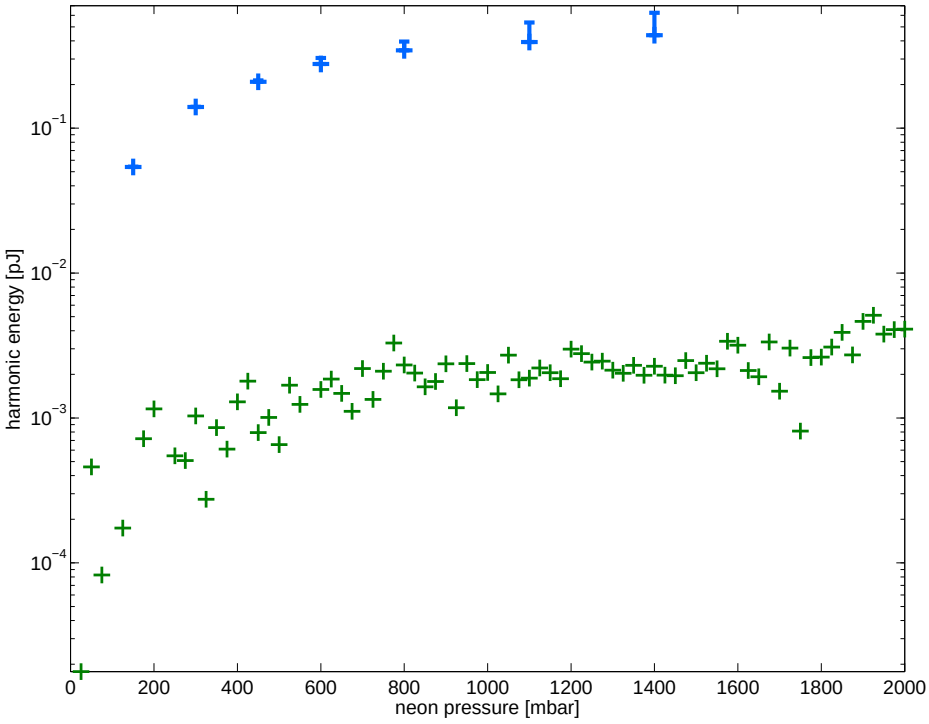

Figure 39: Direct comparison of the QPM target with (blue) and without hydrogen (green) at different Neon pressures.

For the measurements an exposure time of 1 s and an aluminium filter with a thickness of 200 nm were used. The laser power, which was measured in front of the entrance window of the target chamber, was 2.7 W. In order to calculate the pulse energy at the target position, reflection of the beam at the entrance window and clipping on the two focusing mirrors inside the chamber were taken into account with a factor of 0.8. The obtained energy per laser pulse was 0.72 mJ. The harmonic signal was maximal for the 45^{th} harmonic

with a conversion efficiency of $8 \cdot 10^{-10}$. Such a conversion factor is far to small to reach energies, which are high enough to exceed the SASE process (see reference [38]). However, it was the first experiment with the dual-gas foil target to investigate the harmonic spectrum at such short wavelengths (see [30]).

3.5 Results for 3.9 fs pulses

3.5.1 Correction of the CCD readout

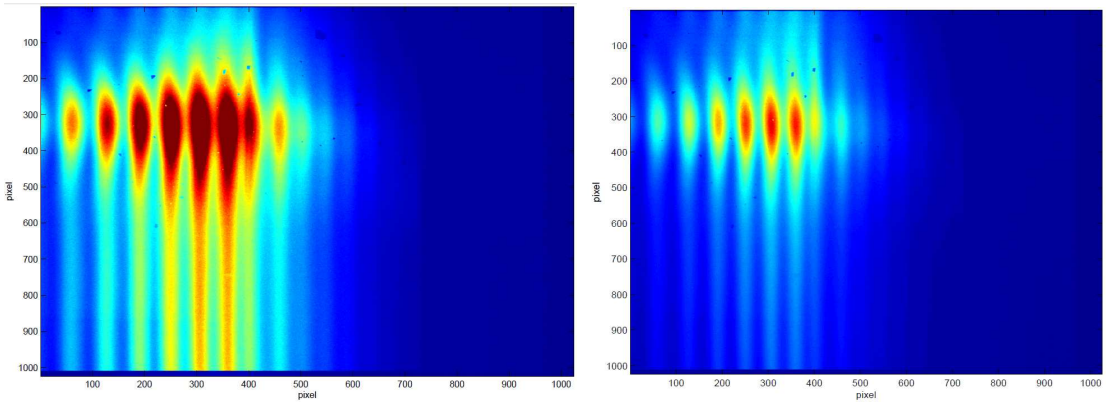

(a) Background subtracted spectrum

(b) Background subtracted spectrum with correction for the readout time

Figure 40: Spectrum with a neon pressure of 3 bar and hydrogen of 5 mbar.

In contrast to the results with the 25 fs laser pulses the achieved XUV intensities with the 3.9 fs laser pulses were higher and the spectral range was extended to shorter wavelengths. A typical obtained spectrum is plotted in figure 40 a). Even though the background is already subtracted the intensity increases from the top to the bottom of the CCD. This is due to the readout of the electric charge from the CCD. The readout has to be considered for the analysis especially for high intensities as the signal could add up until the saturation level of the CCD is reached (see also section 2.8). In order to remove the readout errors, the count values of each row are normalized to the exposure time of the topmost pixel row. The corrected spectrum is shown in figure 40 b). This spectrum is very symmetric, which demonstrates that the procedure works correctly.

3.5.2 Wavelength calibration with the CCD

In figure 41 the integrated energy of each pixel column at a neon pressure of 2500 mbar is presented in dependence on the pixel position (top x-axis). As the

laser pulses where not CEP stabilized, the spectrum shows distinct harmonics. Furthermore the transmission efficiencies of a 18 nm silicium layer, a 18 nm siliciumoxid layer, a 300 nm zirconium filter and neon at a pressure of 10 mbar with an interaction length of 2 mm is plotted against wavelength (bottom x-axis).

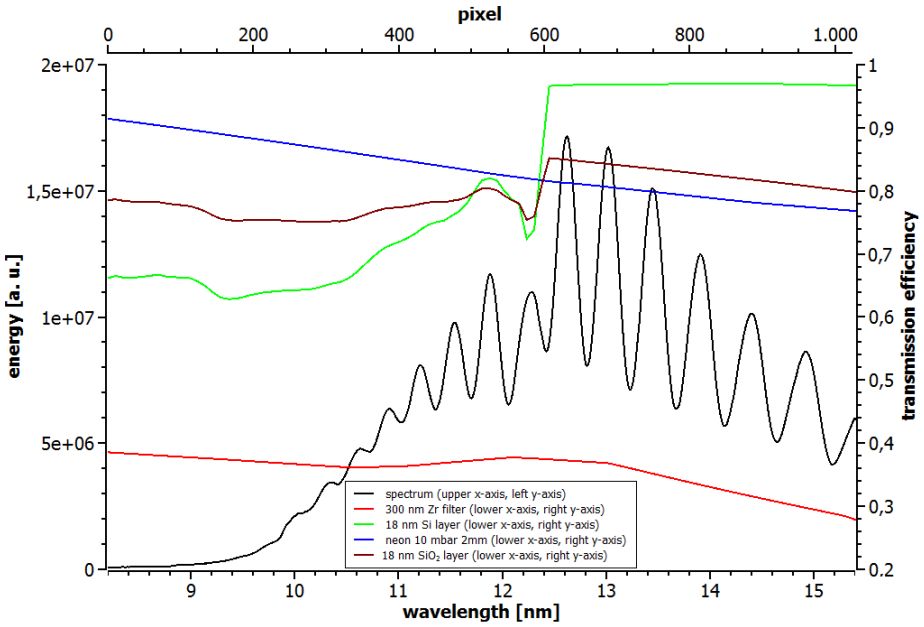

Figure 41: Integrated energy in spatial direction for a neon pressure of 2500 mbar without CEP stabilized laser pulses (black, upper x-axis, left y-axis). The transmission curves (right y-axis) of a 18 nm Si layer (green), a 18 nm SiO_2 layer (brown), a 300 nm Zr filter (red) and neon (blue) at a pressure of 10 mbar with an interaction length of 2 mm is plotted in dependence on the wavelength (lower x-axis)

In this wavelength range, the CCD shows an absorption profile of a silicium layer with a thickness of about 18 nm. The decrease of the transmission efficiency of the silicium layer at 12.2 nm can be correlated to the position at around pixel 600. Therefore the first harmonic that is attenuated by the silicium layer is the 65^{th} harmonic. Hence, it is not necessary to use an additional filter to calibrate the spectrum. The energy decrease at longer wavelengths is due to the decreasing transmission efficiencies of neon and zirconium and to the decrease of the grating reflectivity efficiency. However, it could be also possible that the topmost layer is not purely composed of silicium but also siliciumoxid.

Furthermore from the relative drop of the intensity at 12.2 nm, the thickness of the attenuation layer in front of the CCD can be determined. The thickness of the attenuation layer can be determined to be in the order of 16 to 20 nm. This could be checked with some measurements at a gauged source for example

the DORIS-synchrotron. Nevertheless, for the analysis it is now possible to take this additional absorption into account.

3.5.3 Enhancement due to QPM for 3.9 fs pulses

The effect on the harmonic energy due to phase tuning with hydrogen is shown by comparing QPM and non-QPM scans. In figure 42, the comparison is shown for the 57^{th} harmonic ($\lambda = 13.8\,nm$ or $E = 89.0\,eV$). The red crosses show the neon pressure scan without hydrogen . The blue crosses show the maximal harmonic energy achieved by tuning the hydrogen pressure at a fixed neon pressure.

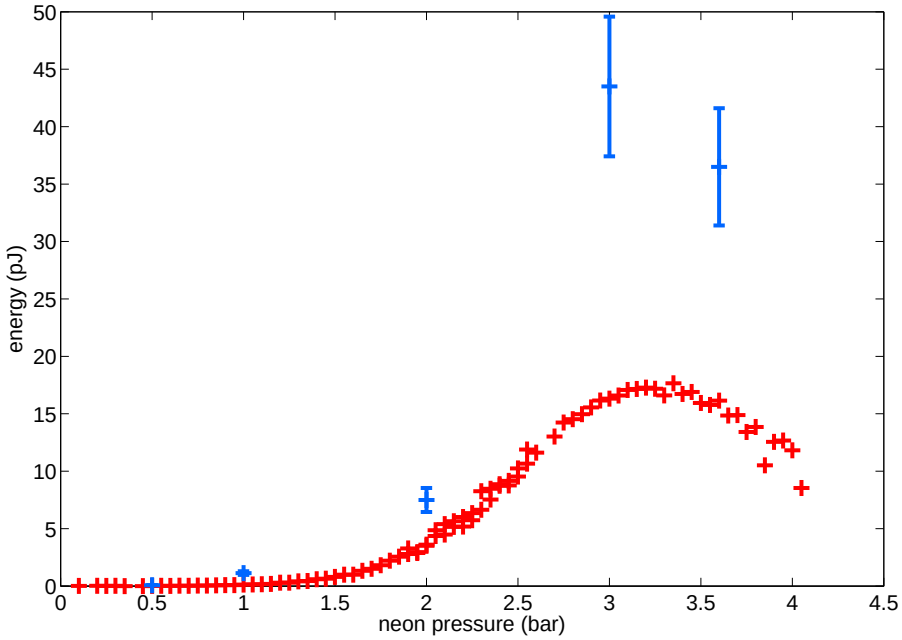

Figure 42: Comparison of the harmonic energy for the 57^{th} harmonic with (blue) and without hydrogen (red) to tune the phase between multiple sources. Only the highest energies obtained via hydrogen scans are plotted.

An enhancement factor larger than two can be observed at neon pressure of 3 bar, whereas the enhancement factor at a neon pressure of 3.6 bar is smaller. For an ideal adjusted QPM source, higher neon pressures would result in higher enhancement factors. The decrease of the enhancement factor is visible for all harmonics, and furthermore, the spectral range is decreased with increasing hydrogen pressure (see figure 43). At low hydrogen pressures the XUV spectrum shows a cutoff at 12 nm with an energy of more than 10^7 counts. In contrast to that, the cutoff is reduced to 13 nm at 700 mbar hydrogen. The

higher the hydrogen pressure the weaker is the harmonic energy in the short wavelength region. This implies that the reduction is a result of the interaction of the driving laser pulses with the hydrogen gas. It could be possible that the pulses are distorted or sustain a spectral chirp from the interaction. And, as the pulse duration is only 3.9 fs the effect of a small energy distortion could lead to a strong decrease of the macroscopic cutoff. This is due to the fact that the harmonic energy E scales with the driving laser intensity I as $E \propto I^{5-7}$ [38].

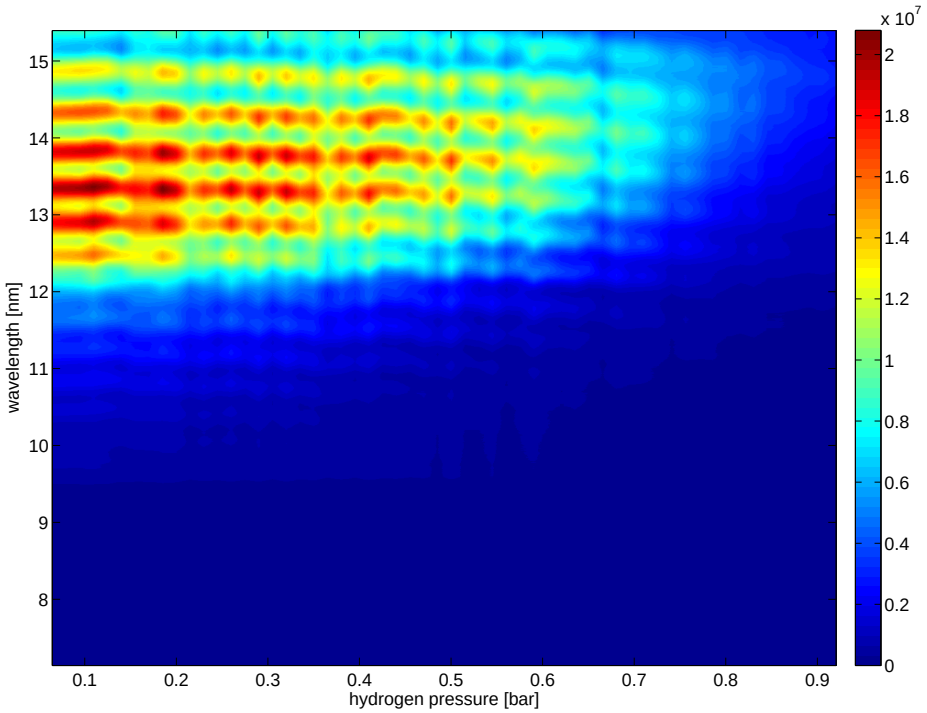

Figure 43: Hydrogen scan for a fixed neon backing pressure of 3.6 bar. The harmonic energy is indicated by colour in arbitrary units.

The conversion efficiency is again calculated with equations (26) and (27) with respect to an additional attenuation from the topmost silicium layer on the CCD. The maximal reached conversions efficiency of the 57^{th} harmonic is $1.3 \cdot 10^{-7}$, which is of the same order of magnitude as the highest conversion efficiencies published recently. For example from reference [57], driver pules with 1 kHz, 800 nm, 35 fs and pulse energies of up to 5 mJ in a free neon jet with a length of 2 mm at 300 mbar resulted in a conversion efficiency of 10^{-7} at an energy of about 80 eV.

3.6 XUV pulse characteristics

An important characteristic of the generated XUV pulses is the line sharpness from which the pulse duration can be estimated. The highest harmonic order observable with the 3.9 fs driving laser pulses was the 79^{th}, which corresponded to a wavelength of 9.9 nm. And the highest order harmonic which could be evaluated was the 67^{th} ($\lambda = 11.7nm$). In order to determine the line sharpness first of all the (FWHM) line width has to be measured. For example the line width of the 45^{th} harmonic is about 29 pixels. Multiplication of the line width with the dispersion of the 11-62 nm grating results in a bandwidth of $\triangle\lambda = 0.140 \pm 0.010$ nm. Dividing the central wavelength of $\lambda = 17.4$ nm by $\triangle\lambda$ determines the line sharpness to be $\frac{\lambda}{\triangle\lambda} = 124.6 \pm 5$. For the experiment with the 3.9 fs driving laser pulse, it was not possible to evaluate all observed harmonics as it was not possible to distinguish the (FWHM) line width of some of the harmonics from the continuous background. The line sharpness for all evaluable harmonics is shown in figure 44. The plotted results are divided into the experiment with the 3.9 fs driving laser pulses measured with the 5-20 nm grating and the experiment with the 25 fs driving laser pulses measured with the 11-62 nm grating.

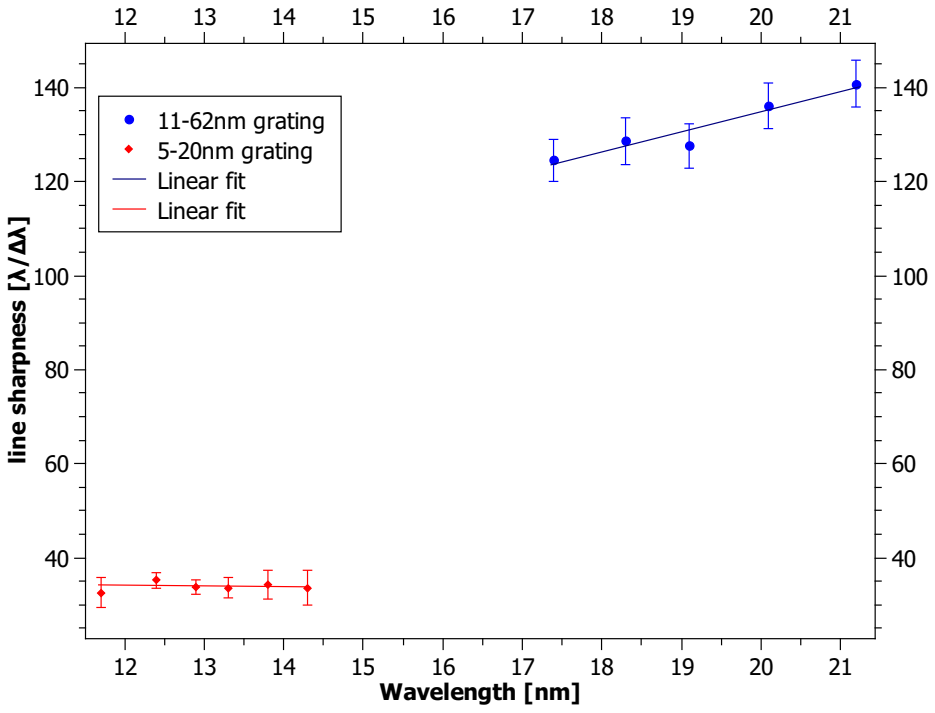

Figure 44: Line sharpness measured with the 11-62 nm grating from 17.4 nm to 21.2 nm (blue) and with the 5-20 nm grating from 11.7 nm to 12.4 nm (red).

From the energy-time uncertainty, the time-bandwidth product can be derived:

$$\triangle E \cdot \triangle t \gtrsim h \tag{28}$$

$$\triangle \nu \cdot \triangle t \equiv TBP \tag{29}$$

The time-bandwidth product of a pulse is the product of the FWHM of its temporal duration and its spectral width. A pulse with the minimum time-bandwidth product is called "Fourier-transform limited" or "bandwidth-limited". There are different kinds of pulse envelops possible, for example the Gaussian and the sech^2 pulses, which look very similar. The TBP of these pulses differ due to the faster decay rate of the Gaussian pulse: $TBP_{gaus} = \frac{2 \cdot ln2}{\pi} = 0.441$ and $TBP_{sech^2} = 0.315$. With the transformation of equation (29) and by insertion of the difference between upper and lower frequency limit, the pulse duration for each harmonic can be calculated.

The results of these calculations are summarized in table 3, which includes the line sharpness, the bandwidth and the resulting pulse duration for both assumed pulse envelops. The harmonic pulse duration decreases with decreasing wavelength (see table 3). Compared to the driving laser pulse duration of the 25 fs, the Gaussian harmonic pulses are shorter by a factor of 5.5 to 7.8. A very similar factor is obtained for the 3.9 fs laser pulses where the harmonics are shortened by a factor of 5.5 to 6.9. These calculated values mark a lower limit for the pulse duration because a Fourier-transform limited pulse is an ideal compressed pulse without any spectral chirp.

laser pulse duration [fs]	harmonic order	wavelength [nm]	line sharpness	bandwidth [nm]	pulse duration gauss [fs]	pulse duration $sech^2$ [fs]
25						
	37	21.2 $\pm$0.1	140.8 $\pm$5.0	0.145 $\pm$0.005	4.55 $\pm$0.16	2.29 $\pm$0.08
	39	20.1 $\pm$0.1	136.2 $\pm$4.9	0.148 $\pm$0.005	4.04 $\pm$0.14	2.46 $\pm$0.09
	41	19.1 $\pm$0.1	127.6 $\pm$4.7	0.150 $\pm$0.006	3.60 $\pm$0.13	2.57 $\pm$0.09
	43	18.3 $\pm$0.1	128.6 $\pm$4.9	0.142 $\pm$0.005	3.44 $\pm$0.13	2.88 $\pm$0.10
	45	17.4 $\pm$0.1	124.6 $\pm$4.5	0.140 $\pm$0.005	3.21 $\pm$0.11	3.25 $\pm$0.12
3.9						
	55	14.3 $\pm$0.1	33.6 $\pm$3.7	0.425 $\pm$0.047	0.71 $\pm$0.08	0.50 $\pm$0.06
	57	13.8 $\pm$0.1	34.3 $\pm$3.1	0.410 $\pm$0.037	0.68 $\pm$0.06	0.49 $\pm$0.04
	59	13.3 $\pm$0.1	33.6 $\pm$2.2	0.396 $\pm$0.026	0.66 $\pm$0.04	0.47 $\pm$0.03
	61	12.9 $\pm$0.1	33.7 $\pm$1.5	0.382 $\pm$0.017	0.64 $\pm$0.03	0.46 $\pm$0.02
	63	12.4 $\pm$0.1	35.2 $\pm$1.7	0.352 $\pm$0.017	0.64 $\pm$0.03	0.46 $\pm$0.02
	67	11.7 $\pm$0.1	32.6 $\pm$3.1	0.359 $\pm$0.034	0.56 $\pm$0.05	0.40 $\pm$0.04

Table 3: Bandwidth and pulse duration listed for each harmonic

4 1D-Simulations of the QPM target

With a 1D simulation it is possible to define roughly the laser parameters and the target parameters to achieve the best conditions for phase matching or quasi-phase matching. Selectable laser parameters include the peak intensity, the pulse duration and the central wavelength. Selectable target parameters include the gas pressure of the HHG medium (for example argon, neon or helium) as well as the pressure of the phase tuning gas, in this case hydrogen. Furthermore, the number of nozzles, their length and the resulting pressure profile have to be defined. From comparison of the simulation to experimental results, it is possible to explain enhancement factors caused by quasi-phase matching. Additional effects such as absorption or alteration of the driving laser pulse by plasma defocusing or self-phase modulation are not considered.

4.1 Structure of the code

The simulation is written using the software Mathematica. One of the main advantages of the simulation in comparison to complex three dimensional numerical codes is the short execution time in the range of a few minutes, depended on the geometrical and pressure resolution. This offers the opportunity to use it parallel to an experiment and compare the results directly. In this section the different work packages of the code are described.

In the first package the driving laser pulse is defined by its duration, wavelength and peak intensity.

The second package calculates the tunnel ionisation rate in the gas medium with ADK (Ammosov–Delone–Krainov) theory [58]. The ADK calculation is an improvement or generalisation of the tunnel ionisation calculation for hydrogen like atoms in a static electric field, which was developed by L. Keldysh in 1965 [59]. The ADK ionisation probability is given by:

$$\omega_{ADK} = \left(\frac{3 \cdot e}{\pi}\right)^{\frac{3}{2}} \cdot \frac{Z^2}{n^{\frac{9}{2}}} \cdot \left(\frac{4 \cdot e \cdot Z^3}{n^4 \cdot F}\right)^{2n-\frac{3}{2}} \cdot exp\left(-\frac{2Z^3}{3 \cdot n^3 \cdot F}\right) , \qquad (30)$$

where F is the electric field in atomic units, $e = 2.718$ is Euler's constant and n is the effective quantum number calculated from the ion charge Z and the ionisation potential I_P given by:

$$n = \frac{Z}{\sqrt{2 \cdot I_P}}$$

The electric field F is calculated from the laser intensity with equation (11), where the electron charge, the mass of an electron and the Dirac constant are defined by $e_c = m = \hbar = 1$. In this part of the simulation the type of gas for the HHG medium has to be chosen and the ionisation rates for single and double ionisation are calculated.

The third part of the code calculates the ionisation fraction from the ionisation rates of the whole laser pulse.

Before the main part of the simulation is started the nozzle geometry is defined by the number of gas jets, their length as well as the pressure profile. The number of points used to spatially resolve the jets can be chosen arbitrarily. Note, the better the resolution the longer the calculation time. Pressure profiles implemented as standard profiles include a single HHG gas nozzle as well as several HHG gas nozzle interspersed with hydrogen nozzles. The division between different gas jets can either be rectangular contrast or a sinusoidal. However, it is no problem to run simulations with a measured pressure profile, if it has been determined experimentally. It is assumed that a convolution of a sinusoidal profile (see figure 45 (a)) with a rectangular profile (see figure 45 (b)) is the most realistic pressure profile.

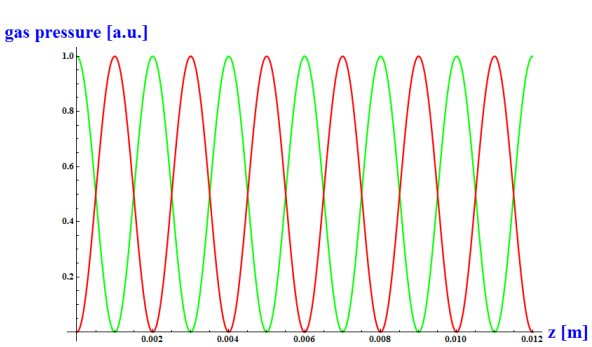

(a) Sinusoidal pressure profile of hydrogen (green) and the HHG gas (red).

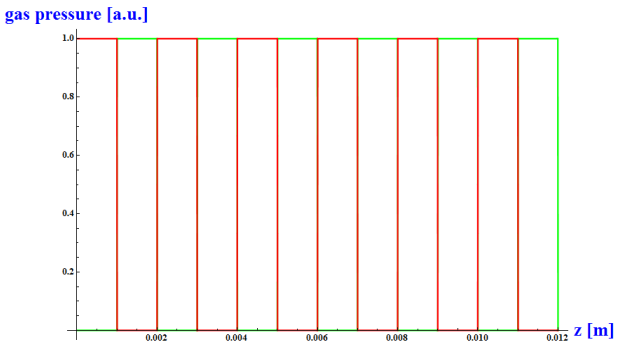

(b) Rectangular pressure profile of hydrogen (green) and the HHG gas (red).

Figure 45: Gas pressure profiles of the simulated dual-gas target.

The main part of the simulation scans for a fixed HHG gas pressure through a defined hydrogen gas pressure range. The wave vector mismatch $\triangle k$ is calculated for each gas pressure, harmonic order and propagation range, from the normal dispersion in the HHG gas (equation (21)), the plasma dispersion for both gases (equation (22)) and the Gouy phase shift (equation (5)). The wave vector mismatch is then used to calculate the intensity of the harmonic signal

$$I(q,n) = \left| \sum_{x}^{n} C(x) \cdot e^{-2 \cdot i \cdot \triangle k(x,q) \cdot L_{Single\,Jet}} \right|^2 ,$$

where C is the gas density, q is the harmonic order and n is the number of the considered data points, which is the propagation range when multiplied with $L_{Single\,Jet}$.

4.2 Results of the simulation

The harmonic energy is calculated in arbitrary units and it is not correlated to the actual harmonic energy achieved in an experiment, because the HHG process is not considered in this physical model. Thus, the energy modulation due to QPM is in the focus of the code.

The following simulations were performed with approximately the same parameters as used for the experiment. The laser pulses have a duration of 4 fs, a central wavelength of 780 nm and an intensity of $1.5 \cdot 10^{15} \frac{W}{cm^2}$. The selected HHG gas is neon, which results in a total ionisation of $\eta = 13.6\,\%$ after the complete laser pulse has passed. The target has a length of 1.2 mm and consists of 12 nozzles with a length of 100 μm. The applied gas in the matching zones is hydrogen, which is completely ionized at this laser intensity.

In order to achieve the highest enhancement factor due to QPM for this setup, it is necessary to determine the neon gas pressure at which the phase advance of a single neon nozzle with a length of 1.2 mm is $\varphi = 12 \cdot L_{coherence}$. In that case one coherence length corresponds to the length of one nozzle $L_{coherence} = 100\,\mu m$. By suppression of the HHG process at the points of destructive interference (by insertion of hydrogen instead of neon) an enhancement factor of 36 can be achieved for a QPM target with 6 single HHG nozzles and a rectangular pressure profile. The increase of the harmonic energy with the propagation in the target is plotted for the 63^{rd} harmonic in figure 46. Here, the energy was normalised to the energy after one coherence length. The simulation can be used to determine the hydrogen pressure, so that the phase advance by the hydrogen nozzle is equal to the phase advance of a neon nozzle. This is necessary, because otherwise the phase of the HHG radiation in the following neon zones will lead to destructive interference. In figure 47 the phase of the HHG radiation is plotted versus the propagation distance z in the target. Here, the phase is normalized by π so that the phase is plotted in units of coherence lengths. The red dots mark the normalized pressure of neon and the yellow dots mark the normalized pressure of hydrogen. In this example the phase is shifted by only one coherence length per nozzle, which corresponds to first order quasi phase matching.

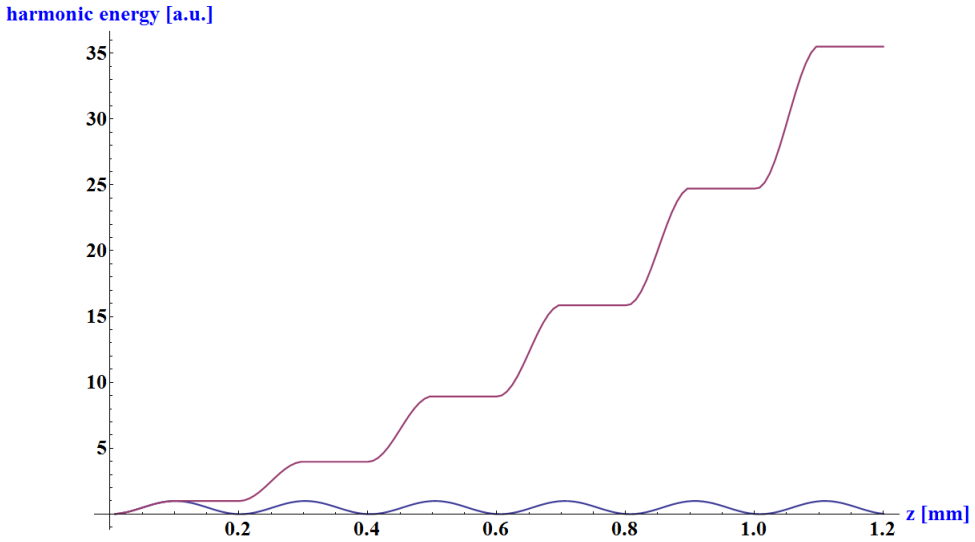

Figure 46: Intensity of the 63^{rd} harmonic versus the propagation range in the target, for a single neon jet (blue) and a combination of six neon jets with six hydrogen jets (red).

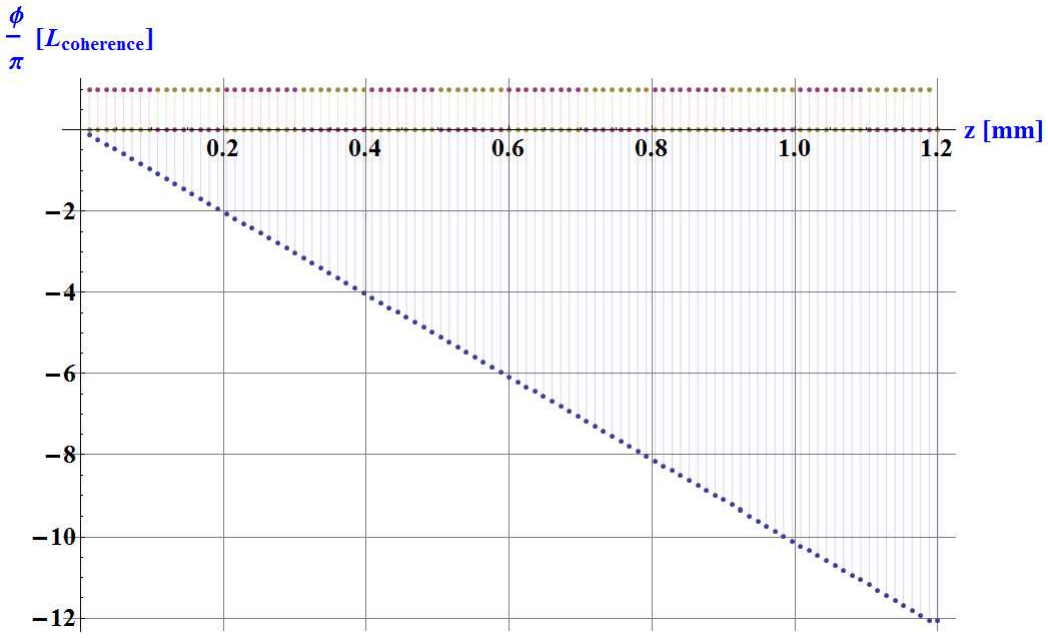

Figure 47: Phase advance during the propagation in neon (red) and hydrogen (yellow) for the 63^{rd} harmonic.

Actually, it will be challenging to achieve a perfect rectangular pressure profile for both gases as they will mix at the edges of each single nozzles. With the assumption of a sinusoidal pressure profile for both gases, an enhancement

factor of only 22.5 can be achieved. This factor is smaller because of a mixture of neon and hydrogen in the matching zones. Thus, radiation is generated in the matching zones, which then interferes destructively with the former generated radiation. This is visible in figure 48, where the harmonic energy decreases in the matching zones. The simulation of a sinusoidal pressure profile is a worst case scenario. Thus, the actual enhancement factor of the target will be larger than 22.5 but smaller than 36, which represents the ideal case.

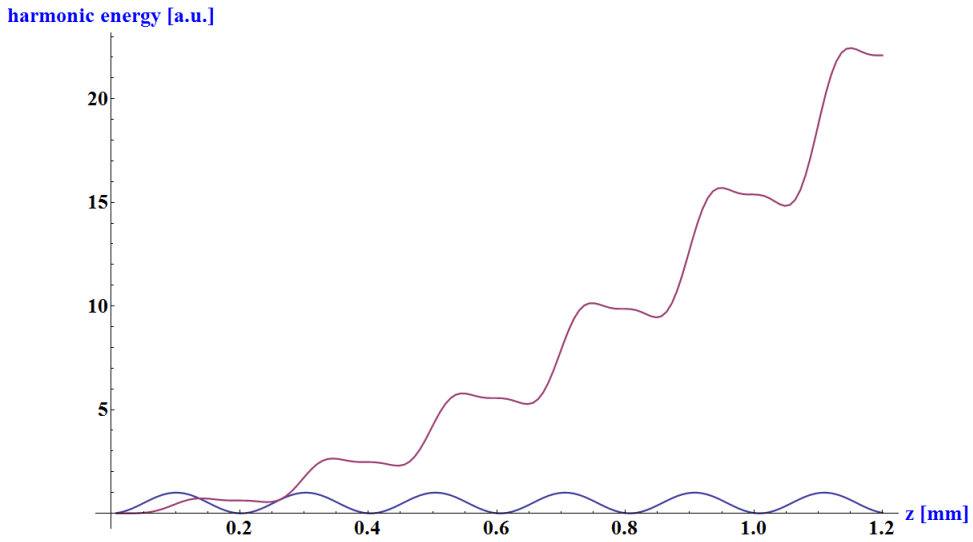

Figure 48: Intensity of the 63^{rd} harmonic versus the propagation range in the target, for a single neon jet (blue) and a combination of six neon jets with six hydrogen jets (red) with sinusoidal pressure profile.

The phase advance in neon depends strongly on the applied laser intensity. Thus, in order to compare the measurements with the simulation it is necessary to determine the actual gas pressure and the pulse energy precisely. For example, if the intensity is varied between $1.1 \cdot 10^{15} \frac{W}{cm^2}$ and $1.9 \cdot 10^{15} \frac{W}{cm^2}$ the ionization fraction of neon is increased from 4.4 % to 27.9 %. In that case, the phase advance changes from $-3.1 \cdot L_{coherence}$ to $-28.8 \cdot L_{coherence}$ (see figure 49) for a single nozzle of a length of 1.2 mm and neon pressure of 80 mbar. The reason for this is the fast increase of the negative contribution of the plasma dispersion to the phase advance, whereas the positive contribution of the neutral gas dispersion decreases. The actual gas density could be determined by comparison of an experiment with the simulation. Therefore it is first of all necessary to determine the laser pulse energy exactly. Afterwards the number of oscillations of the harmonic energy have to counted, while the neon pressure is increased.

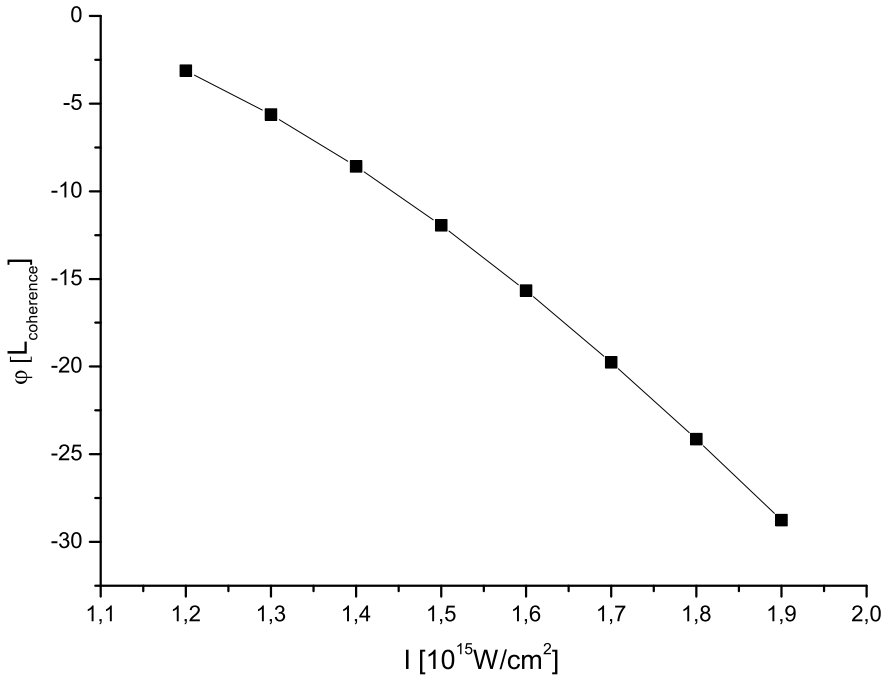

Figure 49: Phase advance in a single nozzle of 1.2 mm with 80 mbar neon in dependence on the applied laser intensity.

4.2.1 Simulation for the FLASH2 seeding system

The FLASH2 seeding laser is planned to deliver pulses of $\lambda_c = 780\,nm$, $\tau = 15\,fs$, $E = 2\,mJ$. If the beam is focused to $100\,\mu m$ (FWHM) an intensity of $1.7 \cdot 10^{15} \frac{W}{cm^2}$ can be achieved. In order to to have 12 coherence lengths at the 63^{rd} harmonic for a single neon nozzle with a length of 1.2 mm an actual neon pressure of 15 mbar would be necessary. In figure 50, a simulated hydrogen scan from 0 to 10 mbar to tune the phase for a QPM target with 6 hydrogen and 6 neon nozzles and a rectangular pressure profile is plotted. The harmonic energy is plotted in arbitrary units, where the highest energy corresponds to the brightest colour. Due to the applied neon pressure the maximal enhancement factor of 36 is only achievable for the 63^{rd} harmonic at a hydrogen pressure of 4.5 mbar. For the 55^{th} harmonic, the highest enhancement factor of 33 is achieved at a hydrogen pressure of 5.5 mbar, whereas the enhancement for higher order harmonics is at lower hydrogen pressures. This is due to the fact that the plasma dispersion as well as the neutral gas dispersion depend on the harmonic order. In conclusion, shorter wavelengths require less HHG and hydrogen gas pressure to achieve the same phase advance as longer wavelengths. Thus, it is possible to decrease the gas pressure and accordingly increase the

number of QPM schemes to achieve higher enhancement factors at shorter wavelengths.

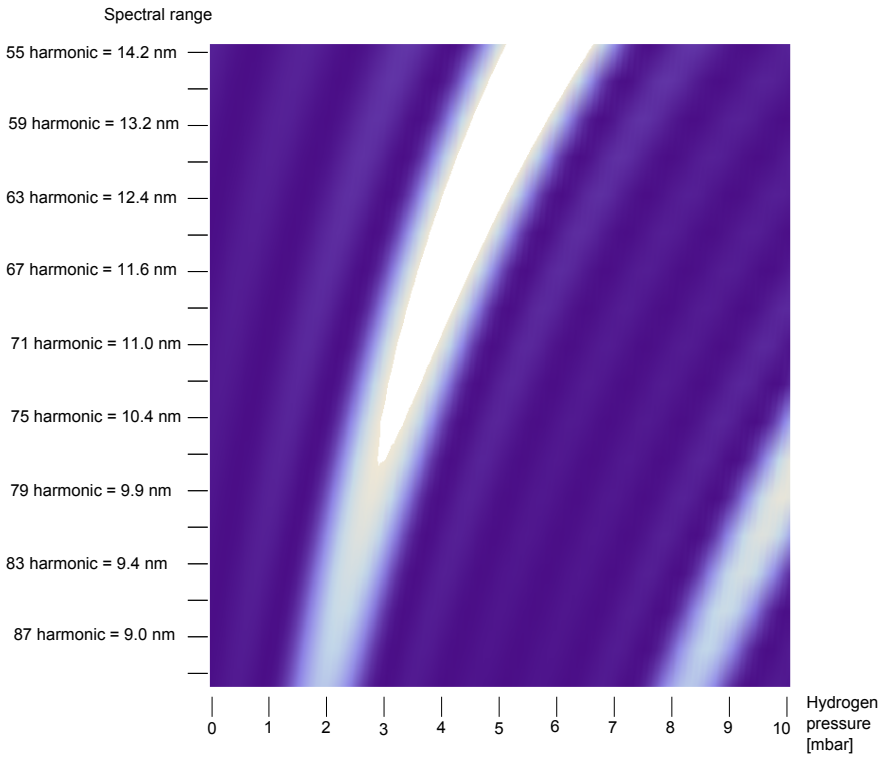

Figure 50: Simulated hydrogen pressure scan for the FLASH2 seeding system for a wavelength range from 9 to 14.2 nm, where the highest energy corresponds to the brightest colour.

5 Conclusion and Outlook

A new XUV spectrometer has been developed for the characterisation of the seed radiation of FLASH2 and was tested successfully. The design is improved due to the insights gained during the experiment. Furthermore, the synchronization of the spectrometer to the target as well as the remote control have been accomplished. The complete setup will be ready for operation at the FLASH2 seeding system in the first half of 2012. The implementation of a Shack-Hartmann wave front sensor as an additional diagnostic tool for the XUV radiation is under consideration. These sensors are used to measure the perturbation of the wave front, so that an adaptive optical system can be tuned in order to reduce the aberration. As these sensors include a XUV CCD camera and have to be placed in the direct beam an integration into the spectrometer would be reasonable.

Experiments with the QPM target were performed to verify its high conversion efficiency in a spectral range from about 10 to 22 nm. The dual-gas QPM target will be improved further by the knowledge gained from the experiments. Therefore a new gas supply setup is planned as well as a new target design is constructed with smaller nozzles. The new target offers the opportunity to control each nozzle pressure individually. Thus, the phase advance in each zone can be optimized until best phase matching for the whole target is achieved.

With the newly developed analytical simulation reasonable tuning parameters and a suitable target setup can be investigated. As this simulation is based on several simplifications it is necessary to measure the actual gas pressure of the target. These measurements will be carried out in the first half of 2012. Furthermore, QPM simulations with a numerical three dimensional code will be performed to prove the results of this simulation and to further explain the experimental results.

List of Figures

List of Tables

References

[1] photon science 2010[a] - highlights and hasylab annual report. page 76, 2010.

[2] S. Schreiber et al. Flash upgrade and first results. *Proceedings of FEL2010, Malmö, Sweden*, 2010.

[3] F. Tavella et al. Fiber-amplifier pumped high average power few-cycle pulse non-collinear opcpa. *Optics Express*, 18:4689–4694, 2010.

[4] W. C. Roentgen. Über eine neue art von strahlen. *Stahel'sche K. Hof- und Universitaetsbuch- und Kunsthandlung*, 1895.

[5] W. Demtröder. *Experimentalphysik 3: Atome, Moleküle und Festkörper*. Springer, 2010.

[6] P. Schmüser, M. Dohlus, and J. Rossbach. *Ultraviolet and Soft X-Ray Free-Electron Lasers*. Springer, 2008.

[7] R. Paschotta. *Encyclopedia of Laser Physics and Technology*. Wiley-VCH, Berlin, 2008.

[8] E. Loewen and C. Palmer. *Diffraction Grating Handbook*. Newport Corporation, 2005.

[9] B. E. A. Saleh and M. C. Teich. *Fundamentals of Photonics*. John Wiley & Sons, Inc., 1991. Chapter 19 Nonlinear Optics.

[10] P.A. Franken et al. Generation of Optical Harmonics. *Phys.Rev.Lett.*, 7: 118–119, 1961. doi: 10.1103/PhysRevLett.7.118.

[11] G. A. Reider. *Photonik Eine Einführung in die Grundlagen*. Springer Verlag, 1997.

[12] M. Drescher. Lecture notes: Ultrafast optical physics. 2010.

[13] A. E. Siegman. *Lasers*. Mill Valley, Calif. : University Science Books, ©1986.

[14] S.C. Rae. Ionization-induced defocusing of intense laser pulses in high-pressure gases. *Optics Communications*, 97:25–28, 1993.

[15] N. Zhavoronkov G. Stibenz and G. Steinmeyer. Self-compression of millijoule pulses to 7.8 fs duration in a white-light filament. *Optics Letters*, 31,2:274–276, 2006.

[16] J. L. Krause et al. High-order harmonic generation from atoms and ions in the high intensity regime. *Physical Review Letters*, 68, 24:3535–3538, 1992.

[17] M. Lewenstein et al. Theory of high-harmonic generation by low-frequency laser fields. *Phys. Rev. A*, 49:2117–2132, Mar 1994. doi: 10.1103/PhysRevA.49.2117.

[18] P. B. Corkum. Attosecond pulses at last. *Nature*, 403:845–846, 2000.

[19] C. M. Kim and C. H. Nam. Selection of an electron path of high-order harmonic generation in a two-colour femtosecond laser field. *J. Phys. B: At. Mol. Opt. Phys.*, 39:3199–3209, 2006.

[20] B. Dromey et al. Quasi-phasematching of harmonic generation via multimode beating in waveguides. *Optical Society of America*, 2007.

[21] J. Lohbreier. *Characterization and Optimization of High-order Harmonics after Adaptive Pulse Shaping*. PhD thesis, Julius-Maximilians-Universität Würzburg, 2008.

[22] H. Ren et al. Quasi-phase-matched high harmonic generation in hollow core photonic crystal fibers. *Optical Society of America*, 2008.

[23] 2011. URL `http://henke.lbl.gov/optical_constants/`.

[24] A. Paul et al. Quasi-phase-matched generation of coherent extreme-ultraviolet light. *Nature*, 421:51–54, 2002.

[25] I. Christov, H. Kapteyn, and M. Murnane. Dispersion-controlled hollow core fiber for phase matched harmonic generation. *Optics Express*, 3:360–365, 1998.

[26] M. Zepf et al. Bright quasi-phase-matched soft-x-ray harmonic radiation from argon ions. *Phys. Rev. Lett.*, 99:143901, 2007.

[27] J. Seres et al. Coherent superposition of laser-driven soft-x-ray harmonics from successive sources. *Nature Physics*, 3:878 – 883, 2007.

[28] B. A. Sickmiller. High harmonic generation from transiently aligned molecules in a hollow-core waveguide. *Dissertation*, 2008.

[29] A. L'Huillier, K. J. Schafer, and K. C. Kulander. High-order harmonic generation in xenon at 1q64 nm: The role of phase matching. *Physical Review Letters*, 66, 1991.

[30] A. Willner et al. Coherent control of high harmonic generation via dual-gas multijet arrays. *PRL*, 107, 2011.

[31] F. Hinterberger. *Physik der Teilchenbeschleuniger*. Springer, 2008.

[32] 2011. URL `http://flash.desy.de/`.

[33] M. Drescher et al. Time-diagnostics for improved dynamics experiments at xuv fels. *Journal of Physics B: atomic, molecular and optical physics*, 43, 2010.

[34] L.-H. Yu et al. High-gain harmonic-generation free-electron laser. *Science 11*, Vol. 289 no. 5481:932–934, 2000.

[35] L. H. Yu et al. First ultraviolet high-gain harmonic-generation free-electron laser. *PRL, 074801*, 91, 2003.

[36] V. Miltchev et al. Simulation studies on the self-seeding option at flash. *Proceedings of FEL, BESSY, Berlin, Germany*, 2006.

[37] J. Boedewadt et al. A compact electron photon diagonstic unit for a seeded fel. *Proceedings of DIPAC09, Basel, Switzerland*.

[38] A. Willner. *A High Repetition Rate XUV Seeding Source for FLASH2*. PhD thesis, Institut fuer Experimentalphysik Universitaet Hamburg, 2011.

[39] M. Schulz et al. Yb:yag innoslab amplifier: efficient high repetition rate subpicosecond pumping system for optical parametric chirped pulse amplification. *Optics Letters 36*, 13:2456–2458, 2011.

[40] T. Harada et al. Optimum design of a grazing-incidence flat-field spectrograph with a spherical varied-line-space grating. *Appl. Opt. 38, 2743-2748*, 1999.

[41] 2011. URL `http://gratings.newport.com/information/handbook/chapter3.asp`.

[42] 2011. URL `http://www.hitachi-hitec.com/`.

[43] F. Frassetto et al. Compact spectrometer for the analysis of high harmonics content of extreme-ultraviolet free-electron-laser radiation. *SPIE–The International Society for Optical Engineering*, Proc. SPIE 7802, 780209, 2010.

[44] F. Schäfers. Ray - the bessy raytrace program. *Springer Series in Modern Optical Sciences: Modern Developments in X-Ray and Neutron Optics, eds. A. Erko, M. Idir, Th. Krist, A.G. Michette, Springer Berlin/Heidelberg*, 137:9–41, 2008.

[45] T. Harada et al. Optimum design of a grazing-incidence flat-field spectrograph with a spherical varied-line-space grating. *Optical Society of America*, 38 No. 13:2743–2747, 1999.

[46] Z. Shi et al. A ray-tracing program and two cases of its application at the shanghai ebit laboratory. *IOPscience*, Phys. Scr. T144 (2011) 014066 (3pp), 2011.

[47] Princeton Instruments. Direct detection of x-rays (30ev to 20kev) using detectors based on ccd technology. 2010.

[48] 2011. URL `http://www.princetoninstruments.com`.

[49] 2011. URL `http://www.ird-inc.com/index.html`.

[50] 2011. URL `http://ttfinfo.desy.de/DOOCSWiki/`.

[51] URL `http://mpsd-cmd.cfel.de/xts/index.html`.

[52] 2011. URL `http://www.mksinst.com/`.

[53] 2011. URL `http://www.edwardsvacuum.com/xds/`.

[54] 2011. URL `http://www.oerlikon.com/leyboldvacuum/ecomaXL/oe_VACUUM_EN_home`.

[55] O. L. Landen and W. E. Alley. Dynamics of picosecond-laser-pulse plasmas determined from the spectral shifts of reflected probe pulses. *Physcial Review A*, 46/8, 1992.

[56] W. Theobald et al. X-ray preheating of window materials in direct-drive shock-wave timing experiments. *PHYSICS OF PLASMAS*, 13:122702–1, 2006.

[57] E. L. Falcão-Filho et al. Scaling of high-order harmonic efficiencies with visible wavelength drivers: A route to efficient extreme ultraviolet sources. *Applied Physics Letters*, 97:061107, 2010.

[58] J. P. Brichta et al. Comparison of adk ionization rates as a diagnostic for selective vibrational level population measurement. *J. Phys. B: At. Mol. Opt. Phys. 39 3769*, 2006.

[59] L. V. Keldysh. Zh. eksp. teor. fiz. 47 1945. *Sov. Phys. JETP 20 1307*, 1965.

Acknowledgement

First of all I would like to thank Prof. Dr. Jörg Rossbach for the opportunity to start my research work at DESY first as a student research assistant and afterwards as a diploma student. Furthermore I am thankful for the opportunities to work as an operator at FLASH and to attend a summer school about laser plasma physics.

I am very grateful to my supervisor Dr. Arik Willner for teaching me for more than two years now. And there is still no end in sight. He had always time and fun to support me or to answer my questions although he was working and writing on his own PhD thesis.

I would like to thank Dr. Franz Tavella for the opportunity to work in his group and for the introduction into laser physics. Many problems, which came along with the spectrometer, were solved by the amazing teamwork of Joseph Gonschior and Otto Peters. Their experience in construction work and their knowledge how to solve problems in the last minute during experiments is irreplaceable. Furthermore, I want to thank Robert Riedel and Michael Schulz for explaining and demonstrating how to push a laser to its limits. Thanks also to Dr. Mark Prandolini for the review of my thesis and to Max Wiedorn, the new student research assistant, for his support.

Erklärung

Ich versichere hiermit dass ich die vorliegende Diplomarbeit selbständig verfasst und keine anderen als die angegebenen Quellen und Hilfsmittel genutzt habe. Ich bin damit einverstanden, dass die Diplomarbeit veröffentlicht wird.

Hamburg, den 29. Februar 2012

Arvid Hage